Impedance Control Network Resonant DC-DC Converters for Wide-Range High-Efficiency Operation

by

Jie Lu

B.Eng., Harbin Institute of Technology, 2012

M.S., University of Colorado Boulder, 2015

A thesis submitted to the

Faculty of the Graduate School of the

University of Colorado in partial fulfillment

of the requirements for the degree of

Doctor of Philosophy

Department of Electrical, Computer, and Energy Engineering

2016

This thesis entitled:

Impedance Control Network Resonant DC-DC Converters for Wide-Range High-Efficiency Operation

written by Jie Lu

has been approved for the Department of Electrical, Computer, and Energy Engineering

_____

Khurram Afridi

_____

Dragan Maksimovic

Date_____

The final copy of this thesis has been examined by the signatories, and we find that both the content and the form meet acceptable presentation standards of scholarly work in the above mentioned discipline.

Jie Lu (Ph.D., Electrical Engineering)

Impedance Control Network Resonant DC-DC Converters for Wide-Range High-Efficiency Operation

Thesis directed by Prof. Khurram Afridi

Abstract

Grid-level power converters based on conventional architectures do not achieve very high efficiencies, and their efficiencies drop substantially as the operating conditions change. This thesis introduces and demonstrates a new resonant converter architecture that operates at fixed frequency and maintains zero-voltage switching (ZVS) and near zero-current switching (ZCS) across wide operating ranges in terms of input/output voltages and output power, minimizing device stresses and switching losses, and enabling both high efficiency and high power density. Unlike a conventional resonant converter, which utilizes a single inverter and a single rectifier, this Impedance Control Network (ICN) resonant converter has multiple inverters and one or more rectifiers. It also utilizes a lossless impedance control network, which provides a differential phase shift in the voltages and currents, whereby the effective impedances seen at the inverter outputs look purely resistive at the fundamental frequency, enabling switching of the inverters at zero current. By modifying the network for slightly inductive loading of the inverters, one can realize simultaneous ZVS and near-ZCS across wide operating ranges.

This thesis also introduces a new modeling approach, termed step-superposition (S2) analysis, which enables exact modeling and optimization of high-order resonant converters. Three 200 W, 500 kHz step-up (25 V to 40 V input and 250 V to 400 V output) ICN resonant converter prototypes which are optimized using S2 analysis are designed, built and tested. One of these converters achieves a peak efficiency of 97.1%, and maintains greater than 96.4% full power efficiency at 250 V output voltage across its nearly 2:1 input voltage range. An optimized startup control approach is developed to further improve the efficiency of ICN converters operating under burst-mode control. This thesis also introduces an alternative to burst-mode control, termed enhanced phase-shift control, which reduces the output capacitance requirement by a

factor of 100. A 120 W, 1 MHz step-down (18 V to 75 V input and 12 V output) ICN converter that demonstrates the advantages of this enhanced phase-shift control is designed, built and tested. Finally, a closed-loop control approach for output voltage regulation in ICN converters is introduced and its effectiveness is demonstrated.

Acknowledgements

I would like to express my deepest gratitude to my advisor, Prof. Khurram Afridi, for his guidance, encouragement and support throughout my PhD program at CU Boulder. His knowledge in power electronics is unparalleled. I have gained large amount of professional knowledge from him. In addition, he has taught me invaluable presentation skills, writing skills, scientific thinking, effective studying, problem solving, and positive approaches to difficult situations. Being one of his PhD students has brought tremendous changes in my life, and all the things I have learned from him will continue to make differences in my life in the future.

I also wish to thank my thesis committee members: Prof. David J. Perreault, Prof. Dragan Maksimovic, Prof. Robert W. Erickson, and Dr. David C. Jones for their advice and help. Their advice has helped make this thesis stronger. In addition, I would like to acknowledge the financial support received from the National Science Foundation (NSF) for the work conducted as part of my PhD thesis.

I would like to give special thanks to my colleague Ashish Kumar in the high frequency power electronics group (HFpeg). The way he thinks through problems is really powerful. I have learned a lot from many inspiring discussions with him. He has used his excellent writing and presentation skills to generously help me in writing papers and making presentation slides. I would also like to thank other student members of HFpeg: Saad Pervaiz, Alihossein Sepahvand, Yu Ni, Colin McHugh, Usama Anwar, Yushi Liu, Brandon Regensburger, Sreyam Sinha, and Katharine Doubleday. I also want to extend my thanks to many members of the Colorado Power Electronics Center (CoPEC): Beom Seok Choi, Hua Chen, Yuanzhe Zhang, Fan Zhang, Fenglong Lu, Hyeokjin Kim, Prasanta Achanta, and Jianglin Zhu.

Finally, I would like to acknowledge both the financial and emotional support from my family. Especially, I would like to thank the support and understanding from my girlfriend Xiaohuan (Linda) Chen.

Contents

Chapter

Tables

Table

Figures

Figure

Chapter 1

Introduction

1.1 Motivation

Compact isolated converters operating at large conversion ratios are needed for applications ranging from off-line power supplies to solar micro-inverters. Such converters based on conventional architectures often do not achieve very high efficiencies, and their efficiencies typically drop from peak values as the operating conditions change. It has been estimated that power supply losses typically account for 20 to 70% of all energy that electronic products consume, and as much as 4% of our entire national electrical energy consumption can be traced to power supply losses for electronic loads, owing largely to poor average power supply efficiencies [1]. Likewise, poor power factor is estimated to be indirectly responsible for as much as 2.8% of energy consumption in commercial buildings [2]. Improved power conversion is also important for dc distribution systems, which are being seriously considered as an alternative to ac distribution in commercial buildings and data centers, as they offer higher efficiency, more effective management of power factor correction, and easier integration of distributed renewable sources and energy storage. Crucial to the integration of distributed renewable sources, energy storage and electronic loads into dc distribution networks, however, are the dc-dc converters that act as an interface between their relatively low voltages (e.g., 25 V to 40 V for solar photovoltaic modules) and the high voltages of the dc bus.

1.2 State of the Art

State of the art high-performance converters that provide an interface between the photovoltaic panels and the ac grid (up to 240 V ac), or dc distribution systems (260 – 410 V dc), achieve peak efficiencies of up to 90-95% (5-10% loss) with much lower average efficiencies. To achieve these high efficiencies, power converters must operate using soft-switching techniques - zero-voltage switching (ZVS, in which the transistor voltage is constrained close to zero when switching on or off) and/or zero-current switching (ZCS, in which the transistor current is constrained close to zero when switching on or off). Without soft

switching, transistor switching loss prevents high efficiency from being obtained and also limits power density, owing to the need to operate at low switching frequencies.

Unfortunately, while available soft-switching circuits can achieve very high efficiencies under specific operating conditions, performance tends to degrade greatly when considering requirements of operation across widely varying input voltage and power levels. In particular, with conventional circuit designs and control methods, it is difficult to maintain desirable circuit waveforms (e.g., ZVS/ZCS switching, minimum conduction current, etc.) as power is reduced from maximum and as the input voltage varies from nominal. This challenge in maintaining high efficiency is tied to both the circuit design and the control methodology. To understand this challenge, consider some widely-used design and control techniques. One common means of controlling resonant soft-switched converters (e.g., series, parallel, series-parallel, LLC converters, etc.) is frequency control, in which the output voltage is regulated in the face of load and input voltage variations by modulating the converter switching frequency [3], [4]. Because of the inductive loading requirements to achieve ZVS switching, power is reduced in such converters by increasing switching frequency, exacerbating switching loss. Wide frequency operation also makes design of magnetic components and EMI filters more challenging. Moreover, depending on resonant tank design, circulating currents in the converter may not back off with power, reducing efficiency.

An alternative method is phase-shift control [5], [6] or "outphasing" control, in which the relative timing of multiple inverter legs are modulated to control power. However, conventional full-bridge resonant converters using phase shift control suffer from asymmetric current levels between the two inverter legs at the switching instants as the legs are outphased to reduce output power, as shown in Fig. 1.1. The result is that the transistors in the leading inverter leg start to turn off at large currents. Also, as outphasing is increased further, the transistors in the lagging inverter leg lose ZVS turn-on capability. These factors result in extra losses and lead to lower converter efficiency at partial loads, and consequently to poor design tradeoffs. Other fixed frequency control techniques have also been developed [7], [8]. However, these also lose zero voltage switching (ZVS) capability as the output power is reduced [9]. Hence, there is need for

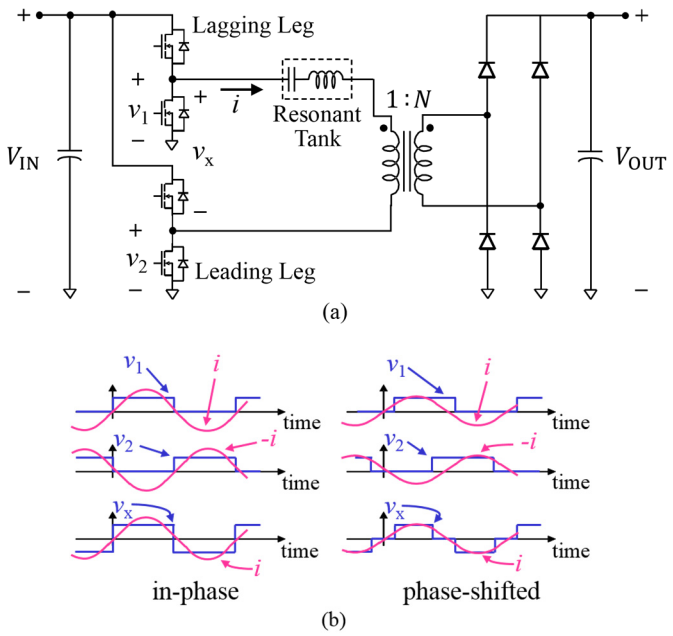

Figure 1.1: Asymmetric current levels at switching instants between two inverter legs and eventual loss of ZVS in (a) conventional full-bridge series resonant dc-dc converter as (b) the two inverter legs are phase-shifted to control output voltage or power.

circuit designs and associated controls that can provide reduced loss when operating over wide input voltage and power ranges, and can provide large voltage conversion ratios.

1.3 Contributions of the Thesis

This thesis introduces a new resonant converter architecture that operates at fixed frequency and maintains ZVS and near-ZCS across wide operating ranges in terms of input/output voltages and output power, minimizing device stresses and switching losses, and enabling both high efficiency and power density. Unlike a conventional resonant converter, which utilizes a single inverter and a single rectifier, this Impedance Control Network (ICN) resonant converter has multiple inverters and one or more rectifiers. It also utilizes a lossless impedance control network, which provides a differential phase shift in the voltages and currents, whereby the effective impedances seen at the inverter outputs look purely resistive at the fundamental frequency, enabling switching of the inverters at zero current across wide operating ranges.

By modifying the network for slightly inductive loading of the inverters, one can realize simultaneous ZVS and near-ZCS. Hence, the ICN converter is able to maintain high efficiency across wide variations in operating conditions. Furthermore, owing to its soft-switching characteristics, the ICN converter can be operated at high switching frequencies, enabling high power densities. The output voltage and power of the ICN converter can be regulated using burst mode (on/off) control, where the converter is turned on and off periodically at a frequency much lower than its switching frequency.

To optimize the design of the ICN converter, an accurate analysis approach for modeling the ICN converter is required. Resonant converters are typically analyzed and designed using fundamental frequency analysis, wherein network waveforms are approximated by their fundamental components and switching frequency harmonics are neglected [41]. This modeling method simplifies the design of resonant converters as it converts the nonlinear power converter into a linear circuit. However, this approach becomes inaccurate when the converter tank waveforms are significantly non-sinusoidal, as is often the case when the quality factor (Q) of the resonant network is low. There are two (related) general approaches for exact analysis of resonant converters: state space analysis, and state plane analysis. State space analysis identifies the operating modes of a resonant converter over one switching cycle, and solves the state vectors recursively from one mode to the next. State space analysis is an accurate and general approach to the analysis of resonant converters, but it requires complicated and time-consuming matrix computations. On the other hand, state plane analysis converts the time-domain analysis of resonant converters to geometrical analysis, where tank waveforms are described using segments of circles, lines or ellipses. Through such graphical representations, state plane analysis simplifies the exact analysis of complicated resonant tank behavior. However, its application is practically limited to simple resonant converters (e.g., with up to two to three tank elements). To analyze high-order resonant converters with multiple tank elements, this method needs to employ complicated higher-dimensional or multiple two-dimensional state planes and becomes difficult to use. This thesis introduces a new analysis approach to modeling resonant converters that can be used to determine closed-form expressions for the exact resonant network waveforms. This approach, based on superposition of step responses to inverter and rectifier imposed steps, does not require analysis of the

different operating modes of a resonant converter, and can easily be applied to resonant converters with high-order resonant networks and multiple inverters and/or rectifiers, such as the ICN converter. In view of its salient features, this approach is termed step-superposition (S2) analysis. This new modeling approach enables resonant converters with low-Q resonant networks to be accurately analyzed and optimized, and is a major contribution of this thesis.

This thesis presents multiple ICN converter prototypes, three of which cater to a high step-up photovoltaic application that requires input voltages varying between 25 V – 40 V to be converted to output voltages in the range of 250 V – 400 V, while delivering up to 200 W of power. These three ICN converter prototypes differ in terms of the Q-factor of their resonant tanks. The low-Q ICN converter, analyzed and optimized using the S2 analysis approach, is found to perform the best, achieving a peak efficiency of 97.1%, maintaining greater than 96.4% full-power efficiency at 250-V output voltage across the nearly 2:1 input voltage range, and full power efficiency above 95% across its full input and output voltage range. It also maintains efficiency above 94.6% over a 10:1 output power range across its full input and output voltage range.

An issue with burst-mode control is that the converter suffers from non-ZVS transitions during the repeated turn-on transients. To tackle this issue, this thesis presents an optimized startup control to improve the efficiency of ICN converters operating under burst-mode control. The optimized startup control minimizes the startup transients of the burst-mode operated ICN converters and helps the converters maintain ZVS and near-ZCS operation even during startup. This startup optimization is made possible by applying the above-mentioned S2 analysis to modeling the ICN converter. It reduces the number of non-ZVS startup transitions by 75%, and reduces losses by up to 20%.

Another issue with burst-mode control is that it introduces a low-frequency ripple in the output voltage of the ICN converter, requiring the converter to have large input and output capacitances. This thesis addresses this issue by introducing an ICN converter that utilizes enhanced phase-shift control to achieve both soft-switching and output voltage regulation. Unlike burst-mode control, where the rectifier legs are switched always at 180° relative to one another, enhanced phase-shift control utilizes the relative phase

between the rectifier legs to regulate output voltage. Since power flows continuously to the output under this control approach, the output voltage does not have a low-frequency ripple, reducing the input and output capacitance requirements of the ICN converter. The avoidance of burst-mode control also simplifies the design of the converter's input EMI filter, reduces switch stresses due to startup overshoots, and improves converter efficiency by eliminating startup and shutdown losses as well as by reducing conduction losses when backing off in power. To demonstrate the efficacy of this new control approach, as well as the performance of the ICN converter in a high step-down telecom application, this thesis presents an enhanced phase-shift controlled ICN converter prototype that operates over an input voltage range of 18 V to 75 V, an output voltage of 12 V, and a 10:1 output power range. This prototype ICN converter achieves a peak efficiency of 95.7% and maintains full-power efficiency above 91.7% across its 4:1 input voltage range. Compared to when operated under burst-mode control, the ICN converter with enhanced phase-shift control reduces converter losses by up to 30% and reduces input and output capacitances by two orders of magnitude.

Finally, this thesis introduces a closed-loop control approach for the ICN converter. A control architecture incorporating a combination of input feed-forward and output feedback control is utilized to regulate the converter output voltage. To facilitate compensator design of the feedback loop, a small-signal dynamic model for the ICN converter is developed. The parameters of the converter transfer function obtained from this model vary widely across the converter's wide operating range, complicating the compensator design. To address this issue, an additional state feedback controller is included to make the parameters of the transfer function insensitive to the operating conditions. This closed-loop control approach successfully regulates the output voltage of the above-mentioned step-down ICN converter prototype over its 4:1 range of input voltage and 10:1 range of output power.

1.4 Thesis Organization

The remainder of this thesis is organized as follows: Chapter 2 describes the architecture, topology and control of the proposed ICN dc-dc converter. Chapter 3 describes the S2 analysis approach. Chapter 4 describes a methodology for the design of an ICN converter. This chapter also describes the design and

implementation of the three prototype step-up ICN converters, and the experimental results from the three step-up ICN prototypes. A step-up ICN resonant converter with optimized startup control is presented in Chapter 5. Chapter 5 also compares the experimental results for the ICN converter with and without the optimized startup control. The enhanced phase-shift control for ICN converters is presented in Chapter 6. Chapter 6 also presents the design and experimental results of a step-down ICN converter utilizing enhanced phase-shift control. A closed-loop control architecture for the ICN converter is introduced in Chapter 7, along with experimental results. Finally, the conclusions of the thesis are presented in Chapter 8. The thesis also contains five Appendices. Appendix A derives the expression for the effective admittances and output power of the ICN converter. Appendix B derives the expressions for the summation of time-shifted decaying sinusoidal functions that is used in the S2 analysis. Appendix C derives expressions for inverter output currents of the ICN converter using S2 analysis. Appendix D provides the loss model that is used to estimate the efficiency and loss breakdown of the ICN converter. Appendix E investigates the sensitivity of the ICN converter's key performance metrics to variations in component values, switching frequency, and the phase shift between the inverters.

Chapter 2

Impedance Control Network (ICN) Resonant Converter

2.1 ICN Converter Architecture

Resonant dc-dc converters comprise an inverter stage, a transformation stage, and a rectifier stage, as shown in Fig. 2.1. Figure 2.2 shows the architecture of the proposed impedance control network (ICN) resonant dc-dc converter. It incorporates multiple inverters and one or more rectifiers operated together under phase-shift control, along with a transformation stage incorporating an impedance control network (ICN). The ICN draws upon the concepts of lossless power combiners and resistance compression networks [10]-[18]. The ICN provides a differential phase shift in the voltages and currents whereby the effective impedances seen at its inputs look purely resistive at the fundamental frequency, enabling switching of the

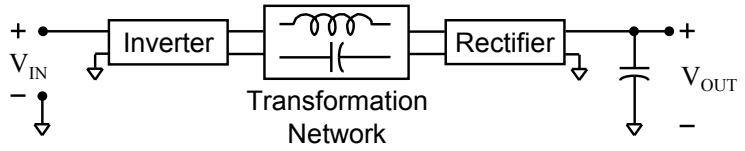

Figure 2.1: Block diagram for a conventional dc-dc resonant converter.

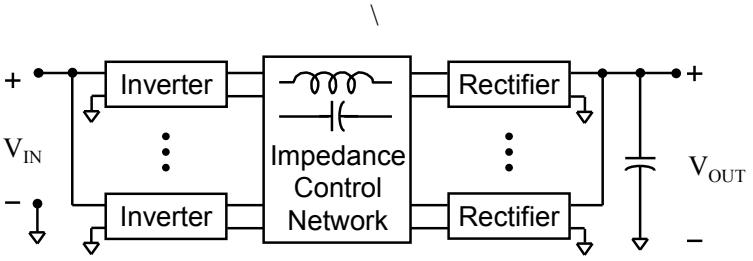

Figure 2.2: Architecture of the proposed impedance control network (ICN) resonant converter. Note that while an input parallel connection of inverter inputs is shown, a series connection may also be employed, and can be advantageous for voltage step-down designs.

inverters at zero current across wide operating ranges[1]. By modifying the networks for slightly inductive loading of the inverters, one can realize simultaneous zero-voltage and near-zero-current switching.

2.2 ICN Converter Topology and Control

There are many possible implementations of the ICN converter. A specific implementation suitable for widely varying input voltages is shown in Fig. 2.3. The converter is operated at a fixed switching frequency and each inverter is operated at a fixed duty ratio (~50%). When the switching frequency of the converter matches the resonant frequency of the resonant tank, and the two branches of the impedance control network are designed to have equal but opposite reactances (+jX and -jX) at the switching frequency, the effective admittances seen by the two inverters (Y_1 and Y_2 of Fig. 2.3) under fundamental frequency approximation and assuming a lossless converter are given by:

$$Y_1 = Y_2^* = \frac{V_{\mathrm{OUT}} \sin\Delta}{N V_{\mathrm{IN}} X} + j\left(\frac{V_{\mathrm{OUT}} \cos\Delta}{N V_{\mathrm{IN}} X} - \frac{1}{X}\right). \tag{2.1}$$

Here V_{IN} is the input voltage, V_{OUT} is the output voltage, N is the transformer turns ratio, and 2Δ is the phase shift between the two inverters. The derivation of (2.1) is provided in Appendix A. With the two branches of the impedance control network designed to have differential reactances, the effective susceptance seen by the two inverters can be made zero or arbitrarily small when the two inverters are operated with a specific phase shift between them, as illustrated in Fig. 2.4. The phase shift at which the susceptance seen by the inverters becomes zero is a function of the input-output voltage ratio and given by:

$$2\Delta = 2\cos^{-1}\left(\frac{N V_{\mathrm{IN}}}{V_{\mathrm{OUT}}}\right). \tag{2.2}$$

Hence, by varying this phase shift as the input or output voltage varies, the admittance seen by the inverters can be kept purely conductive across the full input and output voltage operating range of the dc-dc converter. By operating the converter at a switching frequency slightly higher than the resonant frequency

[1] Here "effective impedance" means the voltage-to-current (V/I) ratio observed at a port with all sources and loads active.

of the L_r - C_r tank, both the inverters can be slightly inductively loaded to achieve ZVS. This allows the inverter switches to have simultaneous zero-voltage switching and near zero-current switching capability, thus minimizing switching losses and reactive currents, boosting converter efficiency over wide input and output voltage ranges.

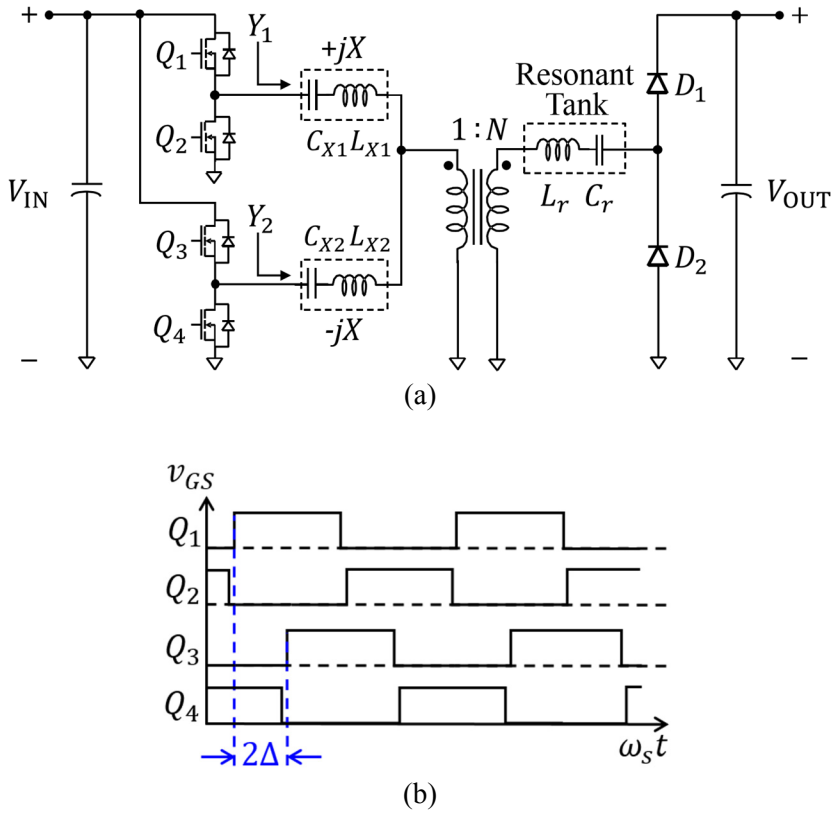

Figure 2.3: One implementation of an impedance control network (ICN) resonant converter, appropriate for voltage step-up: (a) converter topology and (b) switch gating signals.

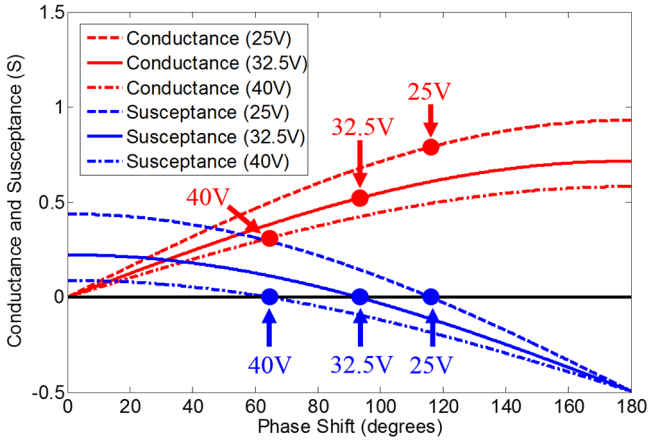

Figure 2.4: Effective conductance (real part of Y_1 or Y_2 as given by (1)) and susceptance (absolute value of imaginary part of Y_1 or Y_2) seen by the two inverters as a function of their relative phase shift for three input voltage values: 25 V, 32.5 V and 40 V. In all cases, output voltage is 250 V, X is 2.026 Ω and N is 5.3.

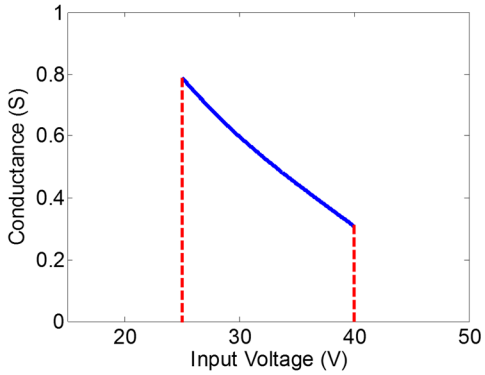

Figure 2.5: Effective conductance seen by the two inverters (real part of Y_1 or Y_2, as given by (1)) as a function of input voltage when the ICN converter with X equal to 2.026 Ω and N equal to 5.3 is operated with zero effective susceptance, at output voltage of 250 V.

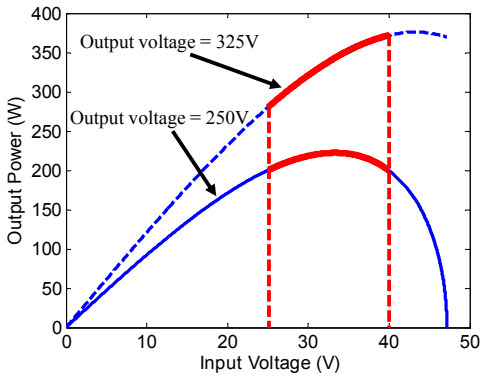

Figure 2.6: Variation in output power as a function of input voltage for the ICN converter operated with the phase-shift between the two inverters controlled to provide zero effective susceptance seen by the inverters. The values of X and N in this ICN converter are 2.026 Ω and 5.3, respectively.

At a given switching frequency, the output power of an inverter is proportional to the square of the input voltage and the conductance seen by the inverter. In conventional designs, this can often lead to large variations in power delivery with input voltage that must be addressed (e.g., through oversizing of the inverter components and use of frequency control to modulate power). However, since the effective conductance seen by the inverters in the ICN converter (operated at near zero effective susceptance) decreases with input voltage (see Fig. 2.4 and Fig. 2.5), the variation in output power with input voltage can be made quite limited across a wide input voltage range, as shown in Fig. 2.6, and expressed mathematically as:

$$P_{\mathrm{OUT}} = \frac{4V_{\mathrm{IN}}\sqrt{V_{\mathrm{OUT}}^2 - N^2V_{\mathrm{IN}}^2}}{\pi^2 NX} \quad . \tag{2.3}$$

This expression is derived assuming a lossless converter and utilizing (2.1) and (2.2), i.e., under fundamental frequency approximation. Appendix A provides the derivation of (2.3). The limited variation in output power with input voltage enables improved sizing of inverter components and use of fixed-frequency operation, with consequent benefits for efficiency. Output power of the converter can be further controlled (for values below that indicated in Fig. 2.6) using burst mode (on/off) control, in which the operation of the converter is modulated on and off at a frequency much lower than its switching frequency [19]-[21]. On/off control is desirable because converter losses back off proportionally to power delivered, thus enabling efficient operation to be maintained over a wide power range. Thus, with the proposed architecture we are able to achieve wide voltage and power range operation at fixed switching frequency and high efficiency.

2.3 Comparison of ICN with RCN Converter

It is instructive to consider the similarities and differences between the ICN converter and a resistance compression network (RCN) converter [15]. They both use burst mode control to regulate output voltage and power, and both can maintain ZVS and near ZCS across a wide range of input voltage, output voltage and power levels. However, while RCN converter utilizes a power splitting network in the rectification

stage, the ICN converter uses a power combining network in the inversion stage. The power splitting network of the RCN converter compresses the change in impedance seen by its inverter even though the effective rectifier resistance changes due to variations in input voltage and output power. In a sense, while the RCN converter offers passive compression of its impedance seen by its inverters, the ICN converter offers active control of the impedances of its inverters. A major practical difference between the ICN and RCN-based approaches is in terms of the variations in their maximum output power characteristics with respect to input and output voltages.

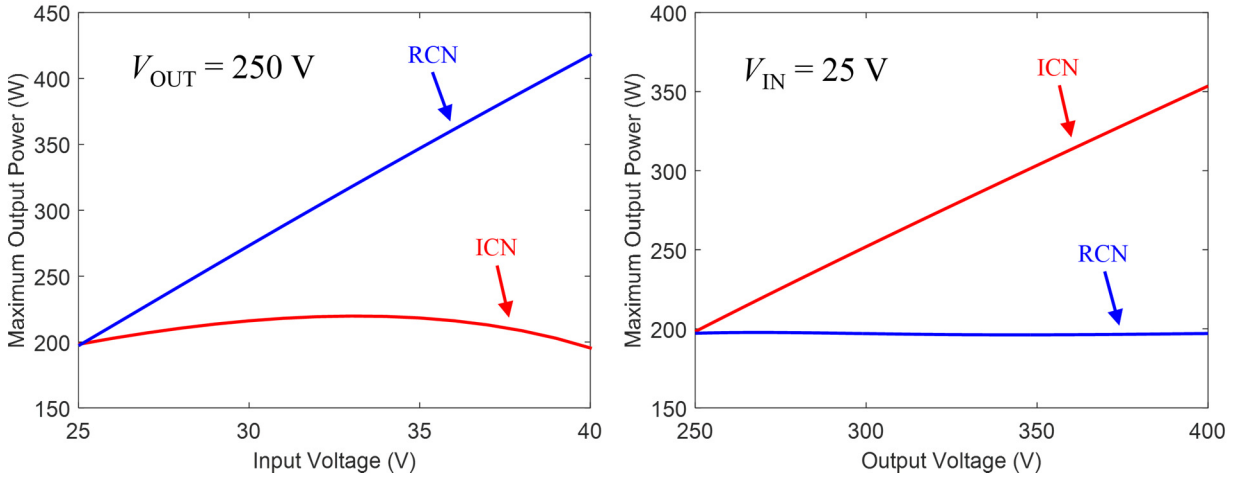

(a) (b)

Figure 2.7: Maximum output power delivered by the ICN converter and the RCN converter against (a) an input voltage range from 25 V to 40 V, and (b) an output voltage range from 250 V to 400 V. The switching frequency used in both cases is 500 kHz.

The maximum output power of the RCN converter is highly invariant to output voltage, while the maximum output power of the ICN converter is highly invariant to input voltage, as can be seen in Fig. 2.7. Figure 2.7 (a) compares the maximum output power delivered by the ICN converter and a RCN converter designed to meet the same specifications as a function of input voltage. The variation in the maximum output power of the ICN converter is quite limited across the entire input voltage range, while that of the RCN converter

increases linearly with input voltage. At the maximum input voltage, the maximum output power of the RCN converter is over twice that of the ICN converter. Figure 2.7 (b) compares the maximum output power delivered by the two converters as a function of output voltage. Now the maximum output power delivered by the RCN converter is nearly constant, while the maximum output power of the ICN converter increases monotonically with output voltage. At the maximum output voltage, the ICN converter delivers maximum output power that is 1.75 times larger than that of the RCN converter. Thus, the ICN converter is more suitable for applications having large variations in input voltages, while the RCN converter is more suitable for applications where the output voltage has large variations.

Chapter 3

Step-Superposition (S2) Analysis

3.1 Conventional Analysis Techniques for Resonant Converters

Resonant converters are typically analyzed and designed using fundamental frequency analysis [4], wherein network waveforms are approximated by their fundamental components and switching frequency harmonics are neglected. This modeling method simplifies the design of resonant converters as it converts the nonlinear power converter into an approximately equivalent linear circuit. However, this approach becomes inaccurate when the converter tank waveforms are significantly non-sinusoidal, as is often the case when the quality factor (Q) of the resonant network is low. There are two related general approaches for exact analysis of resonant converters: state space analysis, and state plane analysis. State space analysis identifies the operating modes of a resonant converter over one switching cycle, and solves the state vectors recursively from one mode to the next [26]-[28]. State space analysis is an accurate and general approach to the analysis of resonant converters, but it requires complicated and time-consuming matrix computations. On the other hand, state plane analysis converts the time-domain analysis of resonant converters to geometrical analysis, where tank waveforms are described using segments of circles, lines or ellipses [29]-[30]. Through such graphical representations, state plane analysis simplifies the exact analysis of complicated resonant tank behavior. However, its application is practically limited to simple resonant converters (e.g., with up to two to three tank elements). To analyze high-order resonant converters with multiple tank elements, this method needs to employ complicated higher-dimensional or multiple two-dimensional state planes and becomes difficult to use. Furthermore, both of the above-mentioned exact modeling approaches require finding all the operating modes of the resonant converter, which is not straightforward particularly for high-order resonant converter topologies with multiple inverters and/or rectifiers. Therefore, there is a need for an exact, yet general and easily-applicable method for modeling topologically advanced high-order resonant converters.

3.2 Step-Superposition (S2) Analysis

This chapter introduces a new analysis approach to modeling resonant converters that can be used to determine closed-form expressions for the exact resonant network waveforms. This approach, based on superposition of step responses to inverter and rectifier imposed steps, can easily be applied to resonant converters with high-order resonant networks, multiple inverters and/or rectifiers. The usefulness of the proposed analysis approach is demonstrated by applying it to a series resonant converter and the proposed impedance control network (ICN) resonant converter [31]-[40]. The modeling results are validated using a 200 W, 500 kHz ICN resonant converter [31]. It is shown that there is an excellent agreement between the experimental and modeled waveforms during steady-state operation and during startup transients.

To understand the proposed step-superposition analysis approach, consider the general architecture of a voltage-fed, voltage-loaded dc-dc resonant converter shown in Fig. 3.1(a). This architecture comprises an inversion stage with one or more inverters, a transformation stage with a resonant network, and a rectification stage with one or more rectifiers. In the proposed analysis approach, the inverter output

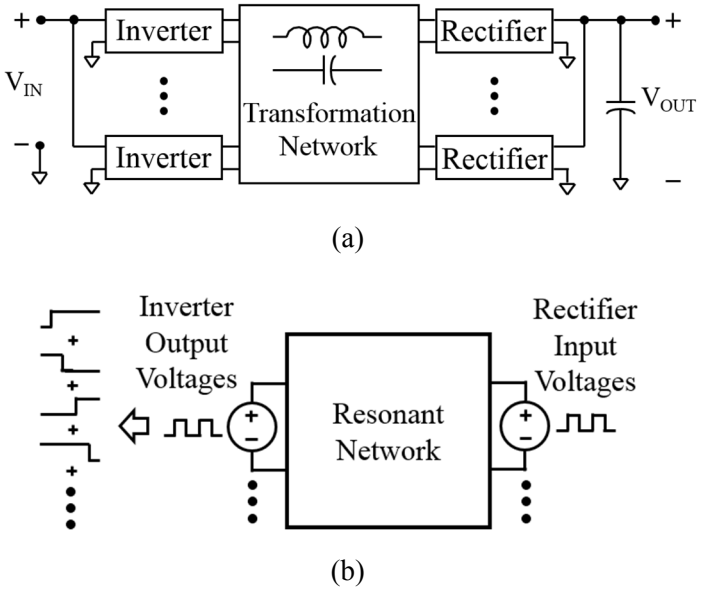

Figure 3.1: A voltage-fed voltage-loaded dc-dc resonant converter: (a) general architecture; and (b) proposed analysis method using a step-superposition model. In the proposed approach the inverter output voltages and rectifier input voltages are modeled as rectangular-wave sources, which are further modeled as series of time-shifted positive and negative steps.

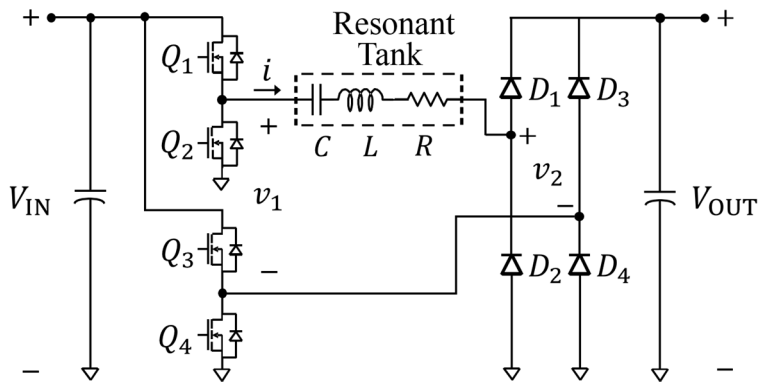

Figure 3.2: A full-bridge series resonant converter. V_{IN} is the input voltage and V_{OUT} is the output voltage.

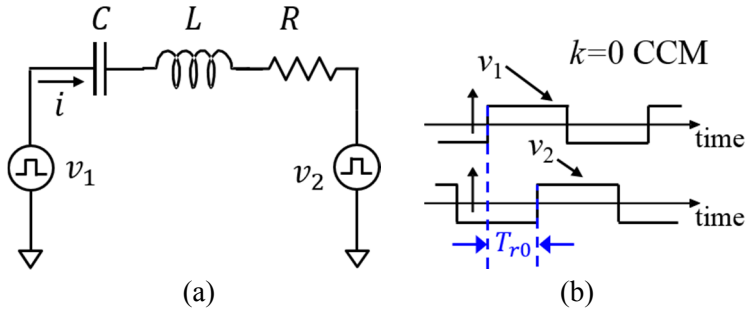

Figure 3.3: The equivalent model of the full-bridge series resonant converter of Fig. 2, together with waveforms of the equivalent voltage sources.

voltages and rectifier input voltages are modeled as rectangular-wave sources as shown in Fig. 3.1(b). The response of the resonant network is obtained for each source, with the other sources set to zero. To compute this single-source response, the rectangular-wave source is further decomposed into a sum of time-shifted positive and negative steps. The tank response to each step is obtained and summed to get the full single-source response. Finally, all the single-source responses are superposed to obtain the complete response of the resonant network in the presence of all inverter and rectifier sources. Note that the summation of steps and superposition of responses are performed under the implicit assumption that the resonant network is linear time-invariant (LTI). In view of salient features of this approach as described above, it is termed step-superposition (S2) analysis.

3.3 Application of S2 Analysis to Series Resonant Converter (SRC)

To better understand the S2 analysis approach, the simple example of a full-bridge series resonant converter (SRC) is considered. The converter topology is shown in Fig. 3.2. The SRC can operate in different modes: the above-resonance mode and several below-resonance modes. In this section, S2 analysis is applied to two example modes of SRC to demonstrate its usefulness.

3.3.1 SRC Operating in Above-Resonance Mode

In this subsection, the converter is assumed to operate above resonance (that is, in the *k*=0 Continuous Conduction Mode (CCM), [41]), where the inverter output current lags the inverter output voltage, and the inverter transistors are switched at 50% duty ratio. Figure 3.3(a) shows the equivalent model for the converter of Fig. 3.2 with all voltages imposed on the resonant network (i.e., the inverter output voltage v_1 and the rectifier input voltage v_2 of Fig. 3.2) modeled by square-wave sources (50% duty ratio). These voltages (v_1 and v_2) are plotted in Fig. 3.3(b), where T_{r0} is defined as the phase lag of the rectifier input voltage with respect to the inverter output voltage. These sources can be decomposed into a sum of time-shifted positive and negative steps, as given by:

$$v_1(t) = \begin{cases} V_{\mathrm{IN0}} - (V_{\mathrm{IN}} + V_{\mathrm{IN0}})u(\mathrm{t}) + \sum_{m=0}^{K-1} 2V_{\mathrm{IN}}u(t'_{\mathrm{K}} + mT_{\mathrm{s}}) - \\ \sum_{m=1}^{K-1} 2V_{\mathrm{IN}}u\left(t'_{\mathrm{K}} - \frac{T_{\mathrm{s}}}{2} + mT_{\mathrm{s}}\right) & , \ 0 \le t'_{\mathrm{K}} < \frac{T_{\mathrm{s}}}{2} \\ V_{\mathrm{IN0}} - (V_{\mathrm{IN}} + V_{\mathrm{IN0}})u(\mathrm{t}) + \sum_{m=0}^{K-1} 2V_{\mathrm{IN}}u(t'_{\mathrm{K}} + mT_{\mathrm{s}}) - \\ \sum_{m=0}^{K-1} 2V_{\mathrm{IN}}u\left(t'_{\mathrm{K}} - \frac{T_{\mathrm{s}}}{2} + mT_{\mathrm{s}}\right) & , \ \frac{T_{\mathrm{s}}}{2} \le t'_{\mathrm{K}} < T_{\mathrm{s}} \end{cases}, \tag{3.1}$$

$$v_2(t) = \begin{cases} V_{\mathrm{OUT0}} - (V_{\mathrm{OUT}} + V_{\mathrm{OUT0}})u(t - T_{\mathrm{r0}}) + \sum_{m=1}^{K-1} 2V_{\mathrm{OUT}}u(t'_{\mathrm{K}} - T_{\mathrm{r0}} + mT_{\mathrm{s}}) - \\ \sum_{m=1}^{K-1} 2V_{\mathrm{OUT}}u\left(t'_{K} - T_{\mathrm{r0}} - \frac{T_{\mathrm{s}}}{2} + mT_{\mathrm{s}}\right) & , \ 0 \le t'_{\mathrm{K}} < T_{\mathrm{r0}} \\ V_{\mathrm{OUT0}} - (V_{\mathrm{OUT}} + V_{\mathrm{OUT0}})u(t - T_{\mathrm{r0}}) + \sum_{m=0}^{K-1} 2V_{\mathrm{OUT}}u(t'_{K} - T_{\mathrm{r0}} + mT_{\mathrm{s}}) - \\ \sum_{m=1}^{K-1} 2V_{\mathrm{OUT}}u\left(t'_{K} - T_{\mathrm{r0}} - \frac{T_{\mathrm{s}}}{2} + mT_{\mathrm{s}}\right) & , \ T_{\mathrm{r0}} \le t'_{\mathrm{K}} < T_{\mathrm{r0}} + \frac{T_{\mathrm{s}}}{2} \\ V_{\mathrm{OUT0}} - (V_{\mathrm{OUT}} + V_{\mathrm{OUT0}})u(t - T_{\mathrm{r0}}) + \sum_{m=0}^{K-1} 2V_{\mathrm{OUT}}u(t'_{\mathrm{K}} - T_{\mathrm{r0}} + mT_{\mathrm{s}}) - \\ \sum_{m=0}^{K-1} 2V_{\mathrm{OUT}}u\left(t'_{\mathrm{K}} - T_{\mathrm{r0}} - \frac{T_{\mathrm{s}}}{2} + mT_{\mathrm{s}}\right) & , \ T_{\mathrm{r0}} + \frac{T_{\mathrm{s}}}{2} \le t'_{\mathrm{K}} < T_{\mathrm{s}} \end{cases} \tag{3.2}$$

Here, V_{IN0} is the initial value of the input voltage, V_{OUT0} is the initial value of the output voltage, t is taken to be zero when the converter is turned on, T_{s} is the switching period of the converter, K (=1, 2, …) is the

number of the switching cycle of interest (the K^{th} switching cycle), and t'_{K} is the time elapsed within the switching cycle of interest. The relationship between t, t'_{K} and K is given by:

$$t'_{\text{K}} = t - (K-1)T_{\text{s}}. \tag{3.3}$$

The response of the tank current, $y_{\text{u}}(t)$, to a unit step assuming very low damping ($R \approx 0$) is given by:

$$y_{\text{u}}(t) = \frac{1}{\omega_{\text{d}} L} e^{-\alpha t} \sin \omega_{\text{d}} t, \tag{3.4}$$

where $\alpha = \frac{R}{2L}$ and $\omega_{\text{d}} = \sqrt{\frac{1}{LC} - \left(\frac{R}{2L}\right)^2}$. Each step in (3.1) and (3.2) excites a similar current response and the components i_1 and i_2 of the tank current i, generated by the two voltage sources v_1 and v_2, respectively, can be obtained by adding the individual responses:

$$i_1(t) = \begin{cases} -(V_{\text{IN}} + V_{\text{IN0}}) y_{\text{u}}(t) + \sum_{m=0}^{K-1} 2V_{\text{IN}} y_{\text{u}}(t'_{\text{K}} + mT_{\text{s}}) - \\ \sum_{m=1}^{K-1} 2V_{\text{IN}} y_{\text{u}}\left(t'_{\text{K}} - \frac{T_{\text{s}}}{2} + mT_{\text{s}}\right) \end{cases}, \quad 0 \le t'_{\text{K}} < \frac{T_{\text{s}}}{2}$$
$$\begin{cases} -(V_{\text{IN}} + V_{\text{IN0}}) y_{\text{u}}(t) + \sum_{m=0}^{K-1} 2V_{\text{IN}} y_{\text{u}}(t'_{\text{K}} + mT_{\text{s}}) - \\ \sum_{m=0}^{K-1} 2V_{\text{IN}} y_{\text{u}}\left(t'_{\text{K}} - \frac{T_{\text{s}}}{2} + mT_{\text{s}}\right) \end{cases}, \quad \frac{T_{\text{s}}}{2} \le t'_{\text{K}} < T_{\text{s}} \tag{3.5}$$

$$i_2(t) = \begin{cases} (V_{\text{OUT}} + V_{\text{OUT0}}) y_{\text{u}}(t - T_{\text{r0}}) - \sum_{m=1}^{K-1} 2V_{\text{OUT}} y_{\text{u}}(t'_{\text{K}} - T_{\text{r0}} + mT_{\text{s}}) + \\ \sum_{m=1}^{K-1} 2V_{\text{OUT}} y_{\text{u}}\left(t'_{\text{K}} - T_{\text{r0}} - \frac{T_{\text{s}}}{2} + mT_{\text{s}}\right) \end{cases}, \quad 0 \le t'_K < T_{\text{r0}}$$
$$\begin{cases} (V_{\text{OUT}} + V_{\text{OUT0}}) y_{\text{u}}(t - T_{\text{r0}}) - \sum_{m=0}^{K-1} 2V_{\text{OUT}} y_{\text{u}}(t'_{\text{K}} - T_{\text{r0}} + mT_{\text{s}}) + \\ \sum_{m=1}^{K-1} 2V_{\text{OUT}} y_{\text{u}}\left(t'_{\text{K}} - T_{\text{r0}} - \frac{T_{\text{s}}}{2} + mT_{\text{s}}\right) \end{cases}, \quad T_{\text{r0}} \le t'_{\text{K}} < T_{\text{r0}} + \frac{T_{\text{s}}}{2}.$$
$$\begin{cases} (V_{\text{OUT}} + V_{\text{OUT0}}) y_{\text{u}}(t - T_{\text{r0}}) - \sum_{m=0}^{K-1} 2V_{\text{OUT}} y_{\text{u}}(t'_{\text{K}} - T_{\text{r0}} + mT_{\text{s}}) + \\ \sum_{m=0}^{K-1} 2V_{\text{OUT}} y_{\text{u}}\left(t'_{\text{K}} - T_{\text{r0}} - \frac{T_{\text{s}}}{2} + mT_{\text{s}}\right) \end{cases}, \quad T_{\text{r0}} + \frac{T_{\text{s}}}{2} \le t'_{\text{K}} < T_{\text{s}} \tag{3.6}$$

The summations in (3.5) and (3.6) can be simplified under low damping condition using Euler's identity, trigonometric identities and geometric series analysis to yield a closed-form expression for the steady-state tank current $i(t) = i_1(t) + i_2(t)$, where:

$$i_1(t) = \begin{cases} \frac{V_{\text{IN}}}{\omega_{\text{d}} L} \frac{\sin\left(\omega_{\text{d}} t'_{\text{K}} - \frac{1}{4}\omega_{\text{d}} T_{\text{s}}\right)}{2\cos\left(\frac{\omega_{\text{d}} T_{\text{s}}}{4}\right)}, & 0 \le t'_{\text{K}} < \frac{T_{\text{s}}}{2} \\ \frac{V_{\text{IN}}}{\omega_{\text{d}} L} \frac{\sin\left(\frac{3}{4}\omega_{\text{d}} T_{\text{s}} - \omega_{\text{d}} t'_{\text{K}}\right)}{2\cos\left(\frac{\omega_{\text{d}} T_{\text{s}}}{4}\right)}, & \frac{T_{\text{s}}}{2} \le t'_{\text{K}} < T_{\text{s}} \end{cases}, \tag{3.7}$$

$$i_2(t) = \begin{cases} -\frac{V_{OUT}}{\omega_d L}\frac{\sin\left(-\omega_d t'_K - \frac{1}{4}\omega_d T_s + \omega_d T_{r0}\right)}{2\cos\left(\frac{\omega_d T_s}{4}\right)}, & 0 \le t'_K < T_{r0} \\ -\frac{V_{OUT}}{\omega_d L}\frac{\sin\left(\omega_d t'_K - \frac{1}{4}\omega_d T_s - \omega_d T_{r0}\right)}{2\cos\left(\frac{\omega_d T_s}{4}\right)}, & T_{r0} \le t'_K < T_{r0} + \frac{T_s}{2} \\ -\frac{V_{OUT}}{\omega_d L}\frac{\sin\left(-\omega_d t'_K + \frac{3}{4}\omega_d T_s + \omega_d T_{r0}\right)}{2\cos\left(\frac{\omega_d T_s}{4}\right)}, & T_{r0} + \frac{T_s}{2} \le t'_K < T_s \end{cases}. \quad (3.8)$$

The initial step responses at the beginning of the converter's operation die out in steady state, so (3.7) and (3.8) are independent of initial voltages. Detailed derivations of the closed-form expression for the summations in (3.7) and (3.8) are provided in Appendix B.

The phase lag of the rectifier (T_{r0}) can be obtained using the fact that at $t'_K = T_{r0}$, rectifier switches commutate and the tank current at this time instant is zero. Hence, T_{r0} is given by:

$$T_{r0} = \frac{\arcsin\left(-\frac{V_{OUT}}{V_{IN}}\sin\left(\frac{\omega_d T_s}{4}\right)\right) + \frac{\omega_d T_s}{4}}{\omega_d}. \quad (3.9)$$

The above application of the S2 analysis pertains to the steady-state operation of the series resonant converter. However, the S2 analysis is a general method that can be used to compute the startup transients of the converter as well, as will be shown in Section 3.4.

A comparison of the modeled and LTSpice-simulated steady-state tank current waveforms for the SRC operating in above-resonance mode is shown in Fig. 3.4, where the converter is operated with 100 V input

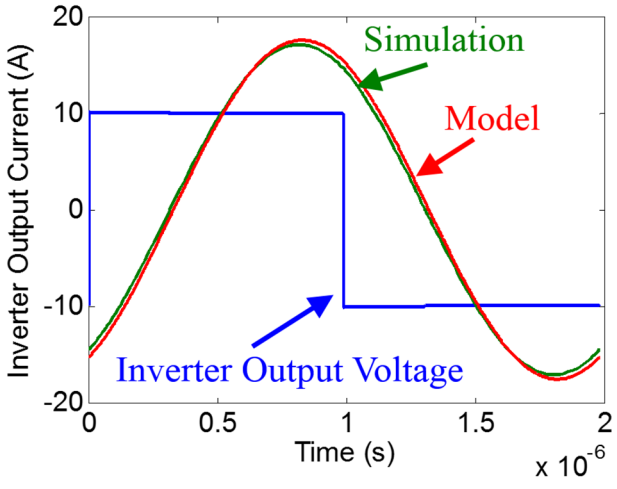

Figure 3.4: Comparison of modeled and simulated tank current waveforms of the series resonant converter operating in steady state with 100 V input voltage, 50 V output voltage and 505 kHz switching frequency. The values of the tank components are $L = 100$ µH and $C = 1.0132$ nF.

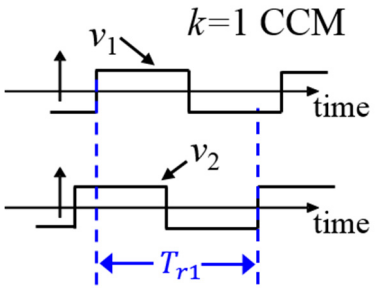

Figure 3.5: Waveforms of the inverter output voltage (v_1) and rectifier input voltage (v_2).

voltage, 50 V output voltage and 505 kHz switching frequency. The values of the tank components are $L = 100$ μH and $C = 1.0132$ nF. The simulated tank current matches the modeled tank current to a high degree of accuracy.

3.3.2 SRC Operating in Below-Resonance Mode

In this subsection, S2 analysis is applied to the SRC operating in below-resonance mode. Without loss of generality, we consider the most commonly used below-resonance mode - *k*=1 CCM mode, where f_s is lower than f_0, but higher than $f_0/2$ [41].

For k=1 CCM mode, the inverter output voltage (v_1) is plotted along with the rectifier input voltage (v_2) in Fig. 3.5, where T_{r1} (larger than $T_s/2$) is the phase lag of the rectifier input voltage with respect to the inverter output voltage. The voltage v_1 is the same as the previous case and given by (3.1). The voltage v_2 is given by:

$$v_2(t) = \begin{cases} V_{OUT0} - (V_{OUT} + V_{OUT0})u(t - T_{r1}) + \sum_{m=1}^{K-1} 2V_{OUT}u(t'_K - T_{r1} + mT_s) - \\ \sum_{m=1}^{K-1} 2V_{OUT}u\left(t'_K - T_{r1} + \frac{T_s}{2} + mT_s\right) \end{cases}, \; 0 \le t'_K < T_{r1} - \frac{T_s}{2}$$

$$\begin{cases} V_{OUT0} - (V_{OUT} + V_{OUT0})u(t - T_{r1}) + \sum_{m=1}^{K-1} 2V_{OUT}u(t'_K - T_{r1} + mT_s) - \\ \sum_{m=0}^{K-1} 2V_{OUT}u\left(t'_K - T_{r1} + \frac{T_s}{2} + mT_s\right) \end{cases}, T_{r1} - \frac{T_s}{2} \le t'_K < T_{r1}.$$

$$\begin{cases} V_{OUT0} - (V_{OUT} + V_{OUT0})u(t - T_{r1}) + \sum_{m=0}^{K-1} 2V_{OUT}u(t'_K - T_{r1} + mT_s) - \\ \sum_{m=0}^{K-1} 2V_{OUT}u\left(t'_K - T_{r1} + \frac{T_s}{2} + mT_s\right), \end{cases} \; T_{r1} \le t'_K < T_s \tag{3.10}$$

Similarly, the component i_1 of tank current i is given by (3.5) and (3.7). The component i_2 of tank current i is given by:

$$i_2(t)=\begin{cases}(V_{\mathrm{OUT}}+V_{\mathrm{OUT0}})y_{\mathrm{u}}(t-T_{\mathrm{r1}})-\sum_{m=1}^{K-1}2V_{\mathrm{OUT}}y_{\mathrm{u}}(t'_{\mathrm{K}}-T_{\mathrm{r1}}+mT_{\mathrm{s}})+\\ \sum_{m=1}^{K-1}2V_{\mathrm{OUT}}y_{\mathrm{u}}\left(t'_{\mathrm{K}}-T_{\mathrm{r1}}+\frac{T_{\mathrm{s}}}{2}+mT_{\mathrm{s}}\right) & ,\ 0\le t'_{\mathrm{K}}<T_{\mathrm{r1}}-\frac{T_{\mathrm{s}}}{2}\\ (V_{\mathrm{OUT}}+V_{\mathrm{OUT0}})y_{\mathrm{u}}(t-T_{\mathrm{r1}})-\sum_{m=1}^{K-1}2V_{\mathrm{OUT}}y_{\mathrm{u}}(t'_{\mathrm{K}}-T_{\mathrm{r1}}+mT_{\mathrm{s}})+\\ \sum_{m=0}^{K-1}2V_{\mathrm{OUT}}y_{\mathrm{u}}\left(t'_{\mathrm{K}}-T_{\mathrm{r1}}+\frac{T_{\mathrm{s}}}{2}+mT_{\mathrm{s}}\right) & ,\ T_{\mathrm{r1}}-\frac{T_{\mathrm{s}}}{2}\le t'_{\mathrm{K}}<T_{\mathrm{r1}}.\\ (V_{\mathrm{OUT}}+V_{\mathrm{OUT0}})y_{\mathrm{u}}(t-T_{\mathrm{r1}})-\sum_{m=0}^{K-1}2V_{\mathrm{OUT}}y_{\mathrm{u}}(t'_{\mathrm{K}}-T_{\mathrm{r1}}+mT_{\mathrm{s}})+\\ \sum_{m=0}^{K-1}2V_{\mathrm{OUT}}y_{\mathrm{u}}\left(t'_{\mathrm{K}}-T_{\mathrm{r1}}+\frac{T_{\mathrm{s}}}{2}+mT_{\mathrm{s}}\right) & ,\ T_{\mathrm{r1}}\le t'_{\mathrm{K}}<T_{\mathrm{s}}\end{cases}$$

(3.11)

Using the results in the Appendix B, the simplified expression of i_2 in steady state is:

$$i_2(t)=\begin{cases}-\frac{V_{\mathrm{OUT}}}{\omega_{\mathrm{d}}L}\frac{\sin\left(\omega_{\mathrm{d}}t'_{\mathrm{K}}+\frac{3}{4}\omega_{\mathrm{d}}T_{\mathrm{s}}-\omega_{\mathrm{d}}T_{\mathrm{r1}}\right)}{2\cos\left(\frac{\omega_{\mathrm{d}}T_{\mathrm{s}}}{4}\right)}, & 0\le t'_{\mathrm{K}}<T_{\mathrm{r1}}-\frac{T_{\mathrm{s}}}{2}\\ -\frac{V_{\mathrm{OUT}}}{\omega_{\mathrm{d}}L}\frac{\sin\left(-\omega_{\mathrm{d}}t'_{\mathrm{K}}-\frac{1}{4}\omega_{\mathrm{d}}T_{\mathrm{s}}+\omega_{\mathrm{d}}T_{\mathrm{r1}}\right)}{2\cos\left(\frac{\omega_{\mathrm{d}}T_{\mathrm{s}}}{4}\right)}, & T_{\mathrm{r1}}-\frac{T_{\mathrm{s}}}{2}\le t'_{\mathrm{K}}<T_{\mathrm{r1}}.\\ -\frac{V_{\mathrm{OUT}}}{\omega_{\mathrm{d}}L}\frac{\sin\left(\omega_{\mathrm{d}}t'_{\mathrm{K}}-\frac{1}{4}\omega_{\mathrm{d}}T_{\mathrm{s}}-\omega_{\mathrm{d}}T_{\mathrm{r1}}\right)}{2\cos\left(\frac{\omega_{\mathrm{d}}T_{\mathrm{s}}}{4}\right)}, & T_{\mathrm{r1}}\le t'_{\mathrm{K}}<T_{\mathrm{s}}\end{cases}$$

(3.12)

Again, the complete tank current is simply given by $i(t)=i_1(t)+i_2(t)$. Evaluating the full tank current at the rectifier commutation time instant (T_{r1}) yields the expression for T_{r1}:

$$T_{\mathrm{r1}}=\frac{\arcsin\left(\frac{V_{\mathrm{OUT}}}{V_{\mathrm{IN}}}\sin\left(\frac{\omega_{\mathrm{d}}T_{\mathrm{s}}}{4}\right)\right)+\frac{3\omega_{\mathrm{d}}T_{\mathrm{s}}}{4}}{\omega_{\mathrm{d}}}.$$

(3.13)

This concludes deriving the expressions for the tank current of SRC when operating in *k*=1 CCM.

3.3.3 S2 Analysis Predicted Output Power

The tank current can be used to derive the output power of the converter. Assuming lossless power conversion, the output power can be derived by averaging the instantaneous input power over one complete switching period. Hence, the output power of the SRC is given by:

$$P_{\mathrm{OUT}}=2f_{\mathrm{s}}V_{\mathrm{IN}}\int_0^{\frac{T_{\mathrm{s}}}{2}}i(t)\cdot dt.$$

(3.14)

Substituting the expression of $i(t)$ into (3.14), gives the following closed-form expression for the output power of the SRC operating in the *k*=0 CCM mode:

$$P_{\mathrm{OUT0}}=\frac{4V_{\mathrm{IN}}V_{\mathrm{OUT}}f_{\mathrm{s}}}{\omega_{\mathrm{d}}^2L}\left[\frac{\cos\left(\frac{\omega_{\mathrm{d}}T_{\mathrm{s}}}{4}-\omega_{\mathrm{d}}T_{\mathrm{r0}}\right)}{\cos\frac{\omega_{\mathrm{d}}T_{\mathrm{s}}}{4}}-1\right],$$

(3.15)

where T_{r0} is the phase lag of the rectifier input voltage and is given by (3.9). For the SRC operating in the k=1 CCM mode, the closed-form expression for the output power is given by:

$$P_{OUT1} = \frac{4V_{IN}V_{OUT}f_s}{\omega_d^2 L}\left[1 - \frac{\cos\left(\omega_d T_{r1} - \frac{3\omega_d T_s}{4}\right)}{\cos\frac{\omega_d T_s}{4}}\right]. \tag{3.16}$$

Here, T_{r1} is the phase lag of the rectifier input voltage and is given by (3.13).

To demonstrate the effectiveness of the above modeling results, the SRC of Fig. 3.2 is simulated for two switching frequencies – 490 kHz and 505 kHz. Similar to the previous section, the converter is operated with 100 V input voltage and 50 V output voltage. The values of the tank components are $L = 100$ µH and $C = 1.0132$ nF, which correspond to a resonant frequency of 500 kHz. For the 490 kHz case, the output power calculated by (3.16) is 278.3 W. When operating at 505 kHz, the output power calculated by (3.15) is 559.7 W. For comparison, the LTSpice-simulated output power of the SRC is 277.5 W and 553.4 W for 490 kHz and 505 kHz, respectively. It is clear that there is excellent agreement between the modeled and simulated output power.

3.4 Application of S2 Analysis to ICN Resonant Converter

As stated earlier, the S2 analysis can be readily applied to high-order resonant converters with advanced topologies. In this section, S2 analysis is applied to the impedance control network (ICN) resonant converter, which is a multi-inverter multi-element resonant converter. The ICN converter is capable of maintaining zero voltage switching (ZVS) and near zero current switching (ZCS) across wide operating ranges. The ICN converter introduced in [31] is shown in Fig. 3.6. This converter is operated at a fixed frequency and each inverter is operated at a fixed duty ratio (~50%). A combination of phase-shift control (for inverters) and burst mode control (in which the converter is modulated on and off at a frequency much lower than its switching frequency) is used to regulate the output voltage and power of the ICN converter.

The equivalent model for the ICN converter of Fig. 3.6 is shown in Fig. 3.7, where the three voltage sources imposed on the resonant network are modeled by square-wave voltage sources. Similar to (3.1) and (3.2), these square-wave sources can be modeled by series of positive and negative steps. The single-source step responses of the tank currents have the following form:

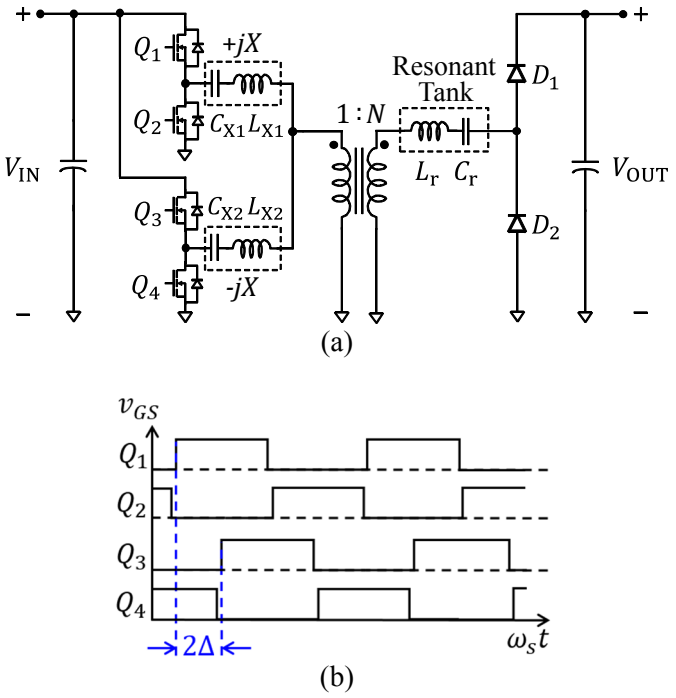

Figure 3.6: One example impedance control network (ICN) resonant converter [31], appropriate for voltage step-up: (a) converter topology and (b) switch gating signals.

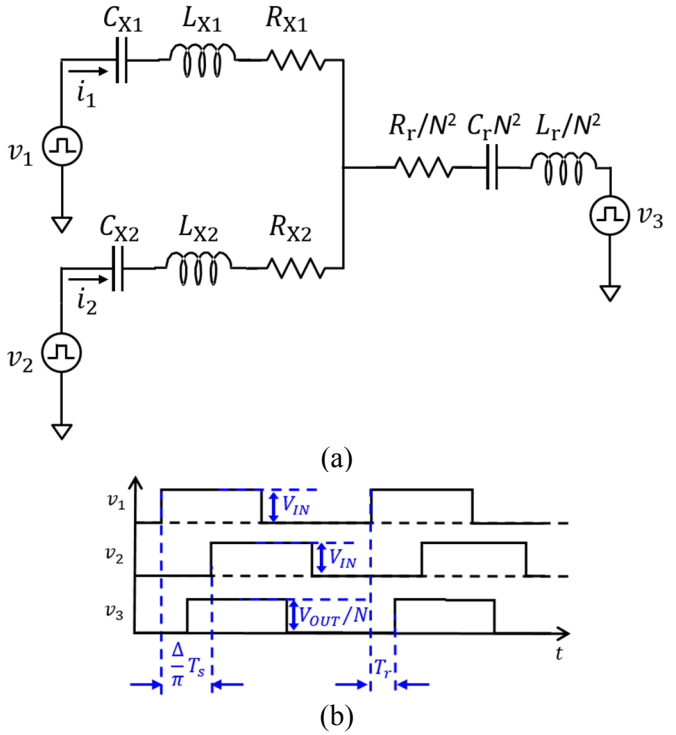

Figure 3.7: Equivalent circuit model for the ICN converter of Fig. 3.6. The resistors model converter losses. Waveforms of voltage sources are shown in (b).

$$i_{\mathrm{u,xy}}(t) = I_{\mathrm{xy1}} e^{-\alpha_1 t} \sin \omega_1 t + I_{\mathrm{xy2}} e^{-\alpha_2 t} \sin \omega_2 t, \tag{3.17}$$

where $i_{\mathrm{u,xy}}(t)$ is the step response of i_{x} to v_{y} (x is 1 or 2, and y is 1, 2 or 3), I_{xy1}, I_{xy2}, α_1, α_2, ω_1 and ω_2 are parameters that depend on input voltage, output voltage, reactive component values, transformer turns ratio and converter losses. The full expressions for these parameters are provided at the end of Appendix C. The two tank currents, i_1 and i_2 (as shown in Fig. 3.7(a)), can be obtained by the superposition of the three single-source responses, as follows:

$$\begin{aligned} i_1(t) &= i_{11}(t) + i_{12}(t) + i_{13}(t), \\ i_2(t) &= i_{21}(t) + i_{22}(t) + i_{23}(t). \end{aligned} \tag{3.18}$$

Here, $i_{\mathrm{xy}}(t)$ is the component of i_{x} generated by v_{y} (x is 1 or 2, and y is 1, 2 or 3). Full expressions for the tank currents are provided in Appendix B. As an example, when the ICN converter is operating in steady state, $i_{11}(t)$ is given by:

$$i_{11}(t) = \begin{cases} \frac{I_{111}\sin\left(\omega_1 t'_{\mathrm{K}} - \frac{\omega_1 T_{\mathrm{s}}}{4}\right)}{2\cos\left(\frac{\omega_1 T_{\mathrm{s}}}{4}\right)} + \frac{I_{112}\sin\left(\omega_2 t'_{\mathrm{K}} - \frac{\omega_2 T_{\mathrm{s}}}{4}\right)}{2\cos\left(\frac{\omega_2 T_{\mathrm{s}}}{4}\right)}, 0 \le t'_{\mathrm{K}} < \frac{T_{\mathrm{s}}}{2} \\ \frac{I_{111}\sin\left(\frac{3\omega_1 T_{\mathrm{s}}}{4} - \omega_1 t'_{\mathrm{K}}\right)}{2\cos\left(\frac{\omega_1 T_{\mathrm{s}}}{4}\right)} + \frac{I_{112}\sin\left(\frac{3\omega_2 T_{\mathrm{s}}}{4} - \omega_2 t'_{\mathrm{K}}\right)}{2\cos\left(\frac{\omega_2 T_{\mathrm{s}}}{4}\right)}, \frac{T_{\mathrm{s}}}{2} \le t'_{\mathrm{K}} < T_{\mathrm{s}} \end{cases}, \tag{3.19}$$

Here, t is taken to be zero when the converter is turned on, T_{s} is the switching period of the converter, K (=1, 2, …) is the number of the switching cycle of interest (the K^{th} switching cycle), and t'_{K} is the time elapsed within the switching cycle of interest.

The ideal phase lag (T_{r}) of the rectifier is found at the instant $t'_{\mathrm{K}} = T_{\mathrm{r}}$, when the rectifier current ($i_1 + i_2$) is zero and the rectifier switches commutate. It may be noted that the charging and discharging of the parasitic capacitances of the actual rectifier diodes during the switching transitions introduces extra delay into T_{r}. This delay, ΔT_{r}, can be approximated by the time required to discharge the parasitic capacitances of the rectifier diodes to half of the output voltage and can be obtained as:

$$\int_{T_{\mathrm{r}}}^{T_{\mathrm{r}}+\Delta T_{\mathrm{r}}} \frac{i_1+i_2}{N}\, dt = 2C_{\mathrm{diode}} V_{\mathrm{OUT}} \times \frac{1}{2}, \tag{3.20}$$

where N is the transformer turns ratio and C_{diode} is the parasitic capacitance of the rectifier diode. This equation neglects the slight change in the rectifier input current during the delay (ΔT_{r}) and calculates the

charge needed to bring the rectifier input voltage to one half of the output voltage. The actual phase lag of the rectifier is given by $T_{\mathrm{r}} + \Delta T_{\mathrm{r}}$.

When the converter is operating in burst mode, $i_{11}(t)$ will have an additional transient component, as given by:

$$i_{11\mathrm{t}}(t) = -\frac{V_{1,0}}{V_{\mathrm{IN}}} i_{\mathrm{u},11}(t) - \frac{I_{111} e^{-(N-1)\alpha_1 T_{\mathrm{s}}} \sin\left(-\omega_1 t'_{\mathrm{K}} + \frac{3\omega_1 T_{\mathrm{s}}}{4} - N\omega_1 T_{\mathrm{s}}\right)}{2\cos\left(\frac{\omega_1 T_{\mathrm{s}}}{4}\right)} - \frac{I_{112} e^{-(N-1)\alpha_2 T_{\mathrm{s}}} \sin\left(-\omega_2 t'_{\mathrm{K}} + \frac{3\omega_2 T_{\mathrm{s}}}{4} - N\omega_2 T_{\mathrm{s}}\right)}{2\cos\left(\frac{\omega_2 T_{\mathrm{s}}}{4}\right)}. \tag{3.21}$$

Here, the first term is the startup transient component generated by the initial value ($V_{1,0}$) of v_1, and the remaining two terms describe the startup transient components generated by the continuously-imposed steps from v_1. The full expression for $i_{11}(t)$ including these burst-mode startup transitions is given by the summation of (3.19) and (3.21). Appendix C provides the complete derivations of the expressions for i_1 and i_2. The rectifier's switching time during the beginning of the startup transitions also affect the transient tank currents, and a method to include their effect is also discussed in Appendix C.

As described in Chapter 4, a prototype 200 W, 500 kHz ICN converter designed to operate over an input voltage range of 25 V to 40 V and output voltage range of 250 V to 400 V is built and tested. The values of the components used in the prototype are: $N = 5.33$, $L_{\mathrm{X1}} = 1.38$ µH, $C_{\mathrm{X1}} = 141$ nF, $L_{\mathrm{X2}} = 0.84$ µH, $C_{\mathrm{X2}} = 68$ nF, $L_{\mathrm{r}} = 18.8$ µH and $C_{\mathrm{r}} = 4.66$ nF. The experimental waveforms of this prototype converter are used to verify the results predicted by the S2 analysis. Figure 3.8 shows the experimental and modeled waveforms of the tank current for the ICN converter operating in steady state at 40 V input and 250 V output. As can be seen in Fig. 3.8, there is an excellent match between the modeled and experimental waveforms. The experimental and modeled burst-mode startup waveforms of the tank current of the ICN converter operating at 40 V input voltage and 400 V output voltage are shown in Fig. 3.9. Again, it is apparent that excellent agreement exists between the modeled and experimental waveforms.

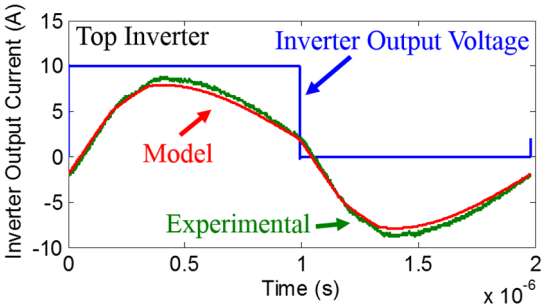

(a)

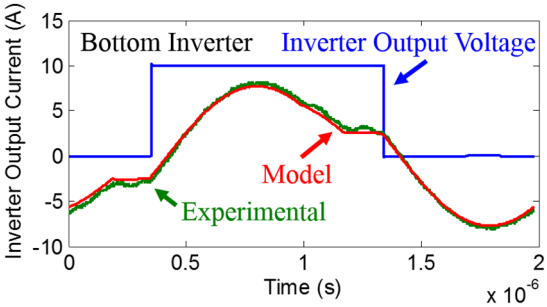

(b)

Figure 3.8: Comparison of modeled and experimental steady-state tank current waveforms of the ICN converter operating at 40 V input and 250 V output.

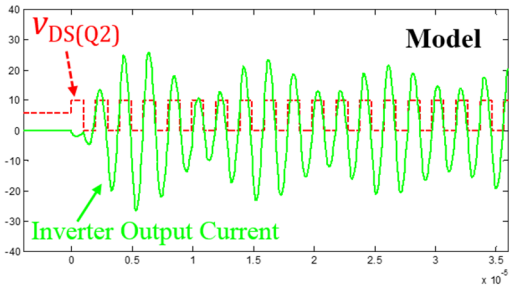

(a)

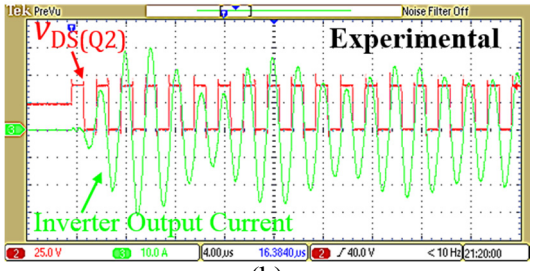

(b)

Figure 3.9: Comparison of modeled and experimental burst-mode startup waveforms of the top inverter of the ICN converter operating at 40 V input and 400 V output.

3.5 Applicability of S2 Analysis

In S2 analysis, the inverter outputs and rectifier inputs are modeled as rectangular-wave voltage sources. It is worth mentioning that the switching node voltages of class-D inverters and rectifiers can be modeled as rectangular-wave sources, while the switching node voltages of class-E inverters or rectifiers cannot be modeled as rectangular-wave sources. Figure 3.10 shows an example class-E inverter, where the input inductor is large and can be treated as a constant current source. The voltage at the switching node is zero during the on mode, while in the off mode it is not specified and is determined by the rest of the circuit. Figure 3.11 shows the equivalent circuits of the class-E inverter during the on and off modes, with the voltage source short-circuited and the current source open-circuited. As shown in Fig. 3.11, the two equivalent circuits of the resonant network during the two modes are different. This implies that the resonant network changes during the converter's operation, and hence S2 is not directly applicable. Hence one assumption of using S2 analysis is that the resonant converter can only contain class-D inverters and rectifiers. These class-D inverters can be either voltage source or current source driven and the class-D

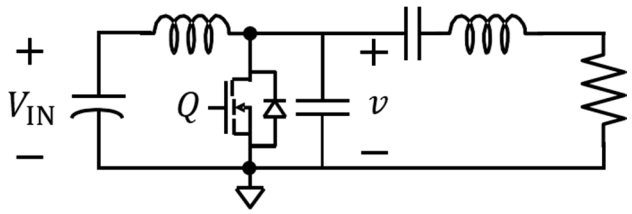

Figure 3.10: An example class-E inverter.

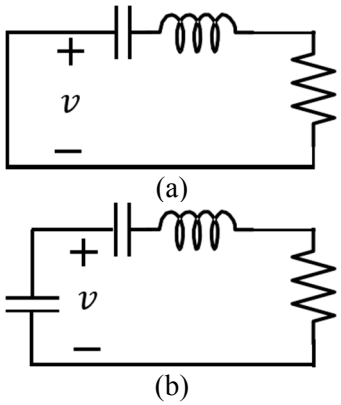

Figure 3.11: Equivalent circuit of the class-E inverter of Fig. 3.10 with: (a) the transistor turned on; (b) the transistor turned off.

rectifiers can be either voltage or current loaded.

A second assumption is that the effect of dead time on the resonant network waveforms can be neglected. During the dead time, the output capacitances of the transistors and diodes become parts of the resonant network. The exact currents and voltages of the resonant network during the dead time can be obtained using either state plane analysis or state space analysis. However, it is complicated to find closed-form expressions for the exact resonant network waveforms during the dead time and numerical solutions are usually used instead. S2 analysis is applicable to resonant converters in which the dead times are short, and hence do not substantially impact the converter waveforms. Under these limitations, the S2 analysis can provide closed-form expressions for the resonant network waveforms and can be easily used to analyze resonant converters containing high-order resonant networks, multiple inverters and/or rectifiers.

Chapter 4

Step-Up ICN Converters

4.1 Design Methodology

In this chapter, we consider the design of the ICN resonant converter shown in Fig. 2.3 has been designed and built with specifications suitable for an interface between a solar photovoltaic (PV) module and a dc distribution system: an input voltage range of 25 V to 40 V, an output voltage range of 250 V to 400 V, and a maximum output power of 200 W. The converter's switching frequency is selected as 500 kHz.

The maximum output power of the ICN converter increases with output voltage (see Fig. 2.6); therefore, if maximum output power can be delivered at minimum output voltage then maximum output power can be delivered at all output voltages. Also given the variation in output power with input voltage (see Fig. 2.6), the need for burst mode control can be minimized if the converter is designed to deliver the same output power at its minimum and maximum input voltages. This requirement can be met at the minimum output voltage if the transformer turns ratio N and the reactance X of the impedance control network are selected using:

$$N = \frac{V_{\mathrm{OUT,min}}}{\sqrt{V_{\mathrm{IN,min}}^2 + V_{\mathrm{IN,max}}^2}}, \tag{4.1}$$

$$X = \frac{4V_{\mathrm{IN,min}}\sqrt{V_{\mathrm{OUT,min}}^2 - N^2V_{\mathrm{IN,min}}^2}}{\pi^2 NP_{\mathrm{OUT,max}}}, \tag{4.2}$$

where $V_{\mathrm{IN,min}}$ is the minimum input voltage, $V_{\mathrm{IN,max}}$ is the maximum input voltage, $V_{\mathrm{OUT,min}}$ is the minimum output voltage and $P_{\mathrm{OUT,max}}$ is the maximum output power. For the given design specifications, N is 5.3 and X is 2.03 Ω.

Once the required differential reactance X is known, the next step is to come up with the design equations for the individual reactive component values. As can be seen from Fig. 2.3, there are three series resonant tanks in the impedance control network. These tanks serve two purposes: i) provide the necessary differential reactances; and ii) filter higher-order harmonics. More specifically, the L_{X1}-C_{X1} tank provides

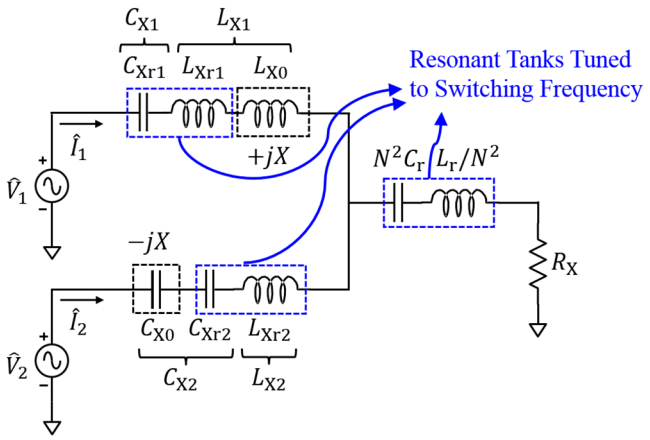

Figure 4.1: Primary side reactive elements broken up into their conceptual constituents: differential reactances L_{X0} and C_{X0}, and series resonant tank elements (L_{Xr1}, C_{Xr1}, L_{Xr2} and C_{Xr2}). In the top branch, L_{X0} and L_{Xr1} collectively form L_{X1} and C_{Xr1} is simply C_{X1} of Fig. 2.3. In the bottom branch, C_{X0} and C_{Xr2} collectively form C_{X2} and L_{Xr2} is simply L_{X2} of Fig. 2.3. The $\hat{V}_1$ and $\hat{V}_2$ are the fundamental components of the output voltages of the inverters, and the $\hat{I}_1$ and $\hat{I}_2$ are the fundamental components of the output currents of the inverters.

the $+jX$ reactance and some filtering of the harmonics, the L_{X2}-C_{X2} tank provides the $-jX$ reactance and also some filtering, and the L_r-C_r tank only provides filtering of higher-order harmonics. Hence, part of the L_{X1}-C_{X1} tank needs to be tuned to the switching frequency to filter out higher-order harmonics, and the remaining part needs to provide the $+jX$ reactance. Likewise, one part of the L_{X2}-C_{X2} tank needs to be tuned to the switching frequency for filtering, and the remaining part needs to provide the $-jX$ reactance. Hence, to determine the values of these reactive components it is simplest to split L_{X1} into two series inductors L_{X0} and L_{Xr1}; and split C_{X2} into two series capacitors C_{X0} and C_{Xr2}. With this division, L_{X0} of the top tank can provide the $+jX$ reactance, and L_{Xr1} together with C_{X1} form the filter. For the bottom tank, C_{X0} can provide the $-jX$ reactance, and L_{X2}-C_{Xr2} form the filter. Figure 4.1 shows the model of the ICN converter under fundamental frequency approximation. The division of the two tanks (L_{X1}-C_{X1} and L_{X2}-C_{X2}) is also shown in Fig. 4.1. Also C_{X1} is relabelled as C_{Xr1} and L_{X2} is relabelled as L_{Xr2}. The voltage source $\hat{V}_1$ models the fundamental component of the output voltage of the top inverter, the voltage source $\hat{V}_2$ models the fundamental component of the output voltage of the bottom inverter, and the phase difference between $\hat{V}_1$ and $\hat{V}_2$ has the specific value determined by (2.2) to make the susceptance seen by the inverters zero. The

remaining parts of the ICN converter of Fig. 2.3 are the transformer, the L_r-C_r tank, the rectifier and the load. Under fundamental frequency approximation a rectifier can be modeled as a resistor (see [4], [12] for equivalent modeling of rectifiers). In Fig. 4.1 the resistor that models the rectifier and the L_r-C_r tank have been reflected to the primary side of the transformer.

The values of the differential reactive elements (L_{X0} and C_{X0}) are determined using:

$$L_{X0} = \frac{X}{\omega_s}, \tag{4.3}$$

$$C_{X0} = \frac{1}{X\omega_s}, \tag{4.4}$$

where ω_s is the angular switching frequency of the converter. The values of the resonant tank elements are determined using:

$$L_{Xr1} = \frac{Z_{0X1}}{\omega_s},\ L_{Xr2} = \frac{Z_{0X2}}{\omega_s},\ L_r = N^2\frac{Z_{0r}}{\omega_s}, \tag{4.5}$$

$$C_{Xr1} = \frac{1}{Z_{0X1}\omega_s},\ C_{Xr2} = \frac{1}{Z_{0X2}\omega_s},\ C_r = \frac{1}{N^2 Z_{0r}\omega_s}, \tag{4.6}$$

where Z_{0X1}, Z_{0X2} and Z_{0r} are the desired characteristic impedances of the tanks ($\equiv \sqrt{L_{Xr1}/C_{Xr1}}$, $\sqrt{L_{Xr2}/C_{Xr2}}$, and $\sqrt{L_r/C_r}/N^2$, respectively). Their values are determined from $Z_{0X1} = Q_{0X1}R_X$, $Z_{0X2} = Q_{0X2}R_X$ and $Z_{0r} = Q_{0r}R_X$, where Q_{0X1}, Q_{0X2}, and Q_{0r} are the desired loaded quality factors of the resonant tanks, and R_X ($=2V_{OUT}^2/\pi^2N^2P_{OUT}$) is the equivalent resistance of the rectifier referred to the primary side of the transformer.

4.2 Selection of Resonant Tank Quality Factors (Q)

The selection of the quality factors of the resonant tanks is a major design consideration in the ICN converter as they impact the level of filtering of the higher order harmonics and value of the resonant inductance. If the resonant tanks are designed to have relatively high quality factors (high-Q) then the tank currents will be almost perfectly sinusoidal but the values of the resonant inductances will be high (with commensurately large inductor size and series resistance). On the other hand, low quality factor (low-Q) designs will require small resonant inductance values leading to reduced losses in the inductor. However,

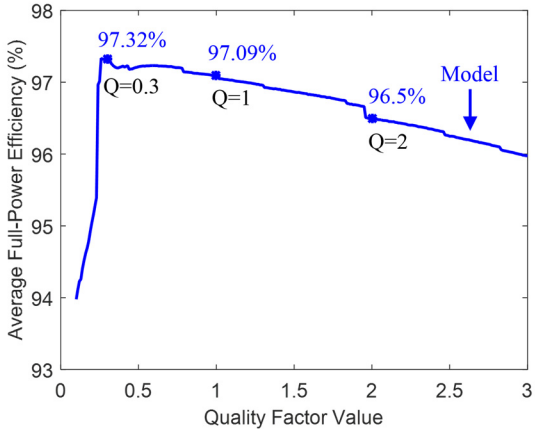

Figure 4.2: Theoretically predicted average full-power efficiencies of ICN converters versus the Q value of their resonant tanks. In all converters, the switching frequency is 505 kHz.

in the low-Q designs the tank currents will not be perfectly sinusoidal. The relatively non-sinusoidal tank currents in the low-Q design could increase turn-off switching losses. To explore the tradeoffs between the above-mentioned conduction and switching losses, a series of ICN converters have been designed with different quality factors for the resonant tanks. The tank Q for the different designs is varied from 0.1 to 3 in step size of 0.01. For each design, the full-power efficiencies are calculated (using an accurate loss model introduced in Appendix D) and averaged over four corner operating points: 25 V input voltage and 250 V output voltage; 25 V input voltage and 400 V output voltage; 40 V input voltage and 250 V output voltage; and 40 V input voltage and 400 V output voltage. The resultant average full-power efficiencies for these ICN converters are plotted against their Q in Fig. 4.2. As can be seen from Fig. 4.2, the average efficiency reaches a peak value of 97.32% when Q is around 0.3. The average efficiency decreases slowly above this value of Q, and drops sharply below it. To verify these theoretical results, three ICN converters with resonant tank Q values of 0.3 (low-Q), 1 (medium-Q) and 2 (high-Q) are built and tested.

4.3 Designed Prototypes

For the low-Q ICN converter, the quality factors of the resonant tanks are approximately 0.3 (Q_{0X1} = 0.28, Q_{0X2} = 0.29, and Q_{0r} = 0.41) when R_X has its minimum value of 2.25 Ω (corresponding to the operating point V_{OUT} = 250 V and P_{OUT} = 200 W). For the given specifications, the values of the reactive components are: $L_{X1} = L_{X0} + L_{Xr1}$ = 0.645 µH + 0.2 µH = 0.845 µH, $C_{X1} = C_{Xr1}$ = 507 nF, $L_{X2} = L_{Xr2}$ = 0.211 µH, and C_{X2}

= $C_{Xr2} \parallel C_{X0}$ = 480 nF ‖ 157.1 nF = 118 nF, L_r = 8.34 μH and C_r = 10 nF. For the medium-Q ICN converter, the actual quality factors are: Q_{0X1} = 0.96, Q_{0X2} = 1.13, and Q_{0r} = 1. For the given specifications, the values of the tank elements are $L_{X1} = L_{X0} + L_{Xr1}$ = 0.645 μH + 0.685 μH = 1.33 μH, $C_{X1} = C_{Xr1}$ = 147 nF, $L_{X2} = L_{Xr2}$ = 0.81 μH, and $C_{X2} = C_{Xr2} \parallel C_{X0}$ = 125 nF ‖ 157.1 nF = 69.6 nF, L_r = 19.1 μH and C_r = 4.9 nF. For the high-Q ICN converter, the actual quality factors are: Q_{0X1} = 2, Q_{0X2} = 2, and Q_{0r} = 2. For the given specifications, the values of the tank elements are $L_{X1} = L_{X0} + L_{Xr1}$ = 0.645 μH + 1.44 μH = 2.085 μH, $C_{X1} = C_{Xr1}$ = 70.6 nF, $L_{X2} = L_{Xr2}$ = 1.44 μH, $C_{X2} = C_{Xr2} \parallel C_{X0}$ = 70.6 nF ‖ 157.1 nF = 48.71 nF, L_r = 38.5 μH, and C_r = 2.4 nF. The above component values are determined under fundamental frequency approximation, which neglects the effect of higher order harmonics. In practice, due to the presence of higher order harmonics, with these component values the currents through the two branches of the ICN converter are not balanced. To balance these currents the value of C_r is slightly altered from its designed value (see Table I). Considering that the actual component values in a practical design may vary from their desired values, the robustness of the ICN converter's performance to these variations is investigated and discussed in Appendix E.

The actual components used in the fabrication of the three prototype ICN resonant converters are listed in Table I. The core material chosen for the magnetic elements (inductors and transformer) for all three converters is N49 from EPCOS since it has low losses around 500 kHz. Litz wire is used to wind the inductors and the transformer. The primary side resonant capacitors are 250-V NP0 low-ESR capacitors, while 1-kV mica low-ESR capacitors are used for the secondary side resonant capacitors. For the half-bridge inverters, EPC 100-V/25-A enhancement-mode gallium nitride (GaN) transistors (EPC2001) are used. These are driven by half-bridge drivers designed for enhancement-mode GaN transistors (LM5113). For the rectifier stage 600-V/2-A silicon carbide (SiC) Schottky diodes (C3D02060E) are used. The converter is controlled using a Microchip dsPIC33FJ64GS610, a 16-bit digital signal controller with high-speed PWM outputs. Figure 4.3 shows the top and bottom views of the prototype low-Q ICN resonant converter.

TABLE I

Actual Components Used in the Prototype ICN Resonant Converters

Component	Low-Q Design	Medium-Q Design	High-Q Design
Q_1, Q_2, Q_3, Q_4	EPC2001, 100-V/25-A eGaN FETs		
D_1, D_2	C3D02060E, 600-V/2-A Schottky Diodes		
L_{X1}	0.89 µH Core: RM10 EPCOS N49 Winding: 4 turns of 4000-strands 48 AWG litz wire	1.38 µH Core: RM12 EPCOS N49 Winding: 4 turns of 6000-strands 48 AWG litz wire	2.147 µH Core: RM12 EPCOS N49 Winding: 5 turns of 6000-strands 48 AWG litz wire
C_{X1}	507 nF 250-V NP0	141 nF 250-V NP0	68 nF 250-V NP0
L_{X2}	0.25 µH Core: RM10 EPCOS N49 Winding: 2 turns of 4000-strands 48 AWG litz wire	0.84 µH Core: RM10 EPCOS N49 Winding: 3 turns of 4000-strands 48 AWG litz wire	1.508 µH Core: RM10 EPCOS N49 Winding: 4 turns of 4000-strands 48 AWG litz wire
C_{X2}	115 nF 250-V NP0	68 nF 250-V NP0	47 nF 250-V NP0
L_r	8.11 µH Core: RM12 EPCOS N49 Winding: 10 turns of 450-strands 46 AWG litz wire	18.8 µH Core: RM10 EPCOS N49 Winding: 19 turns of 450-strands 46 AWG litz wire	39 µH Core: RM10 EPCOS N49 Winding: 27 turns of 450-strands 46 AWG litz wire
C_r	8.72 nF 1000-V Mica	4.66 nF 1000-V Mica	2.47 nF 1000-V Mica
T_X	1 : 5.33, RM10 EPCOS N49 core, Primary winding: 3 turns of 2000-strands 48 AWG Litz wire, Secondary winding: 16 turns of 450-strands 46 AWG Litz wire, Leakage inductance referred to the secondary side: 2.16 µH		
C_{IN}	2.2 mF × 2, 63-V electrolytic capacitors		
C_{OUT}	47 µF × 1, 450-V electrolytic capacitors		

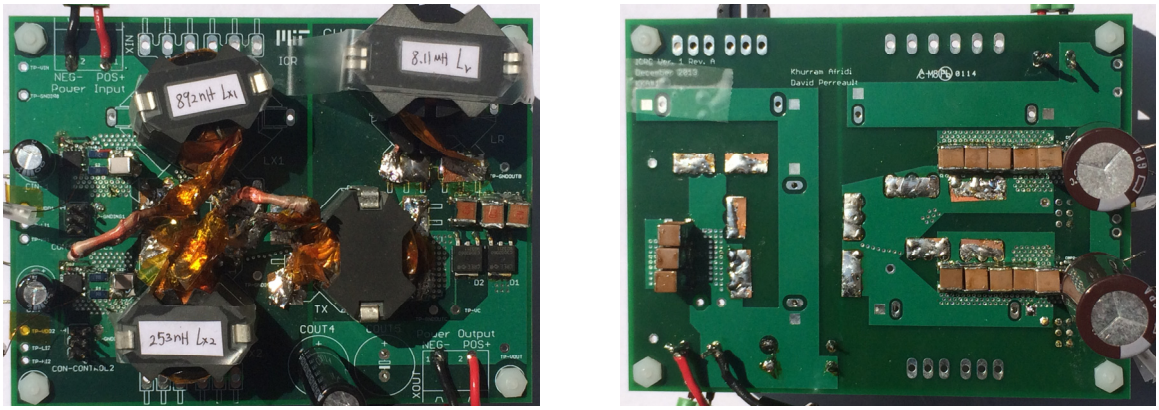

(a) (b)

Figure 4.3: Photograph of the (a) top and (b) bottom of the prototype low-Q ICN resonant converter.

Since the ICN converters are operated in relatively low frequency burst mode to regulate output voltage and power, substantial input and output capacitance is needed to limit output voltage ripple and input and output capacitor ESR losses. Also if the RMS currents through the capacitors are larger than their rated value, the lives of the capacitors will be reduced. Based on theoretical analysis and simulations, the minimum output capacitance that meets a worst case $\pm 1\%$ voltage regulation and also does not exceed the capacitor RMS current limit is 47 μF, and the minimum input capacitance that does not exceed RMS current limit is 4.4 mF. Hence, a 47 μF electrolytic capacitor and two 2.2 mF electrolytic capacitors are used as output and input capacitors, respectively.

4.4 ZVS Operation

As described in Chapter 2, the switching frequency of the ICN converter needs to be slightly higher than the resonant frequency of the resonant tank to ensure ZVS operation of the inverter transistors across the converter's full operating range. To determine the appropriate switching frequency, the designed ICN converters have been simulated at different switching frequencies across the entire operating range, and the simulated waveforms used to determine whether ZVS operation is achieved at all these operating points. For instance, consider a high-to-low transition of the inverter output voltage, as shown in Fig. 4.4(a). During this transition, the inverter output current needs to be positive enough to fully discharge the output capacitance of the bottom transistor (C_{ds2} in Fig. 4.4(a)), while simultaneously charging the output capacitance of the top transistor (C_{ds1} in Fig. 4.4(a)). The maximum charge that the inverter output current can move from the output capacitances can be obtained by integrating the inverter output current from the transistor turnoff instant to the current zero-crossing. This is referred to as the maximum movable charge in Fig. 4.4(b). To achieve ZVS operation, the maximum movable charge needs to be greater than or equal to the charge that needs to be moved. Similar analysis applies to the low-to-high transitions of the inverter output voltage.

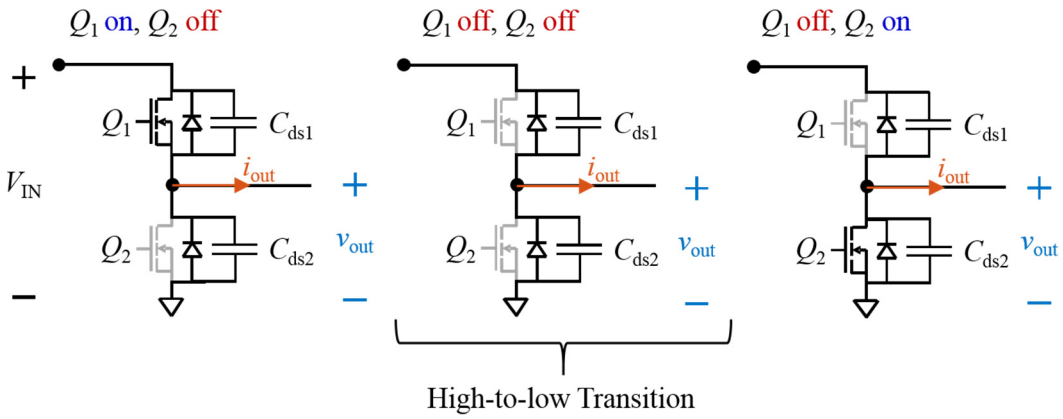

(a)

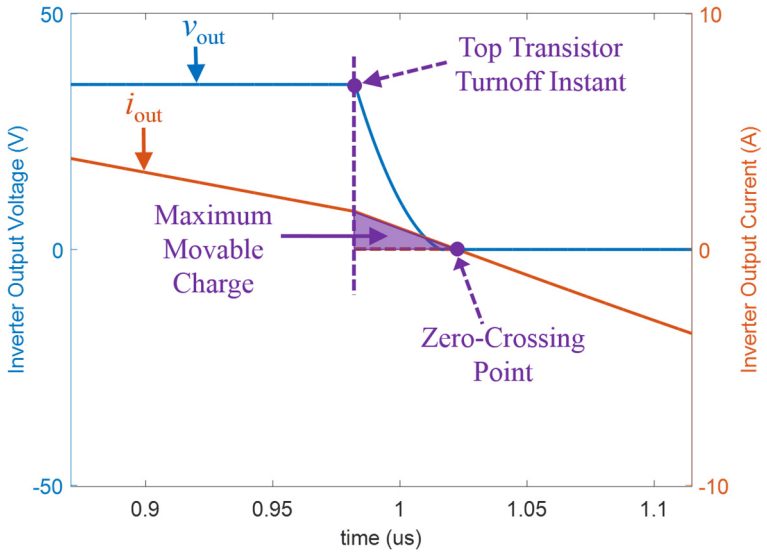

(b)

Figure 4.4: High-to-low transition of a half bridge inverter: (a) switch states during the transition, and (b) inverter output voltage and output current waveforms and definition of maximum movable charge.

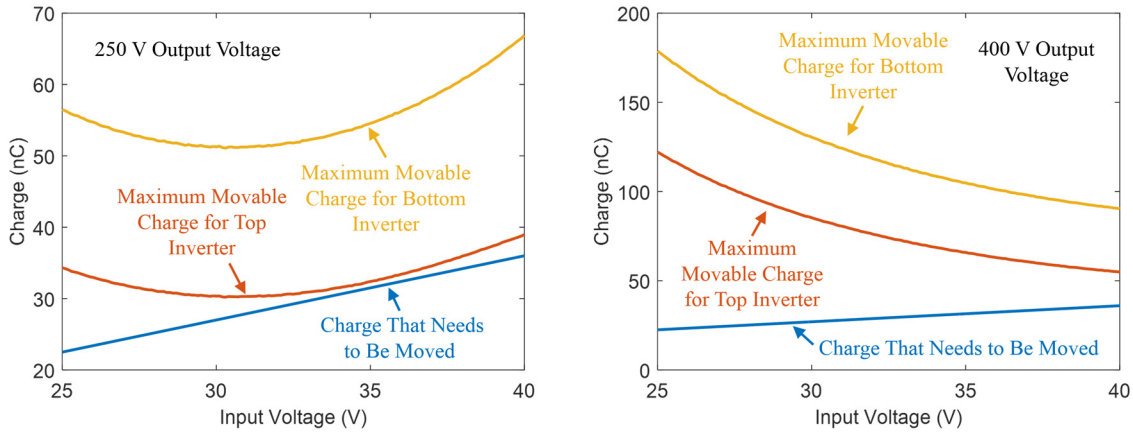

(a) (b)

Figure 4.5: Maximum movable charge and charge that needs to be moved for the top and bottom inverters (as shown in Fig. 4) of the medium-Q ICN converter as a function of input voltage for two extreme output voltage cases: (a) output voltage equal to 250 V and (b) output voltage equal to 400 V. These plots are obtained from the simulated waveforms of the medium-Q ICN converter switching at 509 kHz.

The maximum movable charge and the charge that needs to be moved for the medium-Q ICN converter are plotted as a function of input voltage in Fig. 4.5 for the two extreme values of output voltage: 250 V and 400 V. As can be seen from Fig. 4.5, the maximum movable charge for both the top and bottom inverters (as shown in Fig. 2.3) is always larger than the charge that needs to be moved when the switching frequency is increased to 509 kHz. Hence, the medium-Q ICN converter can achieve ZVS operation across its entire operating range at a switching frequency of 509 kHz. Using similar analysis, the switching frequency needed to guarantee ZVS operation for the high-Q design is found to be roughly the same as that for the medium-Q design. However, the required switching frequency for the low-Q design is slightly higher. This is because the current waveforms of the medium-Q and high-Q designs are both fairly sinusoidal, while the currents of the low-Q design have substantial harmonic content.

4.5 Experimental Results

The low-Q, medium-Q and high-Q 200-W prototype ICN converters have been built and tested. All three converters are operated at a switching frequency of 505 kHz, slightly higher than the designed switching frequency, to make the two inverters sufficiently inductively-loaded to achieve zero voltage switching

(ZVS). Although this switching frequency is slighlty lower than the theoratically predicited value in Section 4.4, it is sufficient to achieve ZVS operation across the entire operating range of the converters. This is partly because the theoretical model assumes a fixed value for the output capacitance of the inverter transistors, while the actual transistors' output capacitance has a strong nonlinear dependence on voltage.

4.5.1 ZVS, Near ZCS and Burst Mode Operation

Figure 4.6 shows the measured waveforms of the three ICN converters when operated at full power (200 W) at their minimum input voltage (V_{IN} = 25 V) and minimum output voltage (V_{OUT} = 250 V). To deliver full power at these voltages, burst mode (on/off) control is not needed, as the converters produce 200 W of output power when they are running continuously. Clearly the switches of both the top and the bottom inverters of the three converters achieve ZVS and near ZCS. ZVS is achieved as the inverter output current is sufficiently negative during the low to high inverter output voltage transitions and sufficiently positive during the high to low inverter output voltage transitions. Near ZCS is achieved as the currents are fairly sinusoidal (due to the presence of the series resonant tanks with reasonable loaded quality factors), with phase that only slightly lags the voltage waveforms.

A useful measure of near ZCS operation is the ratio of the switch current at turn-off to its peak current. For the low-Q converter, the turn-off current of the top inverter is about 1.5 A, which is about 17% of the peak current value; the turn-off current of the bottom inverter is about 2.7 A, which is about 19% of the peak value of the current. The medium-Q and high-Q converters have similar performance in terms of near ZCS operation, even though they use quality factors that are at least three times larger than the low-Q version. The ratios of the turn-off switch current to the peak current for the medium-Q converter are 16% for the top inverter and 25% for the bottom one, and the ratios of the turn-off switch current to the peak current for the high-Q converter are 18% for the top inverter and 30% for the bottom one.

The waveforms of Fig. 4.6 can also be used to compare the theoretically-required phase shift between the two inverters and that needed in practice to achieve ZVS and near ZCS operation. In Fig. 4.6 the phase shift between the two inverters is about 634 ns for the three converters, which is 32% of the switching period (1.982 μs) and corresponds to an angle of 115.16°. This is within 0.5% of the theoretically predicted

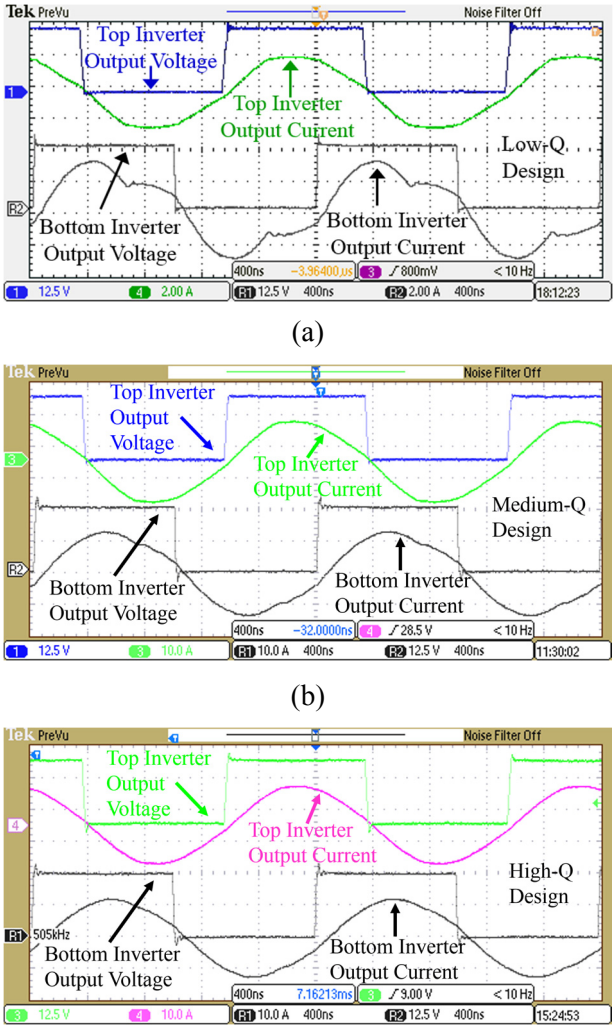

Figure 4.6: Measured waveforms for the (a) low-Q, (b) medium-Q and (c) high-Q ICN converters operating at full power (200 W) at 25 V input voltage and 250 V output voltage. Waveforms shown are the output voltage and output current of both (top and bottom) half-bridge inverters of the (a) low-Q ICN converter, (b) medium-Q ICN converter and (c) high-Q ICN converter.

phase shift value (115.58°) calculated using (2.2).

When the output voltage and - to a lesser extent - the input voltage of the converter increase above their minimum values, burst mode control is needed to limit output power to 200 W (see Fig. 2.6). Burst mode control is also needed at all input/output voltage combinations when the output power is reduced below 200 W. Figure 4.7 shows the operation of the medium-Q converter under burst mode control with an input voltage of 25 V, an output voltage of 400 V and the output power regulated to 200 W. Fixed-frequency PWM burst-mode on/off modulation was used, with a bursting frequency of 1.68 kHz. This value is

selected as it provides a good balance between the additional losses in the input capacitors due to the on/off modulation frequency ripple current and the additional losses in the converter due to its repeated startup and shutdown. Figure 4.7 also shows zoomed-in views of the bottom inverter's output voltage and output current waveforms during converter startup and shutdown.

As stated in section 4.1, large output capacitance is needed to achieve good output voltage regulation when the converter is operating in burst mode. To verify the output voltage regulation of the prototype ICN converters, the output votlage ripple is measured when the converters are operating with 40 V input voltage, 400 V output voltage and 200 W output power. The output voltage of the low-Q converter is shown in Fig. 4.8 at this operating point. As can be seen from Fig. 4.8, the output voltage is quite flat and its ripple has a peak-to-peak value of 5.44 V, which is equivalent to $\pm 0.68\%$ and within the designed range.

To validate that the ICN resonant converter achieves ZVS and near ZCS operation across its entire design range, the operation of the low-Q, medium-Q and the high-Q ICN converters has been tested across their specified input voltage, output voltage and output power ranges. Figure 4.9 shows the pertinent waveforms of the medium-Q converter at four extreme operating points as input voltage is varied from 25 V to 40 V and output voltage is varied from 250 V to 400 V, while keeping output power constant at 200 W. Again it is easy to see that both (top and bottom) inverters of the ICN converter achieve ZVS turn-on and near ZCS turn-off at all four operating points. Figure 4.10 shows the zoomed in view of the switch voltages and currents during the switching transitions when operating with 25 V input and 400 V output. The ZVS turn-on of all the transistors can be observed in Fig. 4.10. It has been confirmed that the medium-Q ICN converter achieves ZVS and near ZCS operation across its entire operating range. Similarly the ZVS and near ZCS operation of the low-Q and high-Q converter has been confirmed across the entire operating range. In Fig. 4.9, it can also be seen that the phase lag of the inverter output current relative to the inverter output voltage is different for different operating points. This is because the needed phase lag in the inverter output current depends on the charge that has to be removed from the output capacitances of the inverter switches (determined by the converter input voltage) and the available current (determined by the maximum output power).

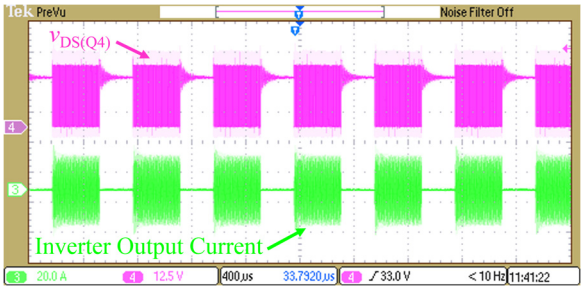

(a)

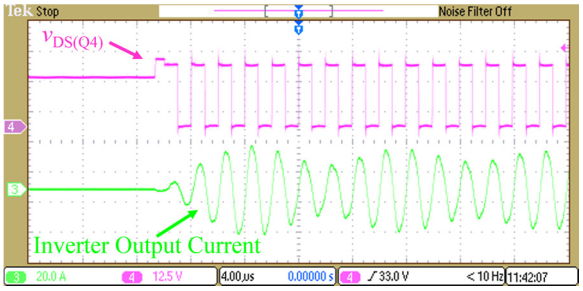

(b)

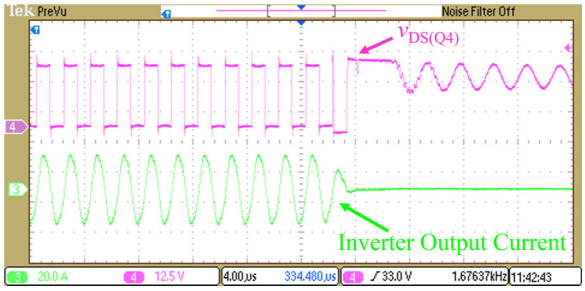

(c)

Figure 4.7: Burst mode operation of the medium-Q ICN resonant converter delivering full power (200 W) at 25 V input voltage and 400 V output voltage. Waveforms shown are the output voltage and output current of the bottom half-bridge inverter: (a) long timescale showing multiple startup and shutdown sequences, (b) zoomed timescale to show the startup dynamics, and (c) zoomed timescale to show the shutdown dynamics.

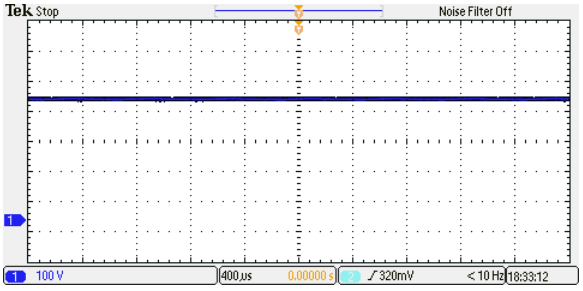

(a)

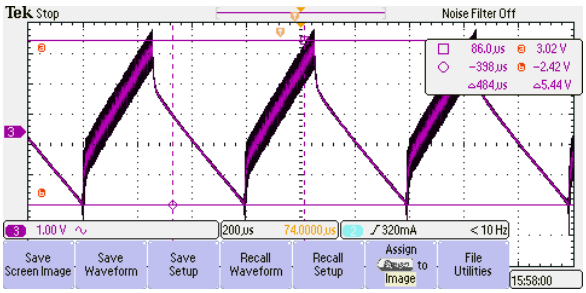

(b)

Figure 4.8: Output voltage for the low-Q ICN converter operating with 40 V input voltage, 400 V output voltage, and 200 W output power measured in (a) 100 V/division and (b) 1 V/division.

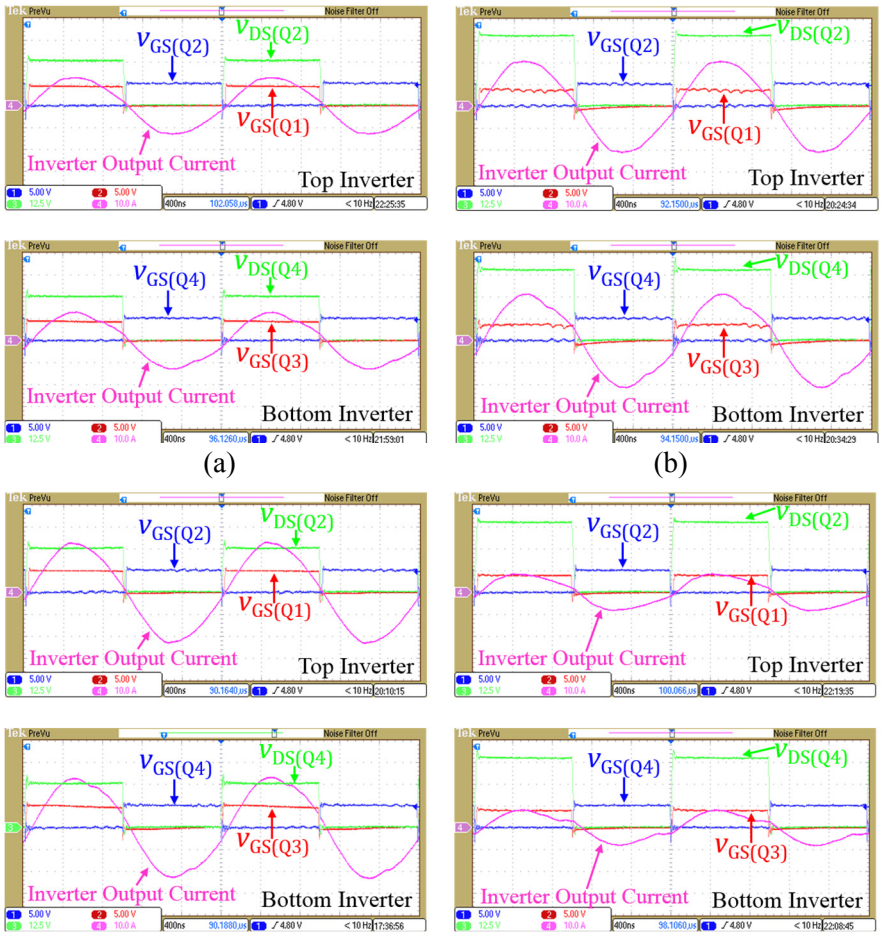

Figure 4.9: Measured waveforms confirming ZVS and near ZCS operation of the medium-Q ICN resonant converter at four extreme operating points in terms of input voltage (V_{IN}) and output voltage (V_{OUT}): (a) V_{IN} = 25 V, V_{OUT} = 250 V, (b) V_{IN} = 40 V, V_{OUT} = 400 V, (c) V_{IN} = 25 V, V_{OUT} = 400 V, (d) V_{IN} = 40 V, V_{OUT} = 250 V.

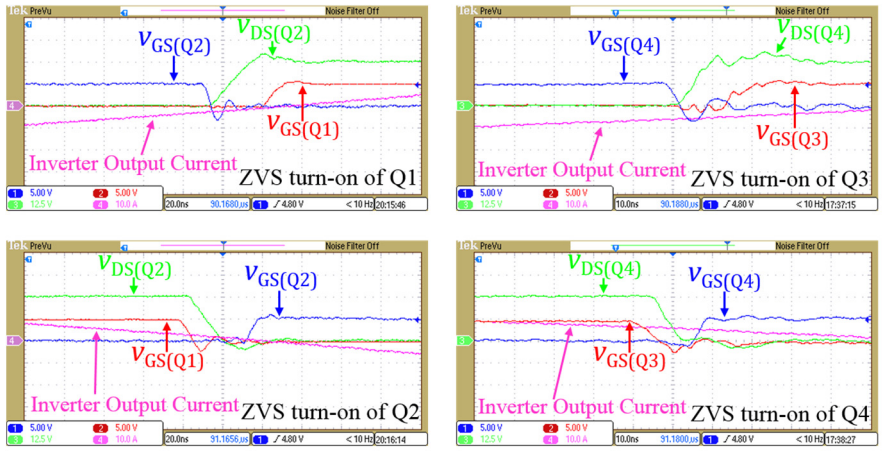

Figure 4.10: Measured waveforms confirming ZVS operation of the medium-Q ICN resonant converter with V_{IN} = 25 V, V_{OUT} = 400 V: (a) ZVS turn-on of the transistors in the top inverter and (b) ZVS turn-on of the transistors in the bottom inverter.

4.5.2 Efficiency Comparison

The efficiency of the three prototype ICN converters has been measured across their entire operating range. The measured efficiency of the three converters is plotted in Fig. 4.11 across variations in input voltage, output voltage and output power. Note that all the efficiency plots are quite flat.

Figure 4.11(a) and (b) plot the efficiency of the ICN converters as their input voltage is varied from 25 V to 40 V, while the output voltage and output power are held constant. In both cases the output power is 200 W, while the output voltage is 250 V in Fig. 4.11(a) and 400 V in Fig. 4.11(b). When the output voltage is 250 V, the peak efficiency of the low-Q ICN converter is 97.1% and its efficiency does not fall below 96.4% as the input voltage is varied across its entire range. The efficiency increases monotonically with increasing input voltage, as primary-side conduction losses are reduced with decreasing input current. The medium-Q converter has a slightly higher peak efficiency of 97.2% and the high-Q converter has a slightly lower peak efficiency of 96.8% than the low-Q converter, but the shapes of the efficiency plots are similar. The efficiency of the converters reduces at higher output voltages, as the converters have to be operated in burst mode to limit output power. However, at full output power (200 W) the efficiency of the low-Q converter never falls below 95%, which occurs at the lowest input voltage (25 V) and highest output voltage (400 V). This is also the operating point at which the difference in efficiency between the low-Q and the high-Q designs is the largest (2.1%). This is because at this operating point the converter has the highest input current resulting in large conduction losses in the inductors.

Figure 4.11(c) and (d) plot the efficiency of the three ICN converters as their output voltage is varied from 250 V to 400 V, while the input voltage and output power are held constant. Again in both cases output power is 200 W, while input voltage is 25 V in Fig. 4.11(c) and 40 V in Fig. 4.11(d). When the input voltage is 40 V, the efficiency of the low-Q converter stays above 96.2% and achieves a peak value of 97.1% when the output voltage is at its minimum (250 V). Again the worst case efficiency of the low-Q converter is 95%, at minimum input voltage (25 V) and maximum output voltage (400 V). The efficiency of the high-Q design is again lower than that of the low-Q and medium-Q designs.

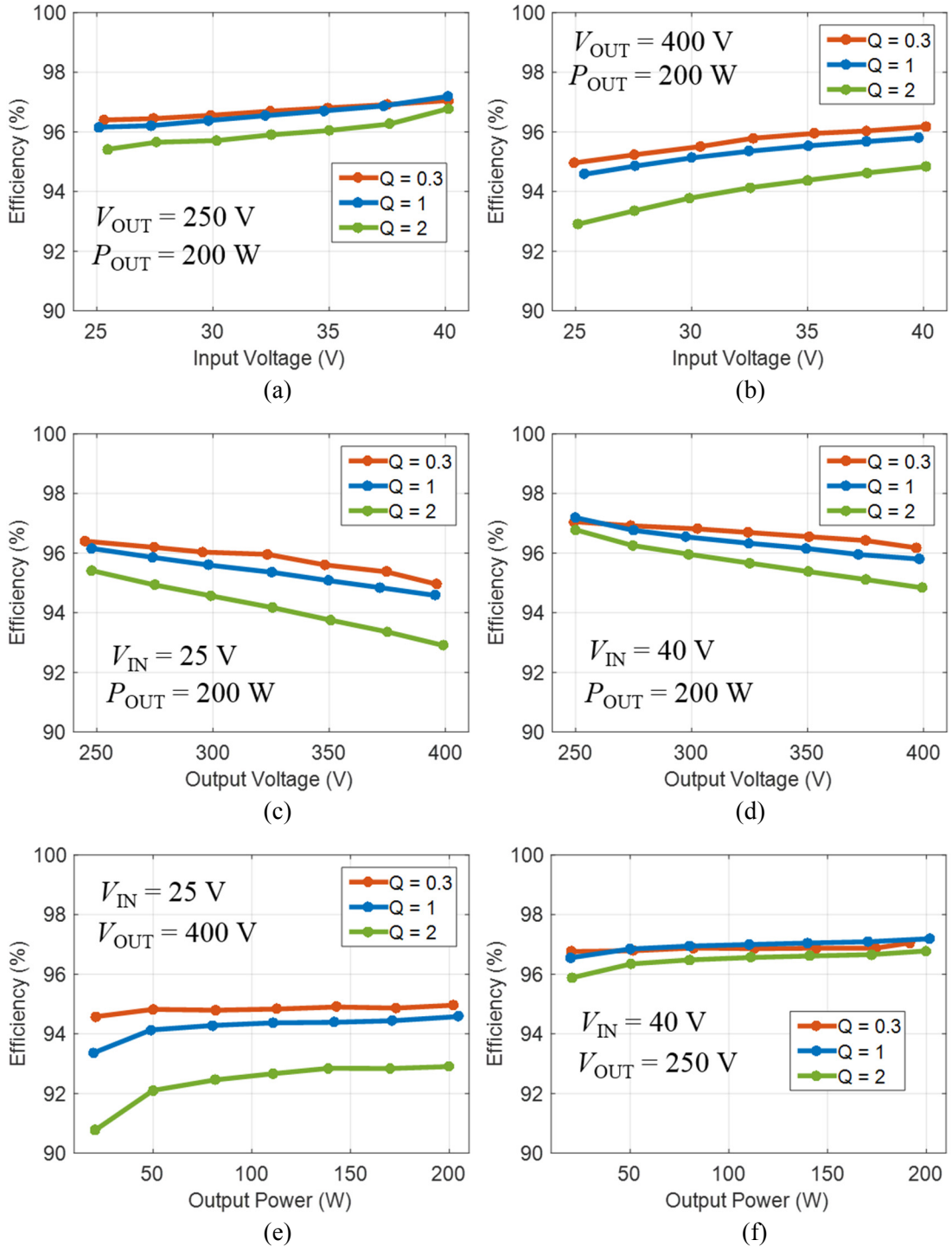

Figure 4.11: Measured efficiency of the low-Q, medium-Q and high-Q ICN resonant converters across variations in input voltage (V_{IN}), output voltage (V_{OUT}) and output power (P_{OUT}): (a) variation in input voltage with V_{OUT} = 250 V and P_{OUT} = 200 W, (b) variation in input voltage with V_{OUT} = 400 V and P_{OUT} = 200 W, (c) variation in output voltage with V_{IN} = 25 V and P_{OUT} = 200 W, (d) variation in output voltage with V_{IN} = 40 V and P_{OUT} = 200 W, (e) variation in output power with V_{IN} = 25 V and V_{OUT} = 400 V, and (f) variation in output power with V_{IN} = 40 V and V_{OUT} = 250 V.

The efficiency of the three ICN converters as the output power is varied is plotted in Fig. 4.11(e) and (f). In Fig. 4.11(e) the input voltage is held at 25 V and the output voltage is held at 400 V and in Fig. 4.11(f) the input voltage is held at 40 V and the output voltage is held at 250 V. In both cases burst mode control is used to vary the output power from 20 W to 200 W. The efficiency of the three converters as a function of output power is quite flat, varying by only 0.3% for the low-Q design over its entire 10:1 output power range when input voltage is 40 V and output voltage is 250 V. The low-Q converter has its lowest efficiency of 94.6% when input voltage is at its minimum (25 V), output voltage is at its maximum (400 V) and output power is at its minimum (20 W). When input voltage is 40 V and output voltage is 250 V the peak efficiency is 97.1% at an output power of 200 W and the efficiency is still above 96.8% at an output power of 20 W. Hence, burst mode control is a good method for regulating output power in an ICN resonant converter as it enables good light load efficiency. However, it does require larger input and output capacitors than might otherwise be used (depending upon the application). For the low-Q ICN converter, the efficiency at 10% of rated power is only 1.2% lower than its full load efficiency, but requires the addition of a 47-uF/450-V electrolytic cpacitor with volume of 0.28 in^3.

In summary, the low-Q ICN converter has higher efficiency than the higher Q designs across the full operating range, except for a narrow range around the 40 V input voltage and 250 V output voltage

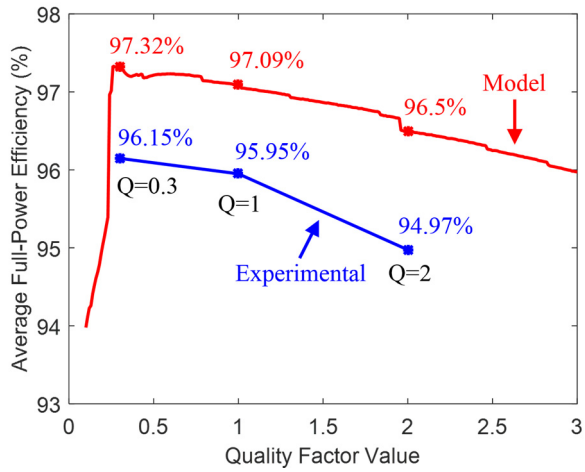

Figure 4.12: Experimental and theoretically predicted average full-power efficiencies of ICN converters versus their Q value. In all converters, the switching frequency is 505 kHz.

operating point, where the medium-Q design has the highest efficiency. Both the low-Q and medium-Q designs have higher efficiency than the high-Q converter across the full operating range. This is because the low-Q and medium-Q converters have significantly lower conduction losses due to their lower valued inductors, and they are still able to maintain ZVS and near ZCS operation across the full operating range. The average values of the full-power efficiencies at the four corner operating points are calculated for each prototype converter and plotted in Fig. 4.12. As can be seen from Fig. 4.12, there is a good match between the experimental and the theoretically predicted efficiencies.

The efficiency results presented above demonstrate that the ICN resonant converter is able to maintain very high efficiencies across a wide range of operating conditions in terms of input voltage, output voltage and output power. To better understand the tradeoffs between the low-Q and the high-Q designs, and explore opportunities for further improvements in efficiency of the ICN converter, a loss breakdown analysis of the three converters has been performed based on the analytical models of the individual loss mechanisms given in Appendix D. Figure 4.13 shows the estimated loss breakdown of the three ICN converters when operating at 32.5 V input voltage, 325 V output voltage and 200 W output power. At this operating point, the diode, magnetic, and transistor losses account for the majority of the power losses for all the three converters. For the low-Q design, the transistor losses are larger than the magnetic losses. For the medium-Q design, the magnetic losses are slightly larger than the transistor losses, while in the high-Q design the magnetic losses are much larger than the transistor losses. In all converters, there are also some losses in the resonant and bypass capacitors and the PCB traces. The gate drive losses are very small due to the use of low gate charge GaN transistors. Figure 4.14 compares the measured and the theoretically predicted total losses in the medium-Q ICN converter across its full input voltage range when operating at 250 V output voltage and 200 W output power. There is reasonably good agreement between the predicted and measured values.

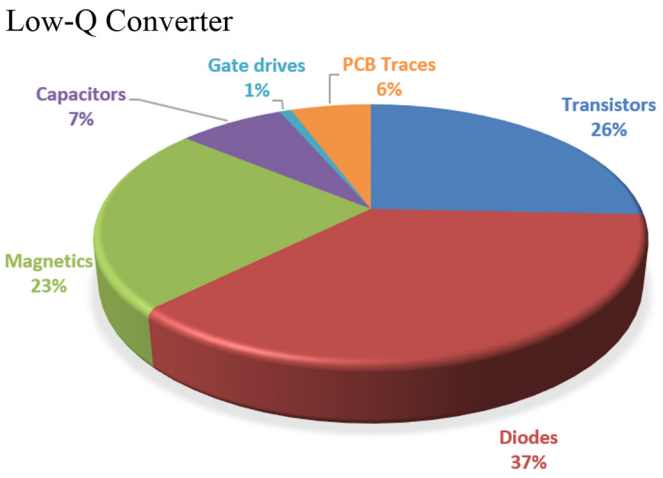

(a)

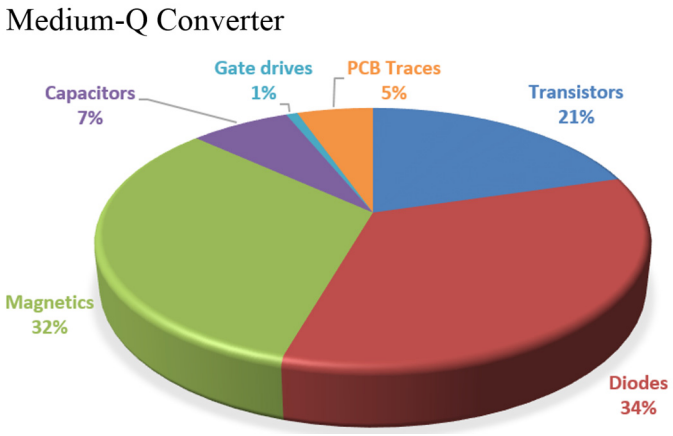

(b)

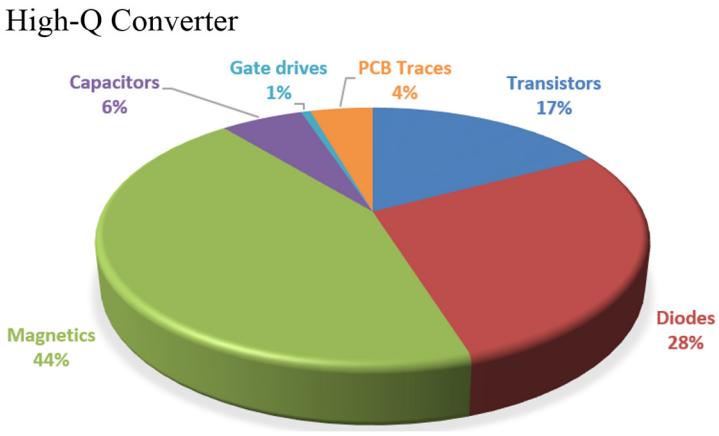

(c)

Figure 4.13: Loss breakdown of (a) low-Q, (b) medium-Q and (c) high-Q ICN converter based on theoretical models when the converters are operating at an input voltage of 32.5 V, output voltage of 325 V and output power of 200 W.

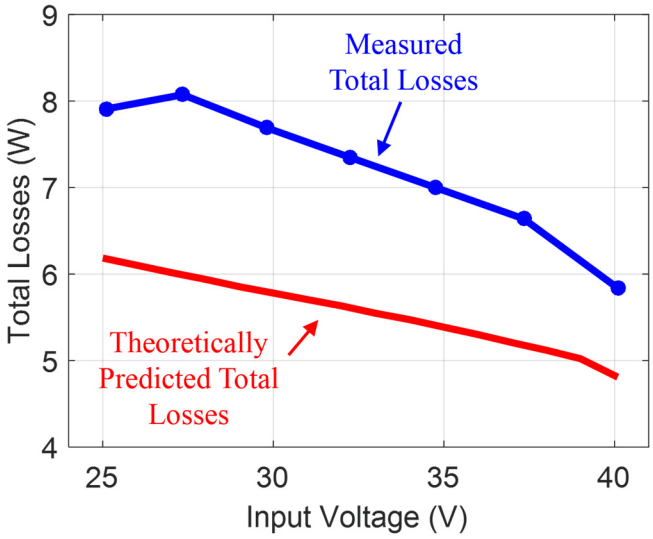

Figure 4.14: Comparison of measured and theoretically predicted total losses in the medium-Q ICN converter as a function of input voltage when the converter is operating at an output voltage of 250 V and output power of 200 W.

Chapter 5

Optimized Startup Control of ICN Converter

5.1 Need for Optimized Startup

As discussed in previous chapter, burst mode is utilized to control the output power of the ICN converter. An issue associated with burst mode operation is that it takes several switching cycles for the converter to achieve steady state and during this startup transition ZVS and near ZCS operation may be lost. This has a negative impact on converter efficiency, especially at light loads when the burst duty ratio is low and the converter spends a large fraction of its total on-time in the startup transition. Therefore, a startup control is needed to minimize the duration of the startup transient.

5.2 Methodology for Determining Optimized Startup

To determine the optimal startup control for the ICN converter, accurate time domain waveforms obtained using step-superposition (S2) analysis approach are used to find the startup sequence that minimizes the settling time of the startup transient. In this approach, the voltages imposed on the impedance control network by the inverter and rectifier switches are modeled by three rectangular-wave voltage sources. The inverter output currents (i_1 and i_2) can be determined via superposition of the individual responses to the three voltage sources, e.g., $i_1(t) = i_{11}(t) + i_{12}(t) + i_{13}(t)$, where $i_{1x}(t)$ is the component of i_1 generated by v_x (where x is 1, 2 or 3). These individual current responses can be determined by modeling each rectangular voltage waveform as a series of positive and negative steps, and by adding their step responses as discussed in Chapter 3. The summations of the step responses can be simplified using Euler's identity, trigonometric identities and geometric series analysis to yield closed-form expressions for the tank currents. Using this technique, $i_{11}(t)$ is given by $i_{11}(t) = i_{11s}(t) + i_{11t}(t)$, where $i_{11s}(t)$ and $i_{11t}(t)$ are the steady state and transient components, respectively, and given by (5.1) and (5.2).

$$i_{11s}(t) = \begin{cases} I_{111}\sin\left(\omega_1 t'_{\mathrm{K}} - \frac{\omega_1 T_{\mathrm{S}}}{4}\right)/\left[2\cos\left(\frac{\omega_1 T_{\mathrm{S}}}{4}\right)\right] + I_{112}\sin\left(\omega_2 t'_{\mathrm{K}} - \frac{\omega_2 T_{\mathrm{S}}}{4}\right)/\left[2\cos\left(\frac{\omega_2 T_{\mathrm{S}}}{4}\right)\right], & 0 \le t'_{\mathrm{K}} < T_s/2 \\ I_{111}\sin\left(\frac{3\omega_1 T_{\mathrm{S}}}{4} - \omega_1 t'_{\mathrm{K}}\right)/\left[2\cos\left(\frac{\omega_1 T_{\mathrm{S}}}{4}\right)\right] + I_{112}\sin\left(\frac{3\omega_2 T_{\mathrm{S}}}{4} - \omega_2 t'_{\mathrm{K}}\right)/\left[2\cos\left(\frac{\omega_2 T_{\mathrm{S}}}{4}\right)\right], & T_s/2 \le t'_{\mathrm{K}} < T_s \end{cases} \quad (5.1)$$

$$i_{11t}(t) = -I_{111}e^{-(K-1)\alpha_1 T_s}\sin\left(-\omega_1 t'_K + \frac{3\omega_1 T_s}{4} - N\omega_1 T_s\right)\Big/\left[2\cos\left(\frac{\omega_1 T_s}{4}\right)\right]$$
$$- I_{112}e^{-(K-1)\alpha_2 T_s}\sin\left(-\omega_2 t'_K + \frac{3\omega_2 T_s}{4} - N\omega_2 T_s\right)\Big/\left[2\cos\left(\frac{dT_s}{4}\right)\right]. \quad (5.2)$$

Here, time t is taken to be zero at the beginning of each burst cycle, T_s is the switching period of the converter, K is the number of switching cycles that have passed since the converter turned on in the current burst cycle and given by $K = \text{floor}(t/T_s)$, t'_K is the time elapsed within the current switching cycle, given by $t'_K = t - KT_s$, I_{111}, I_{112}, α_1, α_2, ω_1 and ω_2 are parameters that depend on input voltage, reactive component values, transformer turns ratio and converter losses. Their expressions are provided in Appendix C, along with complete expressions for all the tank currents. This model has been verified against simulated and experimental results, and some of this verification is provided in the next subsection.

5.3 Optimized Startup Control

The medium-Q ICN resonant converter as described in Chapter 4, is targeted for developing and demonstrating an optimized startup control approach. This ICN converter is operated in burst mode, which involves periodic startup and shutdown of the converter at a frequency much lower than its switching frequency. The measured burst mode startup waveforms of the top inverter of the ICN converter are shown and compared with their model-based counterparts in Fig. 5.1 for two operating points: 25 V input voltage and 400 V output voltage; and 40 V input voltage and 400 V output voltage. As can be seen in Fig. 5.1, there is an excellent match between the model and experimental waveforms. From Fig. 5.1, it can also be seen that both the phase and amplitude of the top inverter output current have oscillations, which result in the loss of ZVS and near ZCS during the startup transients. Similar oscillations also exist in the bottom inverter output current. The S2-analysis-based accurate time-domain model can be used to determine the optimal startup sequence. When operating with 40 V input voltage and 400 V output voltage, the model predicts that by modifying the duty ratio of the bottom inverter in the third switching cycle we can minimize the startup transients for both inverters. The duty ratio of the third switching cycle which minimizes the oscillations in the envelope of the inverter output currents, and hence the startup transients, is 10 %, as can

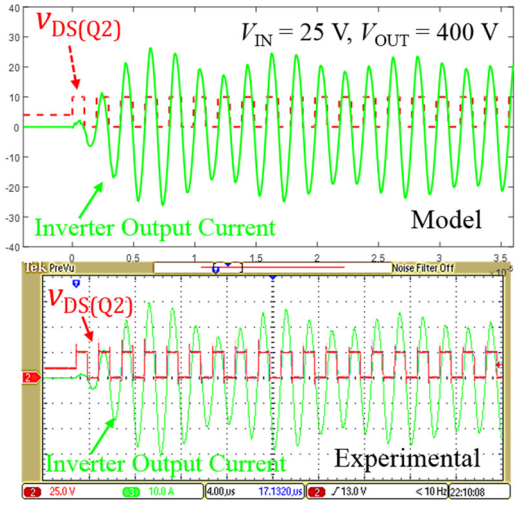

(a)

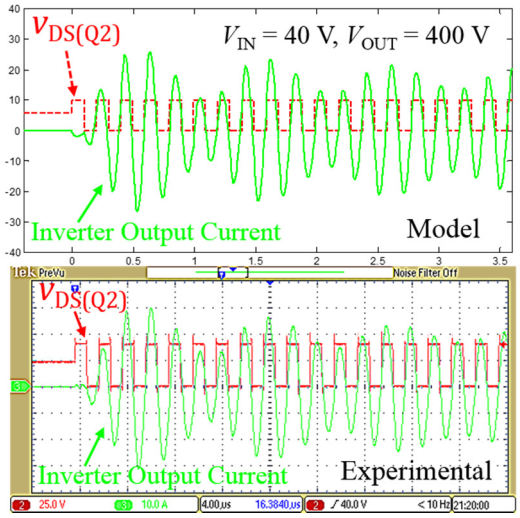

(b)

Figure 5.1: Comparison of model and experimental burst-mode startup waveforms of the top inverter of the ICN converter operating at two operating points without startup control.

be seen from Fig. 5.2. Applying this optimal duty ratio to the ICN converter confirms this prediction. The measured startup waveforms of the ICN converter with the duty ratio for the bottom inverter in the third switching cycle set at 10% are shown in Fig. 5.3. The current envelope oscillations for both inverters are considerably reduced. As compared to no startup control, the settling time with optimized startup control is reduced by 88%; the duration of the startup transient is reduced from 68.7 µs to 8.4 µs. Furthermore, the

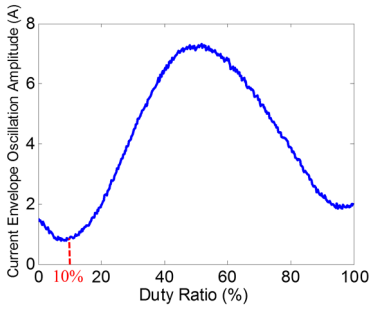

Figure 5.2: Inverter current envelope oscillation amplitude as a function of the duty ratio of the third switching cycle of the bottom inverter.

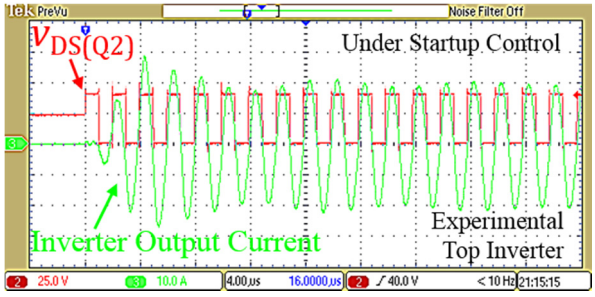

(a)

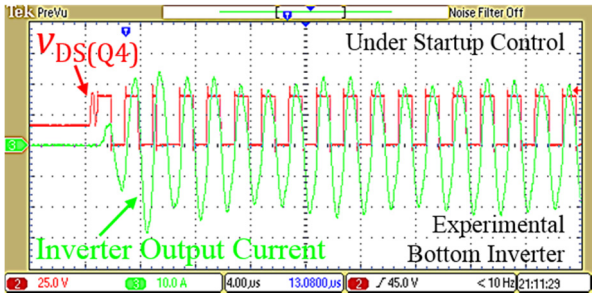

(b)

Figure 5.3: Startup waveforms of the ICN converter operating under optimized startup control at 40 V input voltage and 400 V output voltage.

optimized startup control technique eliminates 75% of the non-ZVS events; reducing the non-ZVS events from 20 to 5 events per burst cycle.

5.4 Efficiency Improvement due to Optimized Startup Control

The efficiency improvement brought by the optimized startup control is shown in Fig. 5.4. The startup control reduces the total losses by 12% when operating at 40 V input voltage, 400 V output voltage and 20

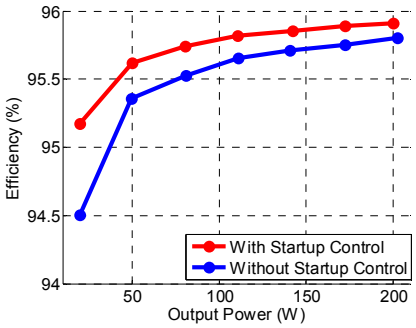

Figure 5.4: Measured efficiencies for ICN converter operating under startup control and without startup control across a power range of 20 W to 200 W at 40 V input and 400 V output.

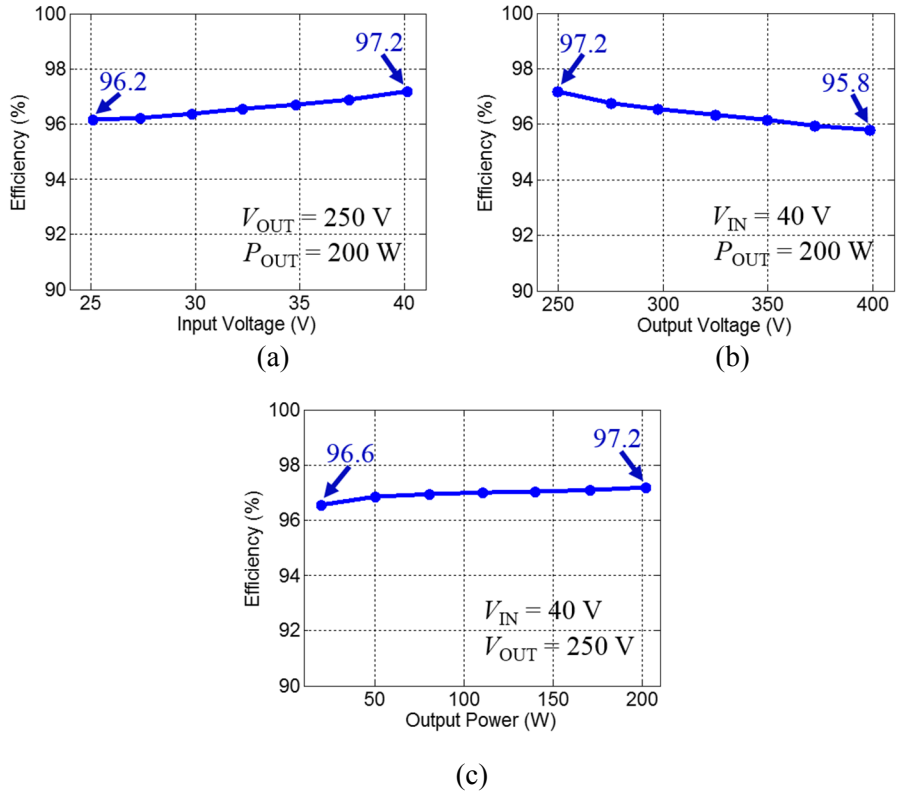

Figure 5.5: Measured efficiencies for the ICN converter across variations in (a) input voltage, (b) output voltage and (c) output power.

W output power (which corresponds to 10% of the full power), and results in 0.7% improvement in overall converter efficiency.

The efficiency of the prototyped converter with optimized startup control has been measured across its entire operating range. The measured efficiency is fairly flat across variations in input voltage, output

voltage and output power, as shown in Fig. 5.5. The prototype ICN converter achieves a peak efficiency of 97.2% and maintains greater than 96.2% full power efficiency at 250 V output voltage across the nearly 2:1 input voltage range, and maintains full power efficiency above 95.8% at 40 V input voltage across its full output voltage range. It also maintains efficiency above 96.6% over a 10:1 output power range at 40 V input voltage and 250 V output voltage, owing to the use of burst-mode control with startup optimization. The high efficiencies are a result of the converter maintaining ZVS and near-ZCS operation across its entire design range, both during startup and steady-state operation.

Chapter 6

ICN Converter with Enhanced Phase-Shift Control

6.1 Issues with Burst Mode Control

As discussed earlier, the use of burst-mode control introduces several challenges. Operating the converter with burst-mode control requires a large output capacitance, limiting the converter's power density. To further increase the power densities and efficiencies of ICN converters, there is a need for new control techniques to regulate their output voltage and power. In ICN converters that utilize synchronous rectifiers, such as the converter shown in Fig. 6.1, an effective alternative is enhanced phase-shift control, in which the inverter and rectifier phase-shifts are controlled to achieve both soft-switching and output voltage regulation.

6.2 Enhanced Phase-Shift Control

The ICN converter of Fig. 6.1 incorporates two half-bridge inverters, a full-bridge synchronous rectifier, and an impedance control network, and is well-suited for low output voltage and high output current step-down applications. Similar to the ICN converter shown in Chapter 4 and 5, this converter is operated at fixed switching frequency, and all inverter and rectifier legs are operated at a fixed duty ratio (~50%). At the switching frequency, the two ICN branches, which are directly connected to the inverters, are designed to have equal but opposite reactances (jX and $-jX$) to provide resistive loading of the inverters. However, there is a slight difference in this ICN converter implementation is that a small extra impedance jX_{L} is incorporated in each branch to make the impedance seen by each inverter inductive and enable ZVS operation of the inverters.

A phase-shift of Φ is introduced between the two rectifier legs, as shown in Fig. 6.2. Under fundamental frequency approximation the equivalent resistance of the rectifier with this phase-shift is given by $\frac{8V_{\mathrm{OUT}}^2}{\pi^2 P_{\mathrm{OUT}}}\sin^2\frac{\Phi}{2}$. Compared to the equivalent resistance of a full bridge rectifier where the two legs operate

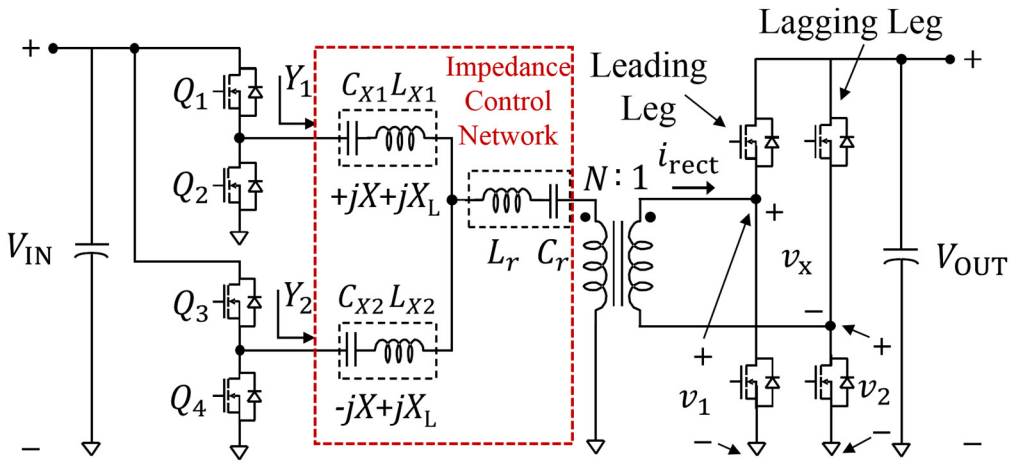

Figure 6.1: One implementation of the ICN resonant converter architecture, appropriate for voltage step-down.

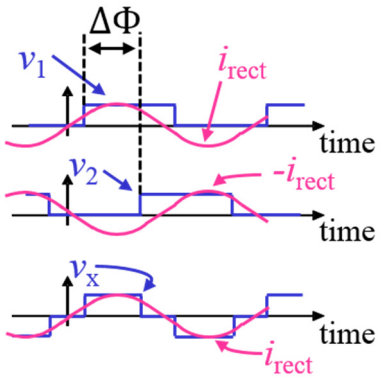

Figure 6.2: Phase-shift between the two legs of the synchronous full bridge rectifier as shown in Fig. 6.1.

180° out of phase, this equivalent resistance has an additional factor of $\sin^2\frac{\Phi}{2}$. The resultant output power of the ICN converter of Fig. 6.1 is then given by:

$$P_{OUT} = \frac{4V_{IN}\sqrt{4N^2V_{OUT}^2\sin^2\frac{\Phi}{2} - V_{IN}^2}}{\pi^2 X}\frac{\sqrt{1-r^2\frac{4N^2V_{OUT}^2\sin^2\frac{\Phi}{2}}{V_{IN}^2}}}{1-r^2}. \quad (6.1)$$

Here r is the ratio of X_L to X. To maintain ZVS and near-ZCS of the inverter transistors, the phase-shift between the inverters is given by:

$$2\Delta = 2\cos^{-1}\sqrt{\frac{\frac{V_{IN}^2}{4N^2V_{OUT}^2\sin^2\frac{\Phi}{2}} - r^2}{1-r^2}}. \quad (6.2)$$

The phases of the leading and lagging legs of the rectifier relative to the phase of the leading inverter are given by:

$$\Phi_{\text{lead}} = \Delta + \frac{\pi}{2} - \frac{\Phi}{2}, \tag{6.3}$$

$$\Phi_{\text{lag}} = \Delta + \frac{\pi}{2} + \frac{\Phi}{2}. \tag{6.4}$$

With this enhanced phase-shift control, burst-mode operation can be avoided over much of the output power range of the ICN converter. As a result, the output capacitance required in the converter is greatly reduced, as the capacitor no longer has to filter the low-frequency burst-mode ripple. The size of the input EMI filter is also reduced. Furthermore, switch stresses are lowered and efficiency is improved as hard-switching during startup transitions is avoided. Another advantage of the proposed enhanced phase-shift control is that the conduction losses in the components on the primary side of the transformer back-off faster with output power than in burst-mode control (where they back-off linearly). This variation in conduction losses with output power is shown in Fig. 6.3.

One potential disadvantage of this enhanced phase-shift control is that the transistors of the lagging leg of the rectifier can lose ZVS at some operating points. This could be a major drawback of this control approach in step-up ICN converters with high output voltages where loss of ZVS could result in high losses.

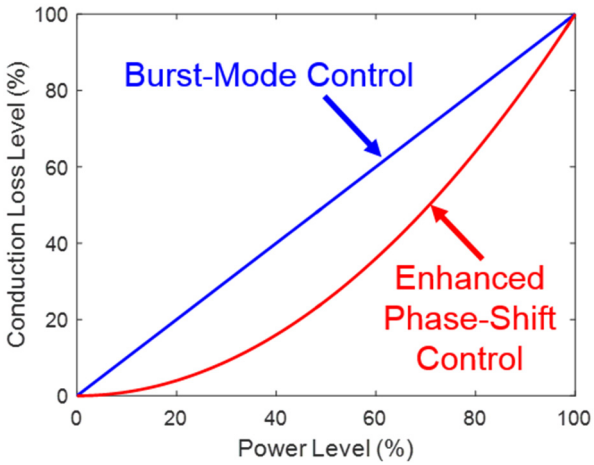

Figure 6.3: Variations in conduction losses in the components on the primary side of the transformer as a function of power delivered by the ICN converter with burst-mode control and with enhanced phase-shift control.

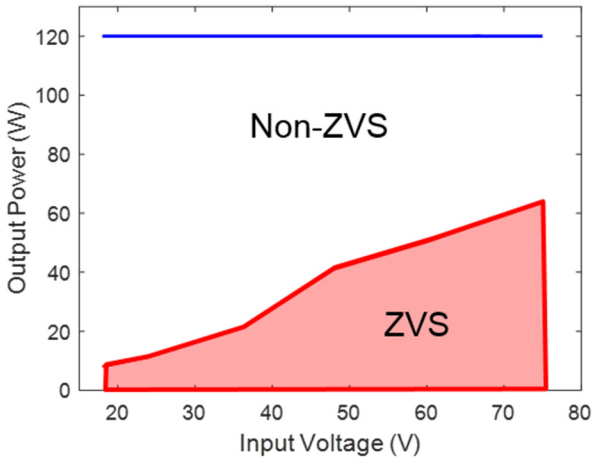

Figure 6.4: ZVS recovery region for the lagging leg of the ICN converter's full-bridge rectifier.

However, this is not a major concern in step-down converters, especially with low output voltages, as is the case in the ICN converter considered in this section. Furthermore, the transistors of the lagging leg of the rectifier recover ZVS at partial power levels, as indicated in Fig. 6.4.

6.3 Prototype Design

The design of the ICN converter involves three steps. In the first step the value of r (which is the ratio of X_{L} to X) is selected. If the value of r is too small, the inverter switches will not achieve ZVS. On the other hand, if the value of r is too large, inverter turn-off will occur at large currents and sizeable circulating currents and associated losses will exist. To ensure that the selected value of r is the minimum needed to achieve ZVS under the worst-case operating condition, an accurate model for the ICN converter currents is required. The step-superposition approach is used to develop this accurate model for the ICN converter, and used to determine the optimal value for r using a numerical approach. The second step of the design is to calculate the needed values for N, X, and X_{L}. These values can be determined from:

$$N = \frac{\sqrt{V_{\mathrm{IN,min}}^2 + V_{\mathrm{IN,max}}^2}}{2V_{\mathrm{OUT}}\sqrt{1+r^2}}, \tag{6.5}$$

$$X = \frac{4V_{\mathrm{IN,min}}\sqrt{4N^2V_{\mathrm{OUT}}^2 - V_{\mathrm{IN,min}}^2}}{\pi^2 P_{\mathrm{OUT,max}}} \frac{\sqrt{1-r^2\frac{4N^2V_{\mathrm{OUT}}^2}{V_{\mathrm{IN,min}}^2}}}{1-r^2}, \tag{6.6}$$

and $X_{\mathrm{L}} = rX$, where $V_{\mathrm{IN,min}}$ and $V_{\mathrm{IN,max}}$ are the minimum and maximum input voltages of the converter, and $P_{\mathrm{OUT,max}}$ is the maximum output power of the converter. The third and final step is to calculate the values of L_{X1}, C_{X1}, L_{X2}, C_{X2}, L_{r} and C_{r}. An effective approach is to divide these components into their functional parts. For example, L_{X1} provides two functions: (i) realizing $jX + jX_{\mathrm{L}}$ and (ii) forming a series resonant filter along with C_{X1} to attenuate higher-order current harmonics. The value of the part of L_{X1} that realizes $jX + jX_{\mathrm{L}}$ can be computed from $L_{\mathrm{X1,1}} = \frac{X+X_{\mathrm{L}}}{\omega_{\mathrm{s}}}$, where ω_{s} is the radial switching frequency of the converter, and the remaining part of L_{X1} can be computed from $L_{\mathrm{X1,2}} = \frac{Q_{0\mathrm{X1}}R_{\mathrm{X}}}{\omega_{\mathrm{s}}}$, where $Q_{0\mathrm{X1}}$ is the quality factor of the series resonant tank formed by $L_{\mathrm{X1,2}}$ and C_{X1}, and R_{X} is the effective series resistance of this tank (which depends on the effective impedance of the rectifier reflected through the transformer). The value of L_{X1} is then given by $L_{\mathrm{X1,1}} + L_{\mathrm{X1,2}}$. The values of the other components can be computed using a similar approach. An advantage of this approach is that it allows the efficiency of the ICN converter to be optimized by selecting appropriate resonant tank quality factors.

A 1-MHz step-down isolated ICN resonant converter (similar to the one shown in Fig. 6.1) has been designed, built and tested for the following specifications: an input voltage range of 18 V to 75 V, an output voltage of 12 V, and a maximum output power of 120 W. Figure 6.5 shows the top and bottom views of this prototype ICN converter. The circuit element values for this prototype are provided in Table II. The

TABLE II
Components Used in the Prototype Step-Down ICN Resonant Converter

Component	Value	Description
Inverter Transistors	-	EPC2001C 100-V/25-A eGaN FETs
Rectifier Transistors	-	EPC2023 30-V/60-A eGaN FETs
L_{X1}	1.4 μH	RM8 Ferroxcube 3F46
C_{X1}	44 nF	250-V NP0
L_{X2}	695 μH	RM8 Ferroxcube 3F46
C_{X2}	17.8 nF	250-V NP0
L_{r}	646 nH	Leakage of Transformer
C_{r}	26 nF	250-V NP0
Transformer	4 : 1	RM8 Ferroxcube 3F46 Primary 4 turns Secondary 1 turn

values are selected to be: $r = 0.1$, $N = 4$, $X = 5.2\ \Omega$, $X_{\mathrm{L}} = 0.52\ \Omega$, $L_{\mathrm{X1}} = 1.4\ \mu\mathrm{H}$, $C_{\mathrm{X1}} = 44\ \mathrm{nF}$, $L_{\mathrm{X2}} = 695\ \mathrm{nH}$, $C_{\mathrm{X2}} = 17.8\ \mathrm{nF}$, $L_{\mathrm{r}} = 646\ \mathrm{nH}$, and $C_{\mathrm{r}} = 26\ \mathrm{nF}$. For the inverters, EPC 100-V/36-A eGaN transistors (EPC2001C) are used. For the rectifier stage EPC 30-V/60-A eGaN transistors (EPC2023) are used.

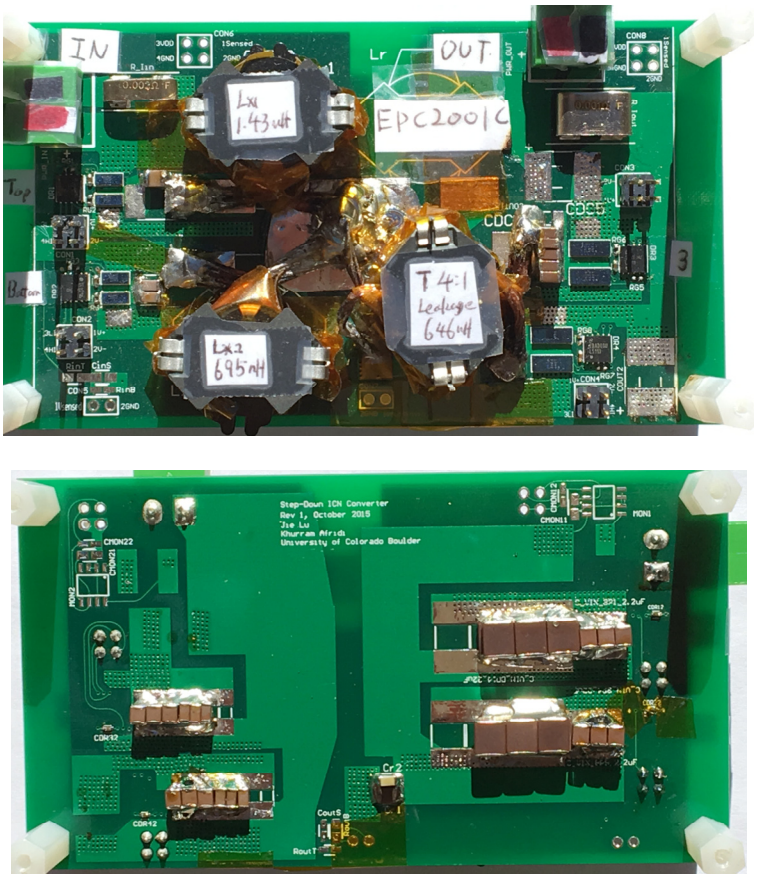

Figure 6.5: Photograph of the top and bottom of the prototype ICN resonant converter.

6.4 Experimental Results

The ICN converter is first operated under enhanced phase-shift control. Figure 6.6 shows the measured waveforms for all the transistors of the ICN converter operating at 120 W output power and 18 V input voltage. As can be seen from Fig. 6.6, all the inverter and rectifier transistors achieve ZVS and near ZCS operation. Figure 6.7 shows the measured waveforms of the ICN converter operating at 120 W output power and 75 V input voltage, and again all the inverter transistors operate with ZVS and near ZCS. However, for the rectifier, the leading leg operates with ZVS, while the lagging leg operates with ZCS. At this input

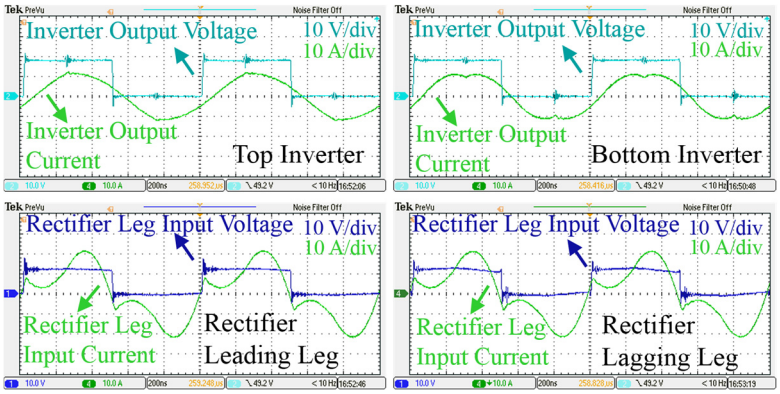

Figure 6.6: Measured waveforms for the ICN resonant converter operating at 18 V input voltage and 120 W output power.

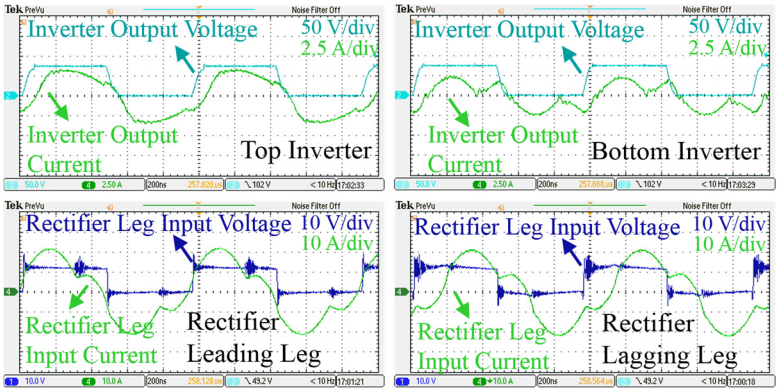

Figure 6.7: Measured waveforms for the ICN resonant converter operating at 75 V input voltage and 120 W output power.

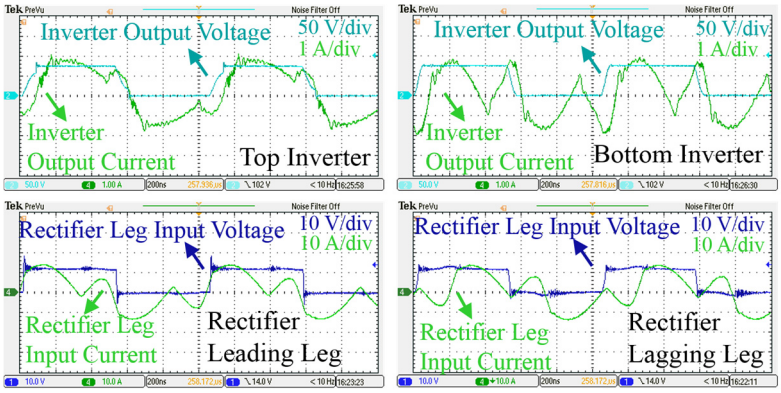

Figure 6.8: Measured waveforms for the ICN resonant converter operating at 75 V input voltage and 60 W output power.

voltage, the lagging leg of the rectifier recovers ZVS when the output power is reduced below 60 W, as can be seen from Fig. 6.8. The converter has also been operated under burst-mode control, and the measured waveforms for the converter operating at 60 W output power and 18 V input voltage are shown in Fig. 6.9.

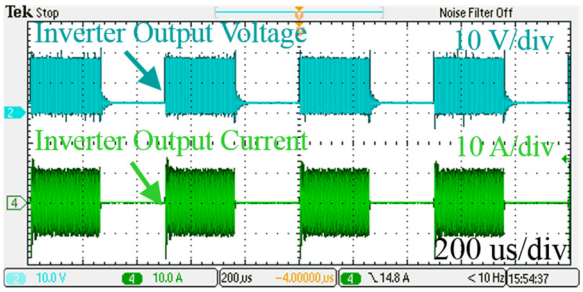

(a)

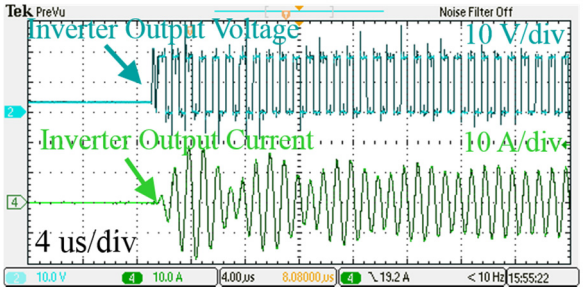

(b)

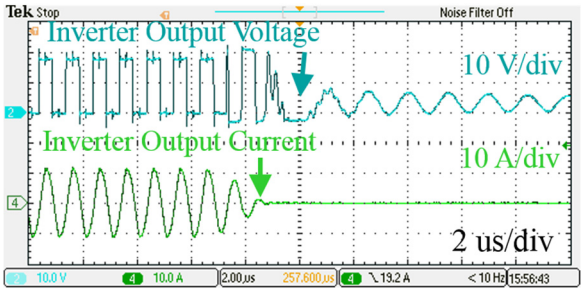

(c)

Figure 6.9: Burst mode operation of the ICN resonant converter delivering 60 W power at 18 V input voltage. Waveforms shown are the output voltage and output current of the top half-bridge inverter: (a) long timescale showing multiple startup and shutdown sequences, (b) zoomed timescale to show the startup dynamics, and (c) zoomed timescale to show the shutdown dynamics.

The efficiency of the prototyped converter has been measured across its entire operating range under enhanced phase-shift control and compared with its efficiency under burst-mode control, as shown in Fig. 6.10. With the enhanced phase-shift control, the ICN converter has higher efficiencies across its full input voltage range and most of its output power range. The ICN converter under enhanced phase-shift control achieves a peak efficiency of 95.7%. Relative to burst-mode control, the maximum full-power efficiency is improved by up to 1.5%, and the efficiency at 40% of full load is improved by up to 3%. This corresponds to a 30% reduction in losses. In addition, with enhanced phase-shift control the ICN converter maintains

full-power efficiency above 91.7% across its 4:1 input voltage range. Note that the efficiency of the ICN converter with inverter phase-shift and burst-mode control is not shown for 75 V input (Fig. 6.10(c) and (d)); this is because the hard-switching of the inverter transistors during the repeated startup transients imposes extra voltage stresses on the devices, preventing the converter from operating safely. Hence higher-voltage-rating devices are needed if the converter is operated under burst-mode control. On the other hand, under enhanced phase-shift control, the ICN converter is able to operate across its entire operating range with relatively low voltage devices.

A major difference between the ICN converter when operated under enhanced phase-shift control versus under burst-mode control is in the size of the output capacitance. To meet a ±3% output voltage ripple requirement, the output capacitance required under burst-mode control is 868 µF, while under enhanced phase-shift control it is only 8.68 µF, i.e., a two orders of magnitude reduction.

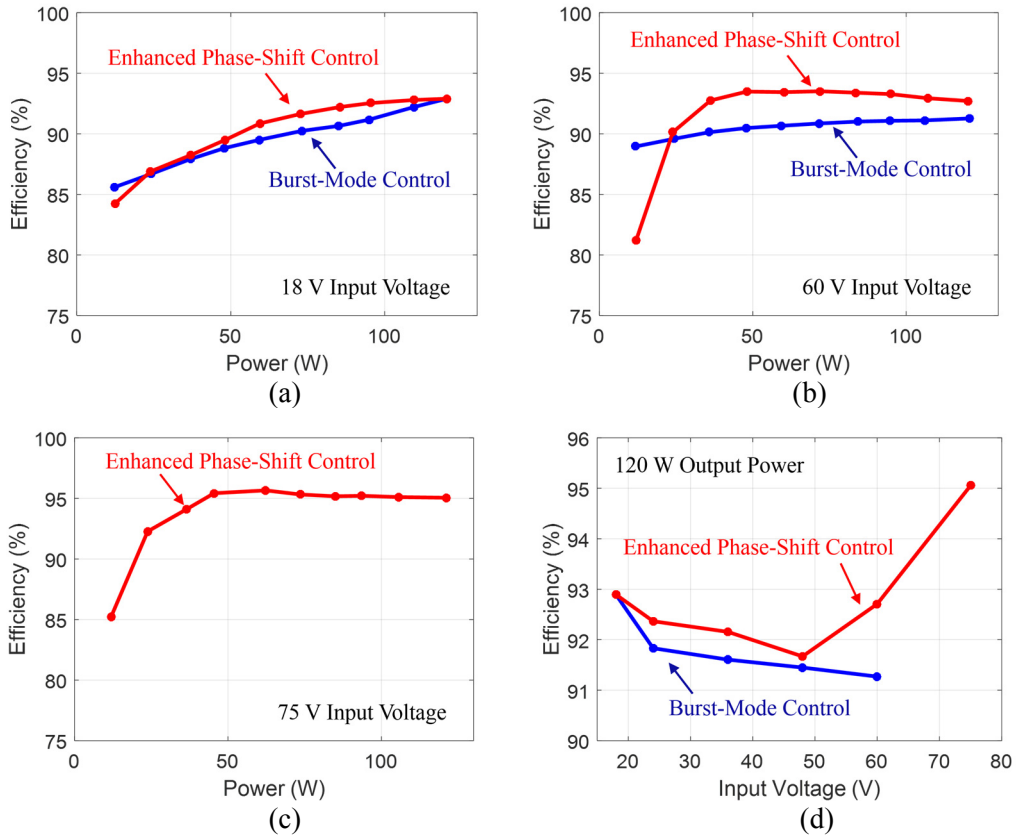

Figure 6.10: Measured efficiency of the ICN converter across variations in: (a) output power with an input voltage of 18 V; (b) output power with an input voltage of 60 V; (c) output power with an input voltage of 75 V; and (d) input voltage with an output power of 120 W.

Chapter 7

Closed-Loop Control of ICN Converter

7.1 Closed-Loop Control Architecture

All the ICN converters presented thus far are operated under open-loop control. This chapter introduces a closed-loop control architecture for the ICN converter that combines feed-forward and feedback control. To improve the closed-loop performance of the ICN converter across wide operating conditions, the controller also incorporates state feedback.

Figure 7.1 shows the simplified block diagram for the proposed control architecture of the ICN converter. The objective of the controller is to regulate the output voltage of the ICN converter when large variations exist in input voltage and output power. As shown in Fig. 7.1, the output voltage of the converter is sensed and compared with a reference voltage, and the error is processed by a linear compensator. The output of this compensator, defined as a new variable, power ratio, and denoted by p_{R}, serves as a control input to a lookup table. The power ratio p_{R} has a direct correlation with the output power delivered by the ICN converter, which can be understood as follows. Referring back to the formula for the output power of an enhanced phase-shift controlled ICN converter presented in Chapter 6, the output voltage and power can be regulated by controlling the phase-shift between the two rectifier legs (Φ, Fig. 6.2). The power ratio is a function of the rectifier phase-shift, and is given by:

$$p_{\mathrm{R}} = \sin^2 \frac{\Phi}{2}. \tag{7.1}$$

The output power of the ICN converter can be expressed in terms of the power ratio as:

$$P_{\mathrm{OUT}} = \frac{4V_{\mathrm{IN}}\sqrt{4N^2V_{\mathrm{OUT}}^2 p_{\mathrm{R}} - V_{\mathrm{IN}}^2}}{\pi^2 X} \frac{\sqrt{1-r^2\frac{4N^2V_{\mathrm{OUT}}^2 p_{\mathrm{R}}}{V_{\mathrm{IN}}^2}}}{1-r^2}. \tag{7.2}$$

It can be seen from (7.2) that apart from the power ratio, the output power depends on the output voltage and the input voltage of the converter. These are incorporated into the control architecture in the following manner: the output voltage reference, $V_{\mathrm{OUT,ref}}$, is used as a second control input of the lookup

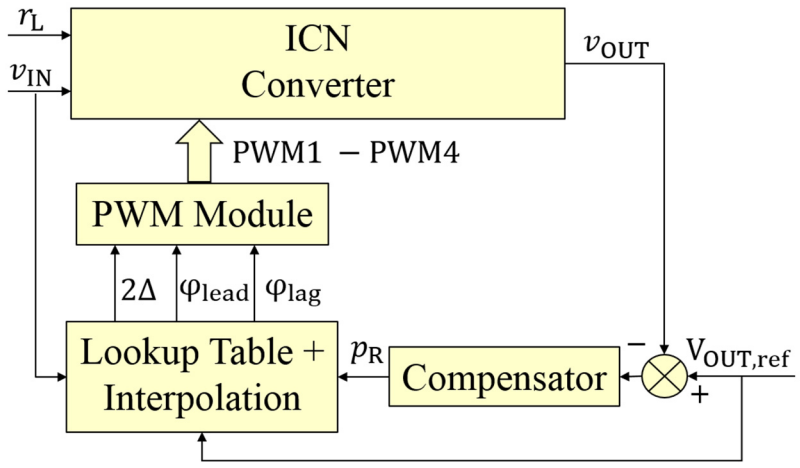

Figure 7.1: Proposed closed-loop control architecture for output voltage regulation in the ICN converter.

table, while the sensed input voltage v_{IN} serves as the third control input. The lookup table then generates the required inverter and rectifier phase shifts, based on the following relationships:

$$2\Delta = 2\cos^{-1}\sqrt{\frac{V_{IN}^2/(4N^2V_{OUT,ref}^2 p_R) - r^2}{1-r^2}}, \tag{7.3}$$

$$\Phi_{lead} = \Delta + \frac{\pi}{2} - \sin^{-1}\sqrt{p_R}, \tag{7.4}$$

$$\Phi_{lag} = \Delta + \frac{\pi}{2} + \sin^{-1}\sqrt{p_R}. \tag{7.5}$$

Here, 2Δ is the phase of the bottom inverter, Φ_{lead} is the phase of the leading leg of the rectifier, and Φ_{lag} is the phase of the lagging leg of the rectifier, all relative to the phase of the top inverter. Applying these phases to the ICN converter of Fig. 6.1 ensures that both output voltage and power regulation as well as soft-switching (ZVS and near-ZCS) are achieved. It is to be noted that utilizing the sensed input voltage v_{IN} as a control input for the lookup table, which represents a feedforward path in the control architecture, ensures that the output voltage of the ICN converter is regulated in the face of wide input voltage variations. The power ratio p_R, which is part of the feedback path in the control architecture, ensures that the output voltage is also regulated in the face of output power variations. This can be intuitively understood as follows: consider a scenario in which the output voltage of the ICN converter is regulated to a certain value, and the output power requirement (load) increases. With no control action taken yet,

the output power delivered by the converter is momentarily less than the power consumed by the load, causing the output voltage to decrease. Referring to Fig. 7.1, this increases the error between the sensed output voltage and its reference, and as a result, the output of the compensator, the power ratio p_{R}, increases. This, in turn, increases the power delivered by the converter, bringing the output voltage back up to its reference value. The feedback and feedforward based control architecture shown in Fig. 7.1 only requires sensing the input and output voltage of the converter, both of which have relative low-frequency variations, and is hence simple and inexpensive to implement. Depending on the required control resolution, the lookup table can also be implemented in a low-cost microcontroller.

7.2 Small-Signal Dynamic Model for the ICN Converter

To facilitate the design of the compensator of the feedback loop shown in Fig. 7.1, a small-signal dynamic model for the ICN resonant converter is developed and shown in Fig. 7.2. This model comprises three parts: a dependent current source (i_{N}), an output resistance (r_{N}), and an output capacitor (C_{OUT}). The dependent current source models the dependence of output current on the power ratio p_{R} , and the output resistance models the dependence of output current i_{out} on the output voltage v_{out}. To obtain the value of the dependent current source and the output resistance, an expression for the accurate average output current of the ICN converter is required. The step-superposition (S2) analysis approach introduced earlier and described in Chapter 3 is used to develop this expression for the average output current. The expression is given by:

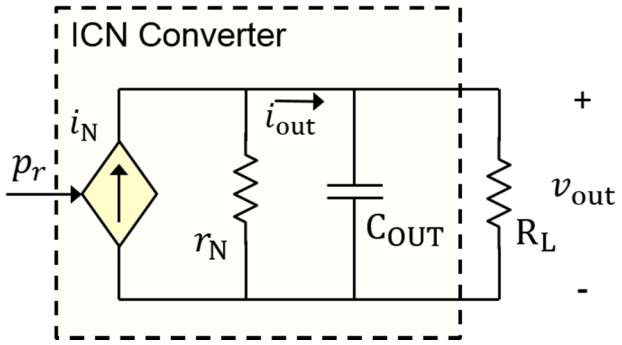

Figure 7.2: Proposed small-signal dynamic model for the ICN converter.

$$i_{\mathrm{OUT}} = f(v_{\mathrm{IN}}, v_{\mathrm{OUT}}, p_{\mathrm{R}}) = 2f_{\mathrm{s}}N(Q_{11} + Q_{12} + Q_{21} + Q_{22}), \tag{7.6}$$

where v_{IN} is the input voltage, v_{OUT} is the output voltage, p_{R} is the power ratio, f_{s} is the switching frequency, N is the transformer turns ratio. Q_{xy} ($x = 1$ or 2, $y = 1$ or 2) is the integration of the component of i_{x} (inverter output current) that is generated by v_{y} (inverter output voltage) over one switching period, and its two components corresponding to the two inverters are given by:

$$Q_{\mathrm{x1}}(t) = \begin{cases} \dfrac{I_{\mathrm{x11}}\left[\cos\left(\frac{\Phi_{\mathrm{lead}}}{2\pi}\omega_1 T_{\mathrm{s}} - \frac{\omega_1 T_{\mathrm{s}}}{4}\right) + \cos\left(-\frac{\Phi_{\mathrm{lag}}}{2\pi}\omega_1 T_{\mathrm{s}} + \frac{3\omega_1 T_{\mathrm{s}}}{4}\right) - 2\cos\left(\frac{\omega_1 T_{\mathrm{s}}}{4}\right)\right]}{2\omega_1 \cos\left(\frac{\omega_1 T_{\mathrm{s}}}{4}\right)} \\ + \dfrac{I_{\mathrm{x12}}\left[\cos\left(\frac{\Phi_{\mathrm{lead}}}{2\pi}\omega_2 T_{\mathrm{s}} - \frac{\omega_2 T_{\mathrm{s}}}{4}\right) + \cos\left(-\frac{\Phi_{\mathrm{lag}}}{2\pi}\omega_2 T_{\mathrm{s}} + \frac{3\omega_2 T_{\mathrm{s}}}{4}\right) - 2\cos\left(\frac{\omega_2 T_{\mathrm{s}}}{4}\right)\right]}{2\omega_2 \cos\left(\frac{\omega_2 T_{\mathrm{s}}}{4}\right)}, \Phi_{\mathrm{lead}} \le \pi \le \Phi_{\mathrm{lag}} \\ \dfrac{I_{\mathrm{x11}}\left[\cos\left(\frac{\Phi_{\mathrm{lead}}}{2\pi}\omega_1 T_{\mathrm{s}} - \frac{\omega_1 T_{\mathrm{s}}}{4}\right) - \cos\left(\frac{\Phi_{\mathrm{lag}}}{2\pi}\omega_1 T_{\mathrm{s}} - \frac{\omega_1 T_{\mathrm{s}}}{4}\right)\right]}{2\omega_1 \cos\left(\frac{\omega_1 T_{\mathrm{s}}}{4}\right)} \\ + \dfrac{I_{\mathrm{x12}}\left[\cos\left(\frac{\Phi_{\mathrm{lead}}}{2\pi}\omega_2 T_{\mathrm{s}} - \frac{\omega_2 T_{\mathrm{s}}}{4}\right) - \cos\left(\frac{\Phi_{\mathrm{lag}}}{2\pi}\omega_2 T_{\mathrm{s}} - \frac{\omega_2 T_{\mathrm{s}}}{4}\right)\right]}{2\omega_2 \cos\left(\frac{\omega_2 T_{\mathrm{s}}}{4}\right)}, \Phi_{\mathrm{lead}} \le \Phi_{\mathrm{lag}} \le \pi \end{cases}, \tag{7.7}$$

$$Q_{\mathrm{x2}}(t) = \begin{cases} \dfrac{I_{\mathrm{x21}}\left[-\cos\left(-\frac{\Phi_{\mathrm{lead}}}{2\pi}\omega_1 T_{\mathrm{s}} - \frac{\omega_1 T_{\mathrm{s}}}{4} + \frac{\Delta}{\pi}\omega_1 T_{\mathrm{s}}\right) + \cos\left(\frac{\Phi_{\mathrm{lag}}}{2\pi}\omega_1 T_{\mathrm{s}} - \frac{\omega_1 T_{\mathrm{s}}}{4} - \frac{\Delta}{\pi}\omega_1 T_{\mathrm{s}}\right) + 2\cos\left(\frac{\omega_1 T_{\mathrm{s}}}{4}\right)\right]}{2\omega_1 \cos\left(\frac{\omega_1 T_{\mathrm{s}}}{4}\right)} \\ + \dfrac{I_{\mathrm{x22}}\left[-\cos\left(-\frac{\Phi_{\mathrm{lead}}}{2\pi}\omega_2 T_{\mathrm{s}} - \frac{\omega_2 T_{\mathrm{s}}}{4} + \frac{\Delta}{\pi}\omega_2 T_{\mathrm{s}}\right) + \cos\left(\frac{\Phi_{\mathrm{lag}}}{2\pi}\omega_2 T_{\mathrm{s}} - \frac{\omega_2 T_{\mathrm{s}}}{4} - \frac{\Delta}{\pi}\omega_2 T_{\mathrm{s}}\right) + 2\cos\left(\frac{\omega_2 T_{\mathrm{s}}}{4}\right)\right]}{2\omega_2 \cos\left(\frac{\omega_2 T_{\mathrm{s}}}{4}\right)}, \Phi_{\mathrm{lead}} \le \Delta \le \Phi_{\mathrm{lag}} \\ \dfrac{I_{\mathrm{x21}}\left[\cos\left(\frac{\Phi_{\mathrm{lead}}}{2\pi}\omega_1 T_{\mathrm{s}} - \frac{\omega_1 T_{\mathrm{s}}}{4} - \frac{\Delta}{\pi}\omega_1 T_{\mathrm{s}}\right) - \cos\left(\frac{\Phi_{\mathrm{lag}}}{2\pi}\omega_1 T_{\mathrm{s}} - \frac{\omega_1 T_{\mathrm{s}}}{4} - \frac{\Delta}{\pi}\omega_1 T_{\mathrm{s}}\right)\right]}{2\omega_1 \cos\left(\frac{\omega_1 T_{\mathrm{s}}}{4}\right)} \\ + \dfrac{I_{\mathrm{x22}}\left[\cos\left(\frac{\Phi_{\mathrm{lead}}}{2\pi}\omega_2 T_{\mathrm{s}} - \frac{\omega_2 T_{\mathrm{s}}}{4} - \frac{\Delta}{\pi}\omega_2 T_{\mathrm{s}}\right) - \cos\left(\frac{\Phi_{\mathrm{lag}}}{2\pi}\omega_2 T_{\mathrm{s}} - \frac{\omega_2 T_{\mathrm{s}}}{4} - \frac{\Delta}{\pi}\omega_2 T_{\mathrm{s}}\right)\right]}{2\omega_2 \cos\left(\frac{\omega_2 T_{\mathrm{s}}}{4}\right)}, \Delta \le \Phi_{\mathrm{lead}} \le \Phi_{\mathrm{lag}} \end{cases}. \tag{7.8}$$

Here, I_{xy1}, I_{xy2}, α_1, α_2, ω_1 and ω_2 are parameters that depend on input voltage, reactive component values, transformer turns ratio and converter losses. Detailed expressions for these parameters are provided in Appendix C. The small-signal parameters i_{N} and r_{N} are then obtained by linearizing the accurate average output current given by (7.6) around the dc operating points of the converter, utilizing the following relationships:

$$i_{\mathrm{N}} = \frac{\partial f}{\partial p_R}, \tag{7.9}$$

$$r_{\mathrm{N}} = \frac{-1}{\partial f / \partial v_{\mathrm{OUT}}}. \tag{7.10}$$

Based on the dynamic model shown in Fig. 7.2, the transfer function from the power ratio $\mathcal{P}_{\mathrm{R}}$ to the output voltage of the ICN converter, hereafter called the control-to-output transfer function, is given by:

$$G_{\mathrm{ICN}}(\mathrm{s}) = \frac{v_{\mathrm{OUT}}(s)}{p_{\mathrm{R}}(s)} = \frac{i_{\mathrm{N}}R}{1+sCR}, \tag{7.11}$$

where $R = \frac{r_{\mathrm{N}}R_{\mathrm{L}}}{r_{\mathrm{N}}+R_{\mathrm{L}}}$. Since the small-signal model of the ICN converter shown in Fig. 7.2 has one state (the converter output voltage), the control-to-output transfer function has a single pole. Figure 7.3 shows how the dc gain and pole location of this transfer function varies with output power, when the input voltage is 18 V and the output voltage is 12 V.

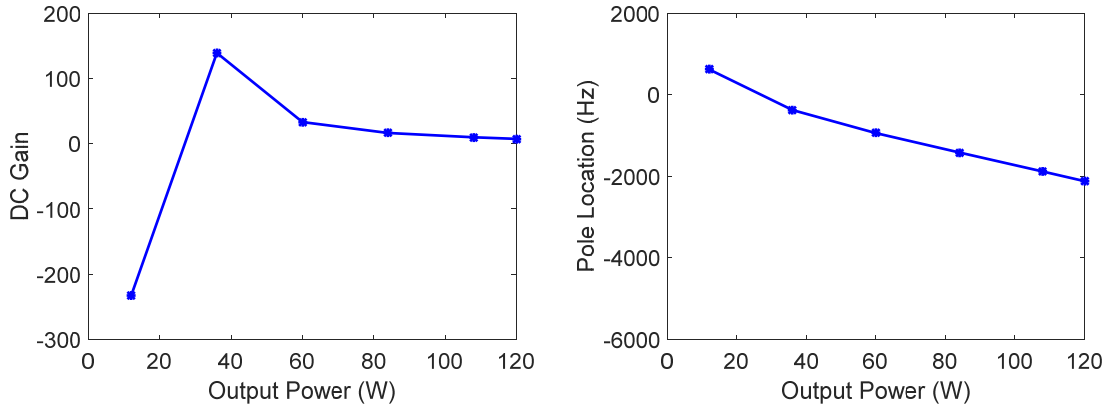

(a) (b)

Figure 7.3: Variations in (a) dc gain and (b) pole location of the control-to-output transfer function of the ICN converter given by (7.11) as a function of the output power of the converter. Here the ICN converter operates with an input voltage of 18 V and an output voltage of 12 V.

7.3 State Feedback Control for the ICN Converter

As can be seen from Fig. 7.3, both the dc gain and pole location of the ICN converter's control-to-output transfer function $G_{\mathrm{ICN}}(\mathrm{s})$ have significant variation as the output power changes for fixed input and output voltages. Figure 7.3(b) shows that the pole of $G_{\mathrm{ICN}}(\mathrm{s})$ moves closer to the right-half plane (RHP) as the output power decreases, eventually entering the RHP at very light loads. This makes it difficult to design a compensator that guarantees good dynamic performance of the closed-loop system at all power levels. To solve this problem, an inner state-feedback loop is introduced in the feedback control architecture, as shown in Fig. 7.4. The sensed output voltage v_{OUT}, which is the only state in the converter model of Fig. 7.2, is scaled by a constant K, and subtracted from the output of the feedback

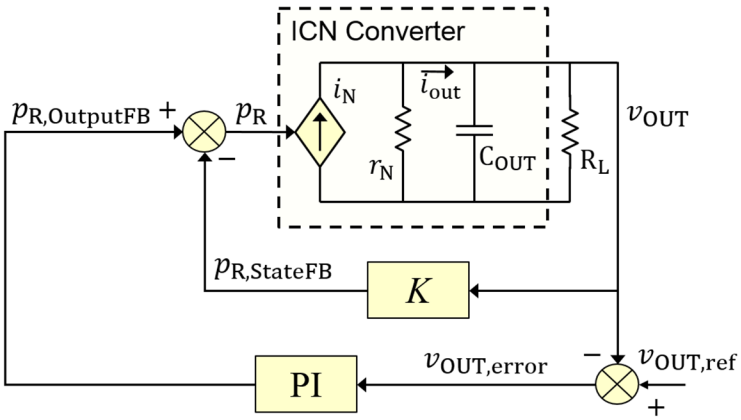

Figure 7.4: New control architecture incorporating an inner state-feedback loop. Appropriately choosing the state-feedback gain K simplifies the design of the outer feedback loop compensator by reducing the sensitivity of the converter's open-loop control-to-output transfer function to operating conditions, and ensuring that the open-loop pole stays in the left-half plane at all power levels.

compensator (shown as a PI compensator in Fig. 7.4). The output of the feedback compensator served as the power ratio p_{R} in the control architecture shown earlier. In comparison, the difference of the compensator output and the scaled output voltage serves as the power ratio in the new architecture of Fig. 7.4. The new control-to-output transfer function of the ICN converter, defined as the transfer function from the output of the feedback compensator ($p_{\mathrm{R,OutputFB}}$ in Fig. 7.4) to the converter output voltage, is obtained by evaluating the closed-loop transfer function of the inner loop, and is given by:

$$G_{\mathrm{ICN,StateFB}}(\mathrm{s}) = \frac{v_{\mathrm{OUT}}(s)}{p_{\mathrm{R,OutputFB}}(s)} = \frac{i_{\mathrm{N}}R}{1+Ki_{\mathrm{N}}R}\frac{1}{1+\frac{sCR}{1+Ki_{\mathrm{N}}R}}, \tag{7.12}$$

Comparing this new control-to-output transfer function to the earlier transfer function given by (7.11), it can be seen that the both the dc gain and the pole location are now modified with factors relating to the state-feedback gain K (note that setting $K = 0$ reduces the new transfer function to the old one). Figure 7.5 shows the variation of the dc gain and pole location of the new transfer function as the ICN converter's output power is varied, when the input voltage is 18 V and the output voltage is 12 V. As compared to Fig. 7.3, the variation of the dc gain is now limited to a narrow range, and the pole is in the left-half plane for all power levels. Owing to the stabilizing effect of this state feedback control,

conventional feedback control is more easily synthesized around the new plant (represented by the inner state-feedback loop), and is far less susceptible to changes in operating conditions.

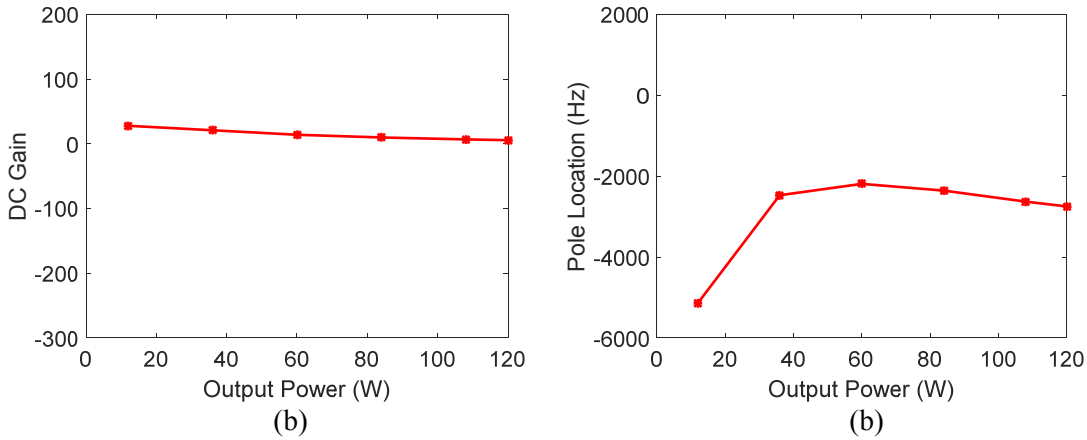

Figure 7.5: Variations in a) dc gain and b) pole of (7.12) as a function of the output power of the ICN converter. Here the ICN converter operates with an input voltage of 18 V and an output voltage of 12 V, and the state feedback constant K is 0.07.

7.4 Closed-Loop Control Simulated and Experimental Results

The above-described closed-loop control is applied to the enhanced phase-shift controlled step-down ICN converter presented in Chapter 6. The control functions, including the feedback compensator and the lookup table, are implemented in a DSP microcontroller, and the control commands (the inverter and rectifier phase-shifts) are updated every switching cycle. The state feedback gain K is selected to be 0.07. A PI controller ($G_{\mathrm{PI}}(s) = K_{\mathrm{p}} + K_{\mathrm{i}}/s$, where $K_{\mathrm{p}} = 0.01$ and $K_{\mathrm{i}} = 1250$) is used to ensure a phase margin greater than 60° across a 10:1 output power range at 18 V input voltage and 12 V output voltage. Figure 7.6 shows the simulated and model-predicted open-loop responses of the converter. As can be seen from Fig. 7.6, the model-predicted open-loop response closely matches the simulated open-loop response. Figure 7.7 shows experimental closed-loop waveforms demonstrating that the closed-loop controller successfully regulates the ICN converter's output voltage in the face of load and input voltage variations.

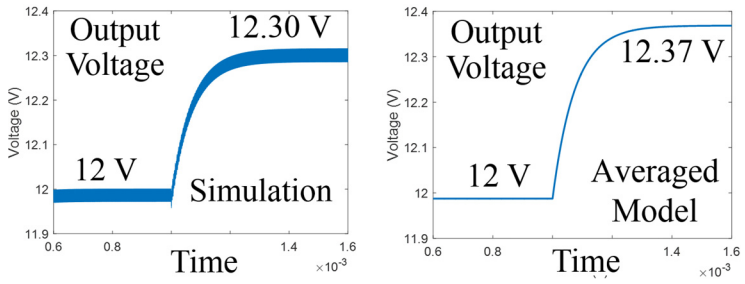

Figure 7.6: Open-loop responses of the ICN converter to a small step change in the power ratio at 18 V input voltage and 120W output power.

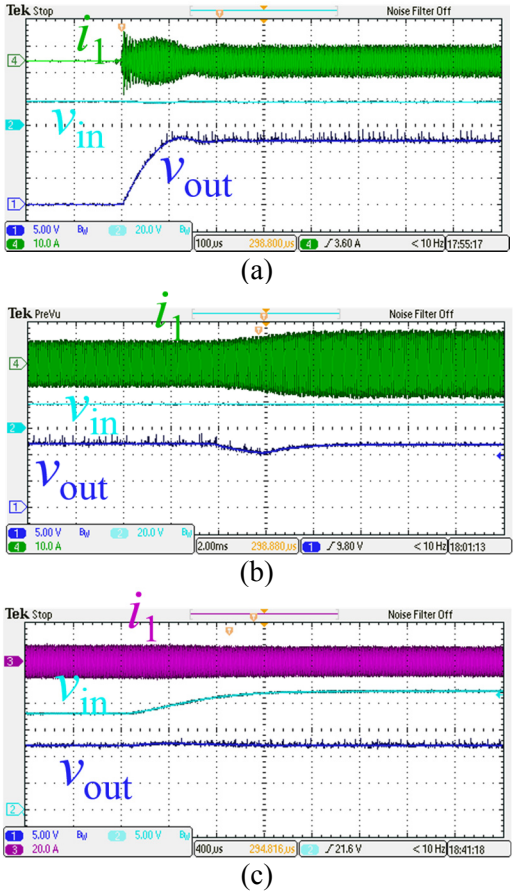

Figure 7.7: Measured waveforms for a) turn-on transient at 36 W output power; b) load step-up transient (6 A to 10 A); c) input voltage ramp-up transient (18 V to 22 V).

Chapter 8

Conclusions

8.1 Summary and Conclusions

Compact isolated converters operating at large conversion ratios are needed for applications ranging from off-line power supplies for electronic loads to solar micro-inverters. Such converters based on conventional architectures often do not achieve very high efficiencies, and their efficiencies typically drop from peak values as the operating conditions change.

Chapter 2 of this thesis introduces a new resonant converter architecture (now also published in [31]-[32], [34]-[40]) that operates at fixed frequency and maintains zero-voltage switching (ZVS) and near-zero-current switching (ZCS) across wide operating ranges in terms of input/output voltages and output power, minimizing device stresses and switching losses, and enabling both high efficiency and power density. Unlike a conventional resonant converter, which utilizes a single inverter and a single rectifier, this Impedance Control Network (ICN) resonant converter has multiple inverters and one or more rectifiers. It also utilizes a lossless impedance control network, which provides a differential phase shift in the voltages and currents, whereby the effective impedances seen at the inverter outputs look highly resistive at the fundamental frequency, enabling switching of the inverters at zero current across wide operating ranges. By modifying the network for slightly inductive loading of the inverters, one can realize simultaneous ZVS and near-ZCS. Hence, the ICN converter is able to maintain high efficiency across wide variations in operating conditions. Furthermore, owing to its soft-switching characteristics, the ICN converter can be operated at high switching frequencies, enabling high power densities. The output voltage and power of the ICN converter can be regulated using burst mode (on/off) control, where the converter is turned on and off periodically at a frequency much lower than its switching frequency.

To optimize the design of the ICN converter, an accurate analysis approach for modeling the ICN converter is required. Resonant converters are typically analyzed and designed using fundamental frequency analysis, wherein network waveforms are approximated by their fundamental components and

switching frequency harmonics are neglected. This approach becomes inaccurate when the converter tank waveforms are significantly non-sinusoidal, as is often the case when the quality factor (Q) of the resonant network is low. There are two (related) general approaches for exact analysis of resonant converters: state space analysis, and state plane analysis. State space analysis is an accurate and general approach to the analysis of resonant converters, but it requires complicated and time-consuming matrix computations. On the other hand, state plane analysis converts the time-domain analysis of resonant converters to geometrical analysis, and simplifies the exact analysis of complicated resonant tank behavior. However, its application is practically limited to simple resonant converters. Chapter 3 of this thesis introduces a new analysis approach to modeling resonant converters that can be used to determine closed-form expressions for the exact resonant network waveforms. This approach, based on superposition of step responses to inverter and rectifier imposed steps, does not require analysis of the different operating modes of a resonant converter, and can easily be applied to resonant converters with high-order resonant networks and multiple inverters and/or rectifiers, such as the ICN converter. In view of its salient features, this approach is termed step-superposition (S2) analysis ([33]). This new modeling approach enables resonant converters with low-Q resonant networks to be accurately analyzed and optimized.

Chapter 4 of this thesis presents three ICN converter prototypes, which cater to a high step-up photovoltaic application that requires input voltages varying between 25 V – 40 V to be converted to output voltages in the range of 250 V – 400 V, while delivering up to 200 W of power (now also published in [31]-[32]). These three ICN converter prototypes differ in terms of the Q-factor of their resonant tanks. The low-Q ICN converter, analyzed and optimized using the S2 analysis approach, is found to perform the best, achieving a peak efficiency of 97.1%, maintaining greater than 96.4% full-power efficiency at 250-V output voltage across the nearly 2:1 input voltage range, and full power efficiency above 95% across its full input and output voltage range. It also maintains efficiency above 94.6% over a 10:1 output power range across its full input and output voltage range.

An issue with burst-mode control is that the converter suffers from non-ZVS transitions during the repeated turn-on transients. To tackle this issue, Chapter 5 of this thesis presents an optimized startup

control to improve the efficiency of ICN converters operating under burst-mode control ([34]). The optimized startup control minimizes the startup transients of the burst-mode operated ICN converters and helps the converters maintain ZVS and near-ZCS operation even during startup. This startup optimization is made possible by applying the above-mentioned S2 analysis to modeling the ICN converter. It reduces the number of non-ZVS startup transitions by 75%, and reduces losses by up to 20%.

Another issue with burst-mode control is that it introduces a low-frequency ripple in the output voltage of the ICN converter, requiring the converter to have large input and output capacitances. Chapter 6 of this thesis addresses this issue by introducing an ICN converter that utilizes enhanced phase-shift control to achieve both soft-switching and output voltage regulation (now also published in [35]). The avoidance of burst-mode control also simplifies the design of the converter's input EMI filter, reduces switch stresses due to startup overshoots, and improves converter efficiency by eliminating startup and shutdown losses as well as by reducing conduction losses when backing off in power. To demonstrate the efficacy of this new control approach, as well as the performance of the ICN converter in high step-down applications, Chapter 6 of this thesis also presents an enhanced phase-shift controlled ICN converter prototype that operates over an input voltage range of 18 V to 75 V, an output voltage of 12 V, and a 10:1 output power range. This prototype ICN converter achieves a peak efficiency of 95.7% and maintains full-power efficiency above 91.7% across its 4:1 input voltage range. Compared to when operated under burst-mode control, the ICN converter with enhanced phase-shift control reduces converter losses by up to 30% and reduces input and output capacitances by two orders of magnitude.

Finally, Chapter 7 of this thesis introduces a closed-loop control approach for the ICN converter. A control architecture incorporating a combination of input feed-forward and output feedback control is utilized to regulate the converter output voltage. To facilitate compensator design of the feedback loop, a small-signal dynamic model for the ICN converter is developed. The parameters of the converter transfer function obtained from this model vary widely across the converter's wide operating range, complicating the compensator design. To address this issue, an additional state feedback controller is included to make the parameters of the transfer function insensitive to the operating conditions. This closed-loop control

approach successfully regulates the output voltage of the step-down ICN converter prototype presented in Chapter 6 over its 4:1 range of input voltage and 10:1 range of output power.

8.2 Recommendations for Future Work

This thesis introduces the ICN resonant converter, develops techniques to optimize its power stage design and presents alternative control strategies to regulate its output power and voltage. However, since the ICN converter is a new type of resonant converter, there are numerous unexplored areas that should be investigated in the future.

One aspect of the ICN converter that merits further exploration is its dynamic model. The dynamic model for the ICN converter developed in this thesis is a first order model valid only in the low frequency range. A more accurate dynamic model is required to predict the higher frequency characteristics of the ICN converter and to facilitate the design of a higher bandwidth controllers for this converter.

In this thesis, the parameters of the state feedback controller and the output feedback controller are designed to have fixed values for the entire operating range of the ICN converter. As a result, the performance of the converter across its full operating range is difficult to optimize. It would be valuable to incorporate a nonlinear control technique, such as gain-scheduling, to improve the closed-loop performance of the ICN converter.

Finally, it would also be useful to investigate the performance of the ICN converter in other potential applications, such as point-of-load converters and bi-directional converters for energy storage applications. For some applications, it would also be valuable to explore other topological variations of the ICN converter architecture.

Bibliography

[1] C. Calwell and T. Reader, "Power Supplies: A Hidden Opportunity for Energy Savings," Report prepared by Ecos Consulting for the National Resources Defense Council, May 2002.

[2] Brian Fortenbery and Jonathan Koomey, "Assessment of the Impacts of Power Factor Correction in Computer Power Supplies on Commercial Building Line Losses," Technical report, EPRI Solutions, March 2006.

[3] R.L. Steigerwald, "High-Frequency Resonant Transistor DC-DC Converters," *IEEE Transactions on Industrial Electronics*, vol. IE-31, no. 2, pp. 181-191, May 1984.

[4] R.L. Steigerwald, "A Comparison of Half-Bridge Resonant Converter Topologies," *IEEE Transactions on Power Electronics*, vol. 3, no. 2, pp. 174-182, April 1988.

[5] J. Vandelac and P.D. Ziogas, "A DC to DC PWM Series Resonant Converter Operated at Resonant Frequency," *IEEE Transactions on Industrial Electronics*, vol. 35, no. 3, pp. 451-460, August 1988.

[6] M.Z. Youssef and P.K. Jain, "A Review and Performance Evaluation of Control Techniques in Resonant Converters," *Proceedings of the IEEE Industrial Electronics Society*, pp. 215-221, Busan, Korea, November, 2004.

[7] F.S. Tsai, P. Materu and F.C. Lee, "Constant-Frequency Clamped-Mode Resonant Converters," *IEEE Transactions on Power Electronics*, vol. 3, no. 4, pp. 460-473, October, 1988.

[8] P. Jain, A. St-Martin and G. Edwards, "Asymmetrical Pulse Width Modulated Resonant DC/DC Converter Topologies," *Proceedings of the IEEE Power Electronics Specialists Conference (PESC)*, pp. 818-825, Seattle, WA, June, 1993.

[9] J.M. Burdio, F. Canales, P.M. Barbosa and F.C. Lee, "A Comparison Study of Fixed-Frequency Control Strategies for ZVS DC/DC Series Resonant Converters," *Proceedings of the IEEE Power Electronics Specialists Conference (PESC)*, pp. 427-432, Vancouver, Canada, June, 2001.

[10] H. Chireix, "High Power Outphasing Modulation," *Proceedings of the IRE*, vol. 23, no.11, pp. 1370-1392, November 1935.

[11] Y. Han, O. Leitermann, D.A. Jackson, J.M. Rivas and D.J. Perreault, "Resistance Compression Networks for Radio-Frequency Power Conversion," *IEEE Transactions on Power Electronics*, pp. 41-53, January 2007.

[12] P.A. Godoy, D.J. Perreault, and J.L. Dawson, "Outphasing Energy Recovery Amplifier with Resistance Compression for Improved Efficiency," *IEEE Transactions on Microwave Theory and Techniques*, vol. 57, no. 12, pp. 2895-2906, December 2009.

[13] D.J. Perreault, "A New Power Combining and Outphasing Modulation System for High-Efficiency Power Amplification," *IEEE Transactions on Circuits and Systems – I*, vol. 58, no. 8, pp. 1713-1726, August 2011.

[14] A.S. Jurkov, L. Roslaniec and D.J. Perreault, "Lossless Multi-Way Power Combining and Outphasing for High-Frequency Resonant Inverters," *IEEE Transactions on Power Electronics*, Vol. 29, No. 4, pp. 1894-1908, April 2014.

[15] W. Inam, K.K. Afridi and D.J. Perreault, "High Efficiency Resonant DC/DC Converter Utilizing a Resistance Compression Network," *IEEE Transactions on Power Electronics*, pp. 4126-4135, vol. 29, no. 8, August 2014.

[16] T.W. Barton, J.L. Dawson and D.J. Perreault, "Experimental Validation of a Four-Way Outphasing Combiner for Microwave Power Amplification," *IEEE Microwave and Wireless Component Letters*, Vol. 23, No. 1, pp. 28-30, Jan. 2013.

[17] T.W. Barton and D.J. Perreault, "Four-Way Microstrip-Based Power Combining for Microwave Outphasing Power Amplifiers," *IEEE Transactions on Circuits and Systems - I*, Vol. 61, No. 10, pp. 2987-2998, October 2014.

[18] T.W. Barton, J. M. Gordonson, and D.J. Perreault, "Transmission Line Resistance Compression Networks and Applications to Wireless Power Transfer," *IEEE Journal of Emerging and Selected Topics in Power Electronics*, Vol. 3, No. 1, pp. 252 - 260, March 2015.

[19] Y. Lee and Y. Cheng, "A 580 kHz switching regulator using on-off control," *Journal of the Institution of Electronic and Radio Engineers*, vol. 57, no. 5, pp. 221–226, September/October 1987.

[20] R.C.N. Pilawa-Podgurski, A.D. Sagneri, J.M. Rivas, D.I. Anderson and D.J. Perreault, "High-Frequency Resonant Boost Converters," *IEEE Transactions on Power Electronics*, vol. 24, No. 6, pp. 1654-1665, June 2009.

[21] J. Hu, A.D. Sagneri, J.M. Rivas, Y. Han, S.M. Davis, and D.J. Perreault, "High-Frequency Resonant SEPIC Converter with Wide Input and Output Voltage Ranges," *IEEE Transactions on Power Electronics*, Vol. 27, No. 1, pp. 189-200, Jan. 2012.

[22] C. R. Sullivan, "Optimal Choice for Number of Strands in a Litz-Wire Transformer Winding", *IEEE Transactions on Power Electronics*, Vol. 14, No. 2, pp. 283-291, Mar. 1999.

[23] J. Muhlethaler, J. Biela, J.W. Kolar and A. Ecklebe, "Core Losses under the DC Bias Condition Based on Steinmetz Parameters," *IEEE Transactions on Power Electronics*, Vol. 27, No. 2, pp. 953-963, Feb. 2012.

[24] L. Scandola, L. Corradini, G. Spiazzi, C. Garbossa, P. Piersimoni and A. Vecchiato, "Online Efficiency Optimization Technique for Digitally Controlled Resonant DC/DC Converters," *Proceedings of the IEEE Applied Power Electronics Conference and Exposition (APEC)*, Fort Worth, TX, March 2014.

[25] A. Sepahvand, L. Scandola, Y. Zhang and D. Maksimovic, "Voltage Regulation and Efficiency Optimization in a 100 MHz Series Resonant DC-DC Converter," *Proceedings of the IEEE Applied Power Electronics Conference and Exposition (APEC)*, Charlotte, NC, March 2015.

[26] H.R.Visser and P.P.J. van den Bosch, "Modeling of Periodically Switching Networks," *Proceedings of the IEEE Power Electronics Specialists Conference (PESC)*, pp. 67-73 Cambridge, MA, June 1991.

[27] O.P. Mandhana and R.G. Hoft, "Steady State Analysis of DC to DC Resonant Converter," *Proceedings of the IEEE Applied Power Electronics Conference (APEC)*, pp. 580-586, Dallas, TX, March 1991.

[28] A. Kumar, J. Lu, and K.K. Afridi, "Enhanced-Accuracy Augmented State-Space Approach to Steady-State Modeling of Resonant Converters," *Proceedings of the IEEE Workshop on Control and Modeling for Power Electronics (COMPEL)*, Vancouver, Canada, July, 2015,

[29] R. Oruganti and F.C. Lee, "Resonant Power Processors, Part I – State Plane Analysis," *IEEE Transactions on Industrial Applications*, vol. IA-21, pp. 1453-1460, November 1985.

[30] W. Feng, F.C. Lee and P. Mattavelli, "Optimal Trajectory Control of Burst Mode for LLC Resonant Converter," *IEEE Transactions on Power Electronics*, vol. 28, no. 1, pp. 457-466, January 2013.

[31] J. Lu, D.J. Perreault, D.M. Otten and K.K. Afridi, "Impedance Control Network Resonant DC-DC Converter for Wide-Range High-Efficiency Operation," *IEEE Transactions on Power Electronics*, vol. 31, no. 7, pp. 5040-5056, July, 2016.

[32] J. Lu, D.J. Perreault and K.K. Afridi, "Impedance Control Network Resonant dc-dc Converter for Wide-range High Efficiency Operation," *Proceedings of the IEEE Applied Power Electronics Conference and Exposition (APEC)*, Charlotte, NC, March 2015.

[33] J. Lu, A. Kumar and K.K. Afridi, "A Step-Superposition Based Analysis Approach to Modeling Resonant Converters," *Proceedings of the IEEE Workshop on Control and Modeling for Power Electronics (COMPEL)*, Vancouver, Canada, July, 2015.

[34] J. Lu and K.K. Afridi, "High Efficiency Impedance Control Network Resonant DC-DC Converter with Optimized Startup Control," *Proceedings of the IEEE Energy Conversion Congress and Exposition (ECCE*), Montreal, Canada, September, 2015.

[35] J. Lu, A. Kumar and K.K. Afridi, "Step-Down Impedance Control Network Resonant DC-DC Converter Utilizing an Enhanced Phase-Shift Control for Wide-Input-Range Operation," *Proceedings of the IEEE Energy Conversion Congress and Exposition (ECCE)*, Milwaukee, WI, September, 2016.

[36] S.J. Gunter, K.K. Afridi, D.M. Otten, R. Abramson and D.J. Perreault, "Impedance Control Network Resonant Step-Down DC-DC Converter Architecture," *Proceedings of the IEEE Energy Conversion Congress and Exposition (ECCE)*, Montreal, Canada, September 2015.

[37] A. Kumar and K.K. Afridi, "Megahertz-Frequency Isolated Resonant dc-dc Converter using Impedance Control Network for High-Efficiency Wide-Range Operation," *Proceedings of the IEEE Energy Conversion Congress and Exposition (ECCE)*, Montreal, Canada, September 2015.

[38] Y. Liu, A. Kumar, J. Lu, D. Maksimovic and K.K. Afridi, "New Design Methodology for Megahertz-Frequency Resonant dc-dc Converters using Impedance Control Network Architecture", *Proceedings of the IEEE Applied Power Electronics Conference and Exposition (APEC)*, Long Beach, CA, March, 2016.

[39] A. Kumar, J. Lu and K.K. Afridi, "Power Density and Efficiency Enhancement in Impedance Control Network Resonant DC-DC Converters Using Topology Morphing Control," *Proceedings of the IEEE Workshop on Control and Modeling for Power Electronics (COMPEL)*, Trondheim, Norway, June, 2016.

[40] A. Kumar, J. Lu, S. Pervaiz, A. Sepahvand and K.K. Afridi, "High Power Density Impedance Control Network DC-DC Converter Utilizing an Integrated Magnetic Structure," *Proceedings of the IEEE Energy Conversion Congress and Exposition (ECCE)*, Milwaukee, WI, September, 2016.

[41] R.W. Erickson and D. Maksimovic, "Resonant Conversion," in *Fundamentals of Power Electronics*, 2nd ed. New York, NY, USA: Springer, 2001.

Appendix A

Effective Admittance and Output Power of ICN Converter

This appendix derives the expression for the effective admittances seen by the two inverters (Y_1 and Y_2), as given by (2.1), and the expression for the output power of the ICN converter under fundamental frequency approximation, as given by (2.3).

Figure A.1 shows an equivalent circuit model for the ICN converter of Fig. 2.3 under fundamental frequency approximation. In this model, $\hat{V}_1$ and $\hat{V}_2$ are the fundamental components of the output voltages of the inverters, $\hat{I}_1$ and $\hat{I}_2$ are the fundamental components of the output currents of the inverters, and R_x is the equivalent resistance of the rectifier referred to the primary side of the transformer. The expressions for $\hat{V}_1$, $\hat{V}_2$ and R_x are given below:

$$\hat{V}_1 = \frac{2}{\pi} V_{IN} e^{j\Delta}, \tag{A.1}$$

$$\hat{V}_2 = \frac{2}{\pi} V_{IN} e^{-j\Delta}, \tag{A.2}$$

$$R_X = \frac{2V_{OUT}^2}{\pi^2 N^2 P_{OUT}}. \tag{A.3}$$

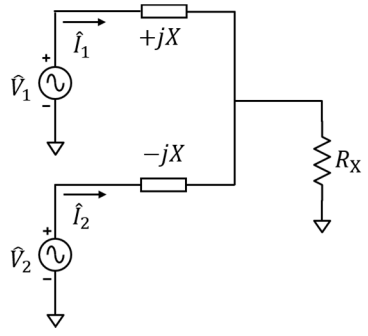

Figure A.1: An equivalent circuit model for the ICN converter of Fig. 2.3 under fundamental frequency approximation. The two input branches of the impedance control network have equal but opposite reactances ($+jX$ and $-jX$). $\hat{V}_1$ and $\hat{V}_2$ are the fundamental components of the output voltages of the inverters, $\hat{I}_1$ and $\hat{I}_2$ are the fundamental components of the output currents of the inverters, and R_X is the equivalent resistance of the rectifier referred to the primary side of the transformer.

Here V_{IN} is the input voltage, V_{OUT} is the output voltage, P_{OUT} is the output power, N is the transformer turns ratio, and 2Δ is the phase shift between the two inverters. The expressions for $\hat{I}_1$ and $\hat{I}_2$ can be derived using superposition:

$$\hat{I}_1 = \frac{R_X - jX}{X^2}\hat{V}_1 - \frac{R_X}{X^2}\hat{V}_2, \tag{A.4}$$

$$\hat{I}_2 = \frac{R_X + jX}{X^2}\hat{V}_2 - \frac{R_X}{X^2}\hat{V}_1. \tag{A.5}$$

Hence, the effective admittances seen by the two inverters are given by:

$$Y_1 \equiv \frac{\hat{I}_1}{\hat{V}_1} = \frac{R_X - jX}{X^2} - \frac{R_X}{X^2}e^{-j2\Delta}, \tag{A.6}$$

$$Y_2 \equiv \frac{\hat{I}_2}{\hat{V}_2} = \frac{R_X + jX}{X^2} - \frac{R_X}{X^2}e^{j2\Delta}. \tag{A.7}$$

Here, R_x is an unknown that can be eliminated using (A.3) and an additional expression relating R_x and output power, as follows. Assuming a lossless converter, output power is equal to input power:

$$P_{OUT} = P_{IN} = \mathrm{Re}\left\{\frac{1}{2}\hat{V}_1\hat{V}_1^* Y_1^* + \frac{1}{2}\hat{V}_2\hat{V}_2^* Y_2^*\right\} = \left(\frac{2}{\pi}V_{IN}\right)^2 \frac{R_X}{X^2}(1-\cos 2\Delta). \tag{A.8}$$

Combining (A.3) and (A.8) yields an expression for R_x that is in terms of given quantities:

$$R_X = \frac{V_{OUT}X}{2NV_{IN}\sin\Delta}. \tag{A.9}$$

Substituting (A.9) into (A.6) and (A.7) gives the desired expression for the effective admittances seen by the two inverters, which is the same as (1):

$$Y_1 = Y_2^* = \frac{V_{OUT}\sin\Delta}{NV_{IN}X} + j\left(\frac{V_{OUT}\cos\Delta}{NV_{IN}X} - \frac{1}{X}\right). \tag{A.10}$$

Now, substituting R_x, as given by (A.9), into the expression for output power, as given by (A.8), gives:

$$P_{OUT} = \frac{4V_{IN}V_{OUT}\sin\Delta}{\pi^2 NX}. \tag{A.11}$$

The effective susceptance seen by both inverters is zero when the phase shift between them is given by:

$$2\Delta = 2\cos^{-1}\left(\frac{NV_{\text{IN}}}{V_{\text{OUT}}}\right). \tag{A.12}$$

Substituting (A.12) into (A.11) yields the desired expression for the output power of the ICN converter when operated with both inverters seeing zero effective susceptance, which is the same as (2.3):

$$P_{\text{OUT}} = \frac{4V_{\text{IN}}\sqrt{V_{\text{OUT}}^2 - N^2V_{\text{IN}}^2}}{\pi^2 NX}. \tag{A.13}$$

Appendix B

Closed-form Expressions for the Summation of Time-shifted Decaying Sinusoidal Functions

The summation of a series of time-shifted decaying sinusoidal functions, as given below:

$$y_{\text{sum}}(t) = \sum_{m=0}^{K-1} e^{-\alpha\left(t'_{\text{K}}+mT_{\text{s}}\right)} \sin \omega_{\text{d}}(t'_{\text{K}} + mT_{\text{s}}). \tag{B.1}$$

Using Euler's formula, (B.1) can be expressed as follows:

$$y_{\text{sum}}(t) = \sum_{m=0}^{K-1} e^{-\alpha\left(t'_{\text{K}}+mT_{\text{s}}\right)} \frac{e^{j\omega_{\text{d}}\left(t'_{\text{K}}+mT_{\text{s}}\right)} - e^{-j\omega_{\text{d}}\left(t'_{\text{K}}+mT_{\text{s}}\right)}}{2j}. \tag{B.2}$$

Rearranging (B.2) yields:

$$y_{\text{sum}}(t) = \frac{e^{(-\alpha+j\omega_{\text{d}})t'_{\text{K}}}}{2j} \sum_{m=0}^{K-1} e^{(-\alpha+j\omega_{\text{d}})mT_{\text{s}}} - \frac{e^{(-\alpha-j\omega_{\text{d}})t'_{\text{K}}}}{2j} \sum_{m=0}^{K-1} e^{(-\alpha-j\omega_{\text{d}})mT_{\text{s}}}. \tag{B.3}$$

Under the light damping condition ($\alpha \approx 0$), (B.3) can be expressed as:

$$y_{\text{sum}}(t) = \frac{e^{j\omega_{\text{d}}t'_{\text{K}}}}{2j} \frac{1-e^{-\alpha(K-1)T_{\text{s}}} \cdot e^{j\omega_{\text{d}}(K-1)T_{\text{s}}}}{1-e^{j\omega_{\text{d}}T_{\text{s}}}} - \frac{e^{-j\omega_{\text{d}}t'_{K}}}{2j} \frac{1-e^{-\alpha(K-1)T_{\text{s}}} \cdot e^{-j\omega_{\text{d}}(K-1)T_{\text{s}}}}{1-e^{-j\omega_{\text{d}}T_{\text{s}}}}, \tag{B.4}$$

which can be further expressed as:

$$y_{\text{sum}}(t) = \frac{1}{2j} \frac{\left[e^{j\omega_{\text{d}}t'_{K}}\right]\left[1-e^{-\alpha(K-1)T_{\text{s}}} \cdot e^{j\omega_{\text{d}}(K-1)T_{\text{s}}}\right]\left[1-e^{-j\omega_{\text{d}}T_{\text{s}}}\right] - \left[e^{-j\omega_{\text{d}}t'_{K}}\right]\left[1-e^{-\alpha(K-1)T_{\text{s}}} \cdot e^{-j\omega_{\text{d}}(K-1)T_{\text{s}}}\right]\left[1-e^{j\omega_{\text{d}}T_{\text{s}}}\right]}{\left[1-e^{j\omega_{\text{d}}T_{\text{s}}}\right]\left[1-e^{-j\omega_{\text{d}}T_{\text{s}}}\right]}. \tag{B.5}$$

Letting $A = \left[e^{j\omega_{\text{d}}t'_{K}}\right]\left[1 - e^{-\alpha(K-1)T_{\text{s}}} \cdot e^{j\omega_{\text{d}}(K-1)T_{\text{s}}}\right]\left[1 - e^{-j\omega_{\text{d}}T_{\text{s}}}\right]$, (B.5) can be expressed as:

$$y_{\text{sum}}(t) = \frac{1}{2j} \frac{A-A^*}{\left[1-e^{j\omega_{\text{d}}T_{\text{s}}}\right]\left[1-e^{-j\omega_{\text{d}}T_{\text{s}}}\right]}. \tag{B.6}$$

Using double angle identities, (B.6) can be further simplified into:

$$y_{\text{sum}}(t) = \frac{1}{8j} \cdot \frac{A-A^*}{\sin^2\left(\frac{\omega_{\text{d}}T_{\text{s}}}{2}\right)}. \tag{B.7}$$

By expanding A and using Euler's formula, $A - A^*$ can be expressed as:

$$A - A^* = 4j\left[\cos\left(\omega_d t'_{\text{K}} - \frac{\omega_{\text{d}}T_{\text{s}}}{2}\right)\sin\left(\frac{\omega_{\text{d}}T_{\text{s}}}{2}\right) - e^{-\alpha(K-1)T_s}\cos\left(\omega_{\text{d}}t'_{\text{K}} - \omega_{\text{d}}T_{\text{s}} + \omega_d KT_s - \frac{\omega_{\text{d}}T_{\text{s}}}{2}\right)\sin\left(\frac{\omega_{\text{d}}T_{\text{s}}}{2}\right)\right].$$

(B.8)

Substituting (B.8) into (B.7) yields:

$$y_{\mathrm{sum}}(t) = \frac{\cos\left(\omega_{\mathrm{d}} t'_{\mathrm{K}} - \frac{\omega_{\mathrm{d}} T_{\mathrm{s}}}{2}\right) - e^{-\alpha(K-1)T_{\mathrm{s}}} \cos\left(\omega_{\mathrm{d}} t'_{\mathrm{K}} + \omega_{\mathrm{d}} K T_{\mathrm{s}} - \omega_{\mathrm{d}} T_{\mathrm{s}} - \frac{\omega_{\mathrm{d}} T_{\mathrm{s}}}{2}\right)}{2\sin\left(\frac{\omega_{\mathrm{d}} T_{\mathrm{s}}}{2}\right)}. \quad \text{(B.9)}$$

When *K* approaches infinity (which implies that the converter reaches steady state), (B.9) can be simplified into:

$$y_{\mathrm{sum}}(t) = \frac{\cos\left(\omega_{\mathrm{d}} t'_{\mathrm{K}} - \frac{\omega_{\mathrm{d}} T_{\mathrm{s}}}{2}\right)}{2\sin\left(\frac{\omega_{\mathrm{d}} T_{\mathrm{s}}}{2}\right)}. \quad \text{(B.10)}$$

Appendix C

Derivations of Expressions for Inverter Output Currents of ICN Converter

This appendix presents the derivation of closed-form expressions for the inverter output currents of the ICN converter. Figure C.1 shows one implementation of an ICN converter. Under S2 analysis, the switch-

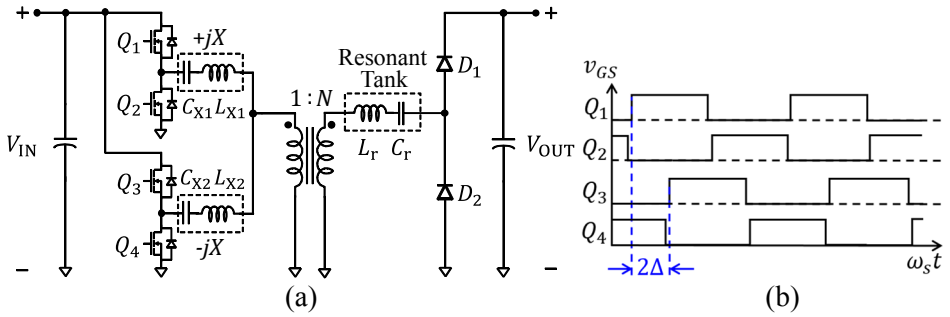

Figure C.1: One implementation of an impedance control network (ICN) resonant converter, appropriate for voltage step-up: (a) converter topology and (b) switch gating signals.

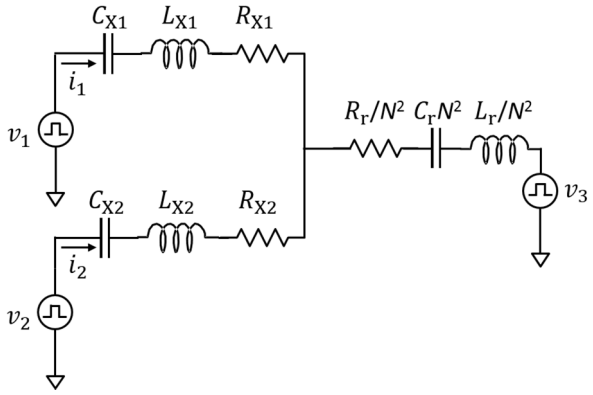

Figure C.2: Equivalent circuit model for the ICN converter of Fig. C.1. The resistors model converter losses.

node voltages of the two inverters and the rectifier of this converter are modeled as square-wave voltage sources, as shown in the equivalent circuit of Fig. C.2. These square-wave sources can be decomposed into a sum of time-shifted positive and negative steps, as given by:

$$v_1(t) = \begin{cases} V_{1,\text{ini}} - V_{1,\text{ini}}u(\text{t}) + \sum_{m=0}^{N-1} V_{\text{IN}}u(t'_{\text{K}} + mT_{\text{s}}) - \\ \sum_{m=1}^{N-1} V_{\text{IN}}u\left(t'_{\text{K}} - \frac{T_{\text{s}}}{2} + mT_{\text{s}}\right) \end{cases}, \quad 0 \le t'_{\text{K}} < \frac{T_{\text{s}}}{2}$$
$$\begin{cases} V_{1,\text{ini}} - V_{1,\text{ini}}u(\text{t}) + \sum_{m=0}^{N-1} V_{\text{IN}}u(t'_{\text{K}} + mT_{\text{s}}) - \\ \sum_{m=0}^{N-1} V_{\text{IN}}u\left(t'_{\text{K}} - \frac{T_{\text{s}}}{2} + mT_{\text{s}}\right) \end{cases}, \quad \frac{T_{\text{s}}}{2} \le t'_{\text{K}} < T_{\text{s}} \qquad \text{(C.1)}$$

$$v_2(t) = \begin{cases} V_{2,\text{ini}} - V_{2,\text{ini}}u(t-2\Delta_t) + \sum_{m=1}^{N-1} V_{\text{IN}}u(t'_{\text{K}} - 2\Delta_t + mT_{\text{s}}) - \\ \sum_{m=1}^{N-1} V_{\text{IN}}u\left(t'_{\text{K}} - 2\Delta_t - \frac{T_{\text{s}}}{2} + mT_{\text{s}}\right) \end{cases}, \; 0 \le t'_{\text{K}} < 2\Delta_t$$
$$\begin{cases} V_{2,\text{ini}} - V_{2,\text{ini}}u(t-2\Delta_t) + \sum_{m=0}^{N-1} V_{\text{IN}}u(t'_{\text{K}} - 2\Delta_t + mT_{\text{s}}) - \\ \sum_{m=1}^{N-1} V_{\text{IN}}u\left(t'_{\text{K}} - 2\Delta_t - \frac{T_{\text{s}}}{2} + mT_{\text{s}}\right) \end{cases}, 2\Delta_t \le t'_{\text{K}} < 2\Delta_t + \frac{T_{\text{s}}}{2}, \quad \text{(C.2)}$$
$$\begin{cases} V_{2,\text{ini}} - V_{2,\text{ini}}u(t-2\Delta_t) + \sum_{m=0}^{N-1} V_{\text{IN}}u(t'_{\text{K}} - 2\Delta_t + mT_{\text{s}}) - \\ \sum_{m=0}^{N-1} V_{\text{IN}}u\left(t'_{\text{K}} - 2\Delta_t - \frac{T_{\text{s}}}{2} + mT_{\text{s}}\right) \end{cases}, 2\Delta_t + \frac{T_{\text{s}}}{2} \le t'_{\text{K}} < T_{\text{s}}$$

$$v_3(t) = \frac{1}{N} \cdot \begin{cases} V_{3,\text{ini}} - V_{3,\text{ini}}u(t-T_{\text{r}}) + \sum_{m=1}^{N-1} V_{\text{OUT}}u(t'_{\text{K}} - T_{\text{r}} + mT_{\text{s}}) - \\ \sum_{m=1}^{N-1} V_{\text{OUT}}u\left(t'_{\text{K}} - T_{\text{r}} - \frac{T_{\text{s}}}{2} + mT_{\text{s}}\right) \end{cases}, \; 0 \le t'_{\text{K}} < T_{\text{r}}$$
$$\begin{cases} V_{3,\text{ini}} - V_{3,\text{ini}}u(t-T_{\text{r}}) + \sum_{m=0}^{N-1} V_{\text{OUT}}u(t'_{\text{K}} - T_{\text{r}} + mT_{\text{s}}) - \\ \sum_{m=1}^{N-1} V_{\text{OUT}}u\left(t'_{\text{K}} - T_{\text{r}} - \frac{T_{\text{s}}}{2} + mT_{\text{s}}\right) \end{cases}, \; T_{\text{r}} \le t'_{\text{K}} < T_{\text{r}} + \frac{T_{\text{s}}}{2}. \quad \text{(C.3)}$$
$$\begin{cases} V_{3,\text{ini}} - V_{3,\text{ini}}u(t-T_{\text{r}}) + \sum_{m=0}^{N-1} V_{\text{OUT}}u(t'_{\text{K}} - T_{\text{r}} + mT_{\text{s}}) - \\ \sum_{m=0}^{N-1} V_{\text{OUT}}u\left(t'_{\text{K}} - T_{\text{r}} - \frac{T_{\text{s}}}{2} + mT_{\text{s}}\right) \end{cases}, \; T_{\text{r}} + \frac{T_{\text{s}}}{2} \le t'_{\text{K}} < T_{\text{s}}$$

Here, $v_1(t)$ and $v_2(t)$ model the switch-node voltages of the top and bottom inverters, respectively, and $v_3(t)$ models the switch-node voltage of the rectifier. $V_{1,\text{ini}}$, $V_{2,\text{ini}}$ and $V_{3,\text{ini}}$ are the voltages at the switch nodes of the two inverters and the rectifier before the converter is turned on, t is taken to be zero when the converter is turned on, T_{s} is the switching period of the converter, K (=1, 2, …) is the number of the switching cycles that have passed since the converter was turned on, including the current switching cycle (the K^{th} switching cycle), and t'_{K} is the time elapsed within the current switching cycle. The relationship between t, t'_{K} and K is given by:

$$t'_{\text{K}} = t - (K-1)T_{\text{s}}. \quad \text{(C.4)}$$

Each of the inverter and rectifier imposed steps in (C.1) – (C.3) produces a response in the resonant tank currents of the ICN converter. The inverter output currents of the ICN converter (i_1 and i_2 in Fig. C.2) are obtained by summing all these responses. This is done systematically by splitting the inverter output currents into three components, two generated as a response to the steps imposed by the two inverters (given in (C.1) and C.2)), and the third generated by the steps imposed by the rectifier (given in (C.3)), as under:

$$i_1(t) = i_{11}(t) + i_{12}(t) + i_{13}(t), \quad \text{(C.5)}$$

$$i_2(t) = i_{21}(t) + i_{22}(t) + i_{23}(t). \quad \text{(C.6)}$$

Here, $i_{\mathrm{xy}}(t)$ is the component of i_{x} generated by v_{y} (where *x* signifies the two inverters and equals 1 or 2, and y signifies the two inverters and the rectifier and equals 1, 2 or 3, as shown in Fig. C.2). The three components of the inverter output currents are individually expressed as:

$$i_{\mathrm{x1}}(t)=\begin{cases}-\frac{V_{\mathrm{1,ini}}}{V_{\mathrm{IN}}}i_{\mathrm{x1,step}}(\mathrm{t})+\sum_{m=0}^{N-1}i_{\mathrm{x1,step}}(t'_{\mathrm{K}}+mT_{\mathrm{s}})-\\ \sum_{m=1}^{N-1}i_{\mathrm{x1,step}}\left(t'_{\mathrm{K}}-\frac{T_{\mathrm{s}}}{2}+mT_{\mathrm{s}}\right) & ,\ 0\le t'_{\mathrm{K}}<\frac{T_{\mathrm{s}}}{2}\\ -\frac{V_{\mathrm{1,ini}}}{V_{\mathrm{IN}}}i_{\mathrm{x1,step}}(\mathrm{t})+\sum_{m=0}^{N-1}i_{\mathrm{x1,step}}(t'_{\mathrm{K}}+mT_{\mathrm{s}})-\\ \sum_{m=0}^{N-1}i_{\mathrm{x1,step}}\left(t'_{\mathrm{K}}-\frac{T_{\mathrm{s}}}{2}+mT_{\mathrm{s}}\right) & ,\ \frac{T_{\mathrm{s}}}{2}\le t'_{\mathrm{K}}<T_{\mathrm{s}}\end{cases}, \tag{C.7}$$

$$i_{\mathrm{x2}}(t)=\begin{cases}-\frac{V_{\mathrm{2,ini}}}{V_{\mathrm{IN}}}i_{\mathrm{x2,step}}(t-2\Delta_t)+\sum_{m=1}^{N-1}i_{\mathrm{x2,step}}(t'_{\mathrm{K}}-2\Delta_t+mT_{\mathrm{s}})-\\ \sum_{m=1}^{N-1}i_{\mathrm{x2,step}}\left(t'_{\mathrm{K}}-2\Delta_t-\frac{T_{\mathrm{s}}}{2}+mT_{\mathrm{s}}\right) & ,\ 0\le t'_{\mathrm{K}}<2\Delta_t\\ -\frac{V_{\mathrm{2,ini}}}{V_{\mathrm{IN}}}i_{\mathrm{x2,step}}(t-2\Delta_t)+\sum_{m=0}^{N-1}i_{\mathrm{x2,step}}(t'_{\mathrm{K}}-2\Delta_t+mT_{\mathrm{s}})-\\ \sum_{m=1}^{N-1}i_{\mathrm{x2,step}}\left(t'_{\mathrm{K}}-2\Delta_t-\frac{T_{\mathrm{s}}}{2}+mT_{\mathrm{s}}\right) & ,2\Delta_t\le t'_{\mathrm{K}}<2\Delta_t+\frac{T_{\mathrm{s}}}{2}\\ -\frac{V_{\mathrm{2,ini}}}{V_{\mathrm{IN}}}i_{\mathrm{x2,step}}(t-2\Delta_t)+\sum_{m=0}^{N-1}i_{\mathrm{x2,step}}(t'_{\mathrm{K}}-2\Delta_t+mT_{\mathrm{s}})-\\ \sum_{m=0}^{N-1}i_{\mathrm{x2,step}}\left(t'_{\mathrm{K}}-2\Delta_t-\frac{T_{\mathrm{s}}}{2}+mT_{\mathrm{s}}\right) & ,2\Delta_t+\frac{T_{\mathrm{s}}}{2}\le t'_{\mathrm{K}}<T_{\mathrm{s}}\end{cases} \tag{C.8}$$

$$i_{\mathrm{x3}}(t)=\begin{cases}-\frac{V_{\mathrm{3,ini}}}{V_{\mathrm{OUT}}}i_{\mathrm{x3,step}}(t-T_{\mathrm{r}})+\sum_{m=1}^{N-1}i_{\mathrm{x3,step}}(t'_{\mathrm{K}}-T_{\mathrm{r}}+mT_{\mathrm{s}})-\\ \sum_{m=1}^{N-1}i_{\mathrm{x3,step}}\left(t'_{\mathrm{K}}-T_{\mathrm{r}}-\frac{T_{\mathrm{s}}}{2}+mT_{\mathrm{s}}\right) & ,\ 0\le t'_{\mathrm{K}}<T_{\mathrm{r}}\\ -\frac{V_{\mathrm{3,ini}}}{V_{\mathrm{OUT}}}i_{\mathrm{x3,step}}(t-T_{\mathrm{r}})+\sum_{m=0}^{N-1}i_{\mathrm{x3,step}}(t'_{\mathrm{K}}-T_{\mathrm{r}}+mT_{\mathrm{s}})-\\ \sum_{m=1}^{N-1}i_{\mathrm{x3,step}}\left(t'_{\mathrm{K}}-T_{\mathrm{r}}-\frac{T_{\mathrm{s}}}{2}+mT_{\mathrm{s}}\right) & ,\ T_{\mathrm{r}}\le t'_{\mathrm{K}}<T_{\mathrm{r}}+\frac{T_{\mathrm{s}}}{2}\\ -\frac{V_{\mathrm{3,ini}}}{V_{\mathrm{OUT}}}i_{\mathrm{x3,step}}(t-T_{\mathrm{r}})+\sum_{m=0}^{N-1}i_{\mathrm{x3,step}}(t'_{\mathrm{K}}-T_{\mathrm{r}}+mT_{\mathrm{s}})-\\ \sum_{m=0}^{N-1}i_{\mathrm{x3,step}}\left(t'_{\mathrm{K}}-T_{\mathrm{r}}-\frac{T_{\mathrm{s}}}{2}+mT_{\mathrm{s}}\right) & ,\ T_{\mathrm{r}}+\frac{T_{\mathrm{s}}}{2}\le t'_{\mathrm{K}}<T_{\mathrm{s}}\end{cases}. \tag{C.9}$$

Here, $i_{\mathrm{xy,step}}(t)$ is the response of the inverter output current i_{x} to a step in the inverter/rectifier switch-node voltage v_{y}. The magnitude of this step equals the input voltage V_{IN} when the step is in the inverter switch-node voltages, and the output voltage V_{OUT} when the step is in the rectifier switch-node voltage. For instance, $i_{\mathrm{11,step}}(t)$ is the response of the top inverter output current to a step of magnitude V_{IN} in the top inverter switch-node voltage. $i_{\mathrm{xy,step}}(t)$ is given by a sum of two exponentially decaying sinusoidal functions, as follows:

$$i_{\mathrm{xy,step}}(t) = I_{\mathrm{xy1}} e^{-\alpha_1 t} \sin \omega_1 t + I_{\mathrm{xy2}} e^{-\alpha_2 t} \sin \omega_2 t, \tag{C.10}$$

where I_{xy1}, I_{xy2}, α_1, α_2, ω_1 and ω_2 are parameters that depend on input voltage, output voltage, reactive component values, transformer turns ratio and converter losses.

These parameters can be obtained by evaluating the ICN converter model of Fig. C.2 in the frequency domain. The inverter output currents are expressed in the frequency domain as:

$$i_1(s) = \frac{v_1(s)[Z_2(s)+Z_3(s)]}{Z(s)} - \frac{v_2(s)Z_3(s)}{Z(s)} - \frac{v_3(s)Z_2(s)}{Z(s)}, \tag{C.11}$$

$$i_2(s) = \frac{v_2(s)[Z_1(s)+Z_3(s)]}{Z(s)} - \frac{v_1(s)Z_3(s)}{Z(s)} - \frac{v_3(s)Z_1(s)}{Z(s)}. \tag{C.12}$$

Here, $Z_1(s)$, Z_2(s) and $Z_3(s)$ are the impedances of the three resonant tanks, given by:

$$Z_1(s) = L_{\mathrm{X1}} s + R_{\mathrm{X1}} + \frac{1}{sC_{\mathrm{X1}}}, \tag{C.13}$$

$$Z_2(s) = L_{\mathrm{X2}} s + R_{\mathrm{X2}} + \frac{1}{sC_{\mathrm{X2}}}, \tag{C.14}$$

$$Z_3(s) = \frac{L_{\mathrm{r}}}{N^2} s + \frac{R_{\mathrm{r}}}{N^2} + \frac{1}{sC_{\mathrm{r}}N^2}, \tag{C.15}$$

and $Z(s)$ is given by:

$$Z(s) = Z_1(s)Z_2(s) + Z_1(s)Z_3(s) + Z_2(s)Z_3(s). \tag{C.16}$$

Rearranging (C.11) and (C.12), the inverter output currents can be expressed as:

$$i_1(s) = \frac{s}{f(s)}\big([f_2(s) + f_3(s)]v_1(s) - f_3(s)v_2(s) - f_2(s)v_3(s)\big), \tag{C.17}$$

$$i_2(s) = \frac{s}{f(s)}\big([f_1(s) + f_3(s)]v_2(s) - f_3(s)v_1(s) - f_1(s)v_3(s)\big), \tag{C.18}$$

where $f_1(s)$, $f_2(s)$, and $f_3(s)$ are given by:

$$f_1(s) = L_{\mathrm{X1}} s^2 + R_{\mathrm{X1}} s + \frac{1}{C_{\mathrm{X1}}}, \tag{C.19}$$

$$f_2(s) = L_{\mathrm{X2}} s^2 + R_{\mathrm{X2}} s + \frac{1}{C_{\mathrm{X2}}}, \tag{C.20}$$

$$f_3(s) = \frac{L_{\mathrm{r}}}{N^2} s^2 + \frac{R_{\mathrm{r}}}{N^2} s + \frac{1}{C_{\mathrm{r}}N^2}, \tag{C.21}$$

and $f(s)$ is given by:

$$f(s) = f_1(s)f_2(s) + f_1(s)f_3(s) + f_2(s)f_3(s). \tag{C.22}$$

The parameters in (C.10) can now be systematically obtained by applying a step to one of the inverter/rectifier switch-node voltages, while the other two voltages are set to zero. For instance, consider a step of magnitude V_{IN} in the top inverter switch-node voltage, that is, $v_1(s) = \frac{V_{\text{IN}}}{s}$, while $v_2(s) = 0$ and $v_3(s) = 0$. Applying these conditions to (C.17) and (C.18), the responses of the two inverter output currents to the step in $v_1(s)$ are given by:

$$i_{11,\text{step}}(s) = V_{\text{IN}} \frac{f_2(s)+f_3(s)}{f(s)}, \tag{C.23}$$

$$i_{21,\text{step}}(s) = V_{\text{IN}} \frac{-f_3(s)}{f(s)}. \tag{C.24}$$

It can be seen from (C.23) and (C.24) that the poles of $i_{u,11}(s)$ and $i_{u,21}(s)$ are given by the two pairs of complex-conjugate roots of the fourth-order polynomial $f(s)$. The absolute value of the real parts of these poles correspond to the exponential coefficients (α_1 and α_2), while the absolute value of the imaginary parts correspond to the damped frequencies (ω_1 and ω_2) in (C.10). Values for the parameters α_1, α_2, ω_1 and ω_2 can be obtained by numerically solving $f(s) = 0$. This procedure is repeated by applying steps to the bottom inverter and rectifier switch-node voltages. It can be observed that the poles of the step responses in each case are given by the roots of the same polynomial $f(s)$.Therefore, α_1, α_2, ω_1 and ω_2 are the same for all combinations of the inverter/rectifier switch-node voltages (indexed by y) and inverter output currents (indexed by x). The magnitude parameters I_{xy1} and I_{xy2} in (C.10) are obtained by evaluating the zeroes of the step responses of the inverter currents, as obtained by applying the above procedure. These parameters have different values depending on the combination of inverter/rectifier voltage and inverter output current being evaluated.

It is evident from (C.7) – (C.9) that the inverter output currents of the ICN converter can be expressed as a summation of time-shifted decaying sinusoidal functions. Utilizing the procedure described in Appendix B, the inverter output currents can be expressed in closed-form. For clarity, these expressions are split into steady-state and startup transient components. The expressions for the inverter output

currents, as a response to the top and bottom inverter switch-node voltages, $i_{\mathrm{x1}}(t)$ and $i_{\mathrm{x2}}(t)$, are given by:

$$i_{\mathrm{x1}}(t) = i_{\mathrm{x1s}}(t) + i_{\mathrm{x1t}}(t), \tag{C.25}$$

$$i_{\mathrm{x2}}(t) = i_{\mathrm{x2s}}(t) + i_{\mathrm{x2t}}(t), \tag{C.26}$$

where the steady-state ($i_{\mathrm{x1s}}(t)$ and $i_{\mathrm{x2s}}(t)$)and startup transient components ($i_{\mathrm{x1t}}(t)$ and $i_{\mathrm{x2t}}(t)$) are given by:

$$i_{\mathrm{x1s}}(t) = \begin{cases} \frac{I_{\mathrm{x11}}\sin\left(\omega_1 t'_{\mathrm{K}} - \frac{\omega_1 T_{\mathrm{s}}}{4}\right)}{2\cos\left(\frac{\omega_1 T_{\mathrm{s}}}{4}\right)} + \frac{I_{\mathrm{x12}}\sin\left(\omega_2 t'_{\mathrm{K}} - \frac{\omega_2 T_{\mathrm{s}}}{4}\right)}{2\cos\left(\frac{\omega_2 T_{\mathrm{s}}}{4}\right)}, 0 \le t'_{\mathrm{K}} < \frac{T_{\mathrm{s}}}{2} \\ \frac{I_{\mathrm{x11}}\sin\left(\frac{3\omega_1 T_{\mathrm{s}}}{4} - \omega_1 t'_{\mathrm{K}}\right)}{2\cos\left(\frac{\omega_1 T_{\mathrm{s}}}{4}\right)} + \frac{I_{\mathrm{x12}}\sin\left(\frac{3\omega_2 T_{\mathrm{s}}}{4} - \omega_2 t'_{\mathrm{K}}\right)}{2\cos\left(\frac{\omega_2 T_{\mathrm{s}}}{4}\right)}, \frac{T_{\mathrm{s}}}{2} \le t'_{\mathrm{K}} < T_{\mathrm{s}} \end{cases}, \tag{C.27}$$

$$i_{\mathrm{x1t}}(t) = \frac{V_{1,\mathrm{ini}}}{V_{IN}} I_{x11} e^{-\alpha_1 t} \sin\omega_1 t + \frac{V_{1,\mathrm{ini}}}{V_{IN}} I_{x12} e^{-\alpha_2 t} \sin\omega_2 t - \frac{I_{x11}}{2\cos\left(\frac{\omega_1 T_{\mathrm{s}}}{4}\right)} e^{-(K-1)\alpha_1 T_{\mathrm{s}}} \sin\left(-\omega_1 t'_{\mathrm{K}} - K\omega_1 T_{\mathrm{s}} + \frac{3\omega_1 T_{\mathrm{s}}}{4}\right) - \frac{I_{x12}}{2\cos\left(\frac{\omega_2 T_{\mathrm{s}}}{4}\right)} e^{-(K-1)\alpha_2 T_{\mathrm{s}}} \sin\left(-\omega_2 t'_{\mathrm{K}} - K\omega_2 T_{\mathrm{s}} + \frac{3\omega_2 T_{\mathrm{s}}}{4}\right), \tag{C.28}$$

$$i_{\mathrm{x2s}}(t) = \begin{cases} \frac{I_{\mathrm{x21}}}{2\cos\left(\frac{\omega_1 T_{\mathrm{s}}}{4}\right)} \sin\left(-\omega_1 t'_{\mathrm{K}} - \frac{\omega_1 T_{\mathrm{s}}}{4} + \omega_1 \frac{\Delta}{\pi} T_{\mathrm{s}}\right) + \frac{I_{\mathrm{x22}}}{2\cos\left(\frac{\omega_2 T_{\mathrm{s}}}{4}\right)} \sin\left(-\omega_2 t'_{\mathrm{K}} - \frac{\omega_2 T_{\mathrm{s}}}{4} + \omega_2 \frac{\Delta}{\pi} T_{\mathrm{s}}\right), \ 0 \le t'_{\mathrm{K}} < \frac{\Delta}{\pi} T_{\mathrm{s}} \\ \frac{I_{\mathrm{x21}}}{2\cos\left(\frac{\omega_1 T_{\mathrm{s}}}{4}\right)} \sin\left(\omega_1 t'_{\mathrm{K}} - \frac{\omega_1 T_{\mathrm{s}}}{4} - \omega_1 \frac{\Delta}{\pi} T_{\mathrm{s}}\right) + \frac{I_{\mathrm{x22}}}{2\cos\left(\frac{\omega_2 T_{\mathrm{s}}}{4}\right)} \sin\left(\omega_2 t'_{\mathrm{K}} - \frac{\omega_2 T_{\mathrm{s}}}{4} - \omega_2 \frac{\Delta}{\pi} T_{\mathrm{s}}\right), \ \frac{\Delta}{\pi} T_{\mathrm{s}} \le t'_{\mathrm{K}} < \frac{\Delta}{\pi} T_{\mathrm{s}} + \frac{T_s}{2} \\ \frac{I_{\mathrm{x21}}}{2\cos\left(\frac{\omega_1 T_{\mathrm{s}}}{4}\right)} \sin\left(-\omega_1 t'_{\mathrm{K}} + \frac{3\omega_1 T_{\mathrm{s}}}{4} + \omega_1 \frac{\Delta}{\pi} T_{\mathrm{s}}\right) + \frac{I_{\mathrm{x22}}}{2\cos\left(\frac{\omega_2 T_{\mathrm{s}}}{4}\right)} \sin\left(-\omega_2 t'_{\mathrm{K}} + \frac{3\omega_2 T_{\mathrm{s}}}{4} + \omega_2 \frac{\Delta}{\pi} T_{\mathrm{s}}\right), \ \frac{\Delta}{\pi} T_{\mathrm{s}} + \frac{T_s}{2} \le t'_{\mathrm{K}} < T_{\mathrm{s}} \end{cases} \tag{C.29}$$

$$i_{\mathrm{x2t}}(t) = \frac{V_{2,\mathrm{ini}}}{V_{IN}} I_{x21} e^{-\alpha_1 t} \sin\omega_1 t + \frac{V_{2,\mathrm{ini}}}{V_{IN}} I_{x22} e^{-\alpha_2 t} \sin\omega_2 t - \frac{I_{x21}}{2\cos\left(\frac{\omega_1 T_{\mathrm{s}}}{4}\right)} e^{-(K-1)\alpha_1 T_{\mathrm{s}}} \sin\left(-\omega_1 t'_{\mathrm{K}} - K\omega_1 T_{\mathrm{s}} + \frac{3\omega_1 T_{\mathrm{s}}}{4}\right) - \frac{I_{x22}}{2\cos\left(\frac{\omega_2 T_{\mathrm{s}}}{4}\right)} e^{-(K-1)\alpha_2 T_{\mathrm{s}}} \sin\left(-\omega_2 t'_{\mathrm{K}} - K\omega_2 T_{\mathrm{s}} + \frac{3\omega_2 T_{\mathrm{s}}}{4}\right) \tag{C.30}$$

$V_{1,\mathrm{ini}}$ and $V_{2,\mathrm{ini}}$ are the initial voltages at the two inverter switch nodes at time $t = 0$ (i.e., at the start of each burst cycle).

For the remaining two terms in (C.5) and (C.6), $i_{\mathrm{x3}}(t)$ (x is 1 or 2), closed-form expressions for steady-state operation are given by (C.31). Here, T_r is the phase lag of the rectifier, which is defined as the time $t'_{\mathrm{K}} = T_r$ when the rectifier current ($(i_1 + i_2)/N$) is zero and hence the rectifier switches commutate. It may be noted that the charging and discharging of the parasitic capacitances of the actual rectifier diodes

during the switching transitions introduce extra delay into T_r. This delay, ΔT_r, can be approximated by the time required to discharge the parasitic capacitances of the rectifier diodes to half of the output voltage and can be obtained from: $\int_{T_r}^{T_r+\Delta T_r} \frac{i_1+i_2}{N} dt = 2C_{diode}V_{OUT} \times \frac{1}{2}$, where N is the transformer turns ratio and C_{diode} is the parasitic capacitance of the rectifier diode. The actual phase lag of the rectifier is given by $T_r + \Delta T_r$.

$$i_{\mathrm{x3s}}(t) =$$

$$\begin{cases} \frac{I_{\mathrm{x31}}}{2\cos\left(\frac{\omega_1 T_\mathrm{s}}{4}\right)}\sin\left(-\omega_1 t'_\mathrm{K} - \frac{\omega_1 T_\mathrm{s}}{4} + \omega_1 T_\mathrm{r}\right) + \frac{I_{\mathrm{x32}}}{2\cos\left(\frac{\omega_2 T_\mathrm{s}}{4}\right)}\sin\left(-\omega_2 t'_\mathrm{K} - \frac{\omega_2 T_\mathrm{s}}{4} + \omega_2 T_\mathrm{r}\right),\ 0 \le t'_\mathrm{K} < T_\mathrm{r} \\ \frac{I_{\mathrm{x31}}}{2\cos\left(\frac{\omega_1 T_\mathrm{s}}{4}\right)}\sin\left(\omega_1 t'_\mathrm{K} - \frac{\omega_1 T_\mathrm{s}}{4} - \omega_1 T_\mathrm{r}\right) + \frac{I_{\mathrm{x32}}}{2\cos\left(\frac{\omega_2 T_\mathrm{s}}{4}\right)}\sin\left(\omega_2 t'_\mathrm{K} - \frac{\omega_2 T_\mathrm{s}}{4} - \omega_2 T_\mathrm{r}\right),\ T_\mathrm{r} \le t'_\mathrm{K} < T_\mathrm{r} + \frac{T_\mathrm{s}}{2} \\ \frac{I_{\mathrm{x31}}}{2\cos\left(\frac{\omega_1 T_\mathrm{s}}{4}\right)}\sin\left(-\omega_1 t'_\mathrm{K} + \frac{3\omega_1 T_\mathrm{s}}{4} + \omega_1 T_\mathrm{r}\right) + \frac{I_{\mathrm{x32}}}{2\cos\left(\frac{\omega_2 T_\mathrm{s}}{4}\right)}\sin\left(-\omega_2 t'_\mathrm{K} + \frac{3\omega_2 T_\mathrm{s}}{4} + \omega_2 T_\mathrm{r}\right),\ T_\mathrm{r} + \frac{T_\mathrm{s}}{2} \le t'_\mathrm{K} < T_\mathrm{s} \end{cases} . \quad \text{(C.31)}$$

For startup transients, closed-form expressions for $i_{13}(t)$ and $i_{23}(t)$ are difficult to obtain as an expression for the commutation time of the diode rectifier at the very beginning of the startup transient is difficult to determine. Thus the actual commutation time is determined numerically by searching across the entire switching period, and utilizing the condition that the rectifier current is near-zero at the commutation instant, taking into account that the actual commutation happens when the parasitic capacitances of the rectifier diodes are fully charged or discharged. It is worth mentioning that for an ICN converter with active rectifier (using transistors), the closed-form expressions for $i_{13}(t)$ and $i_{23}(t)$ can also be obtained, and the resultant expressions are similar to those in (C.28).

Expressions for all the parameters used in (C.27) – (C.31) are listed below:

$$I_{111} = V_{\mathrm{IN}}\beta_1\left[\left(\frac{1}{C_\mathrm{r}N^2} + \frac{1}{C_{\mathrm{X2}}}\right) - \omega_1^2\left(\frac{L_\mathrm{r}}{N^2} + L_{\mathrm{X2}}\right)\right]; \quad \text{(C.32)}$$

$$I_{112} = V_{\mathrm{IN}}\beta_2\left[\left(\frac{1}{C_\mathrm{r}N^2} + \frac{1}{C_{\mathrm{X2}}}\right) - \omega_2^2\left(\frac{L_\mathrm{r}}{N^2} + L_{\mathrm{X2}}\right)\right]; \quad \text{(C.33)}$$

$$I_{121} = -V_{\mathrm{IN}}\beta_1\left(\frac{1}{C_\mathrm{r}N^2} - \omega_1^2\frac{L_\mathrm{r}}{N^2}\right); \quad \text{(C.34)}$$

$$I_{122} = -V_{\mathrm{IN}}\beta_2\left(\frac{1}{C_\mathrm{r}N^2} - \omega_2^2\frac{L_\mathrm{r}}{N^2}\right); \quad \text{(C.35)}$$

$$I_{13b} = -\left(\frac{V_{OUT}}{N}\right)\beta_1\left(\frac{1}{C_{X2}} - \omega_1^2 L_{X2}\right); \tag{C.36}$$

$$I_{13d} = -\left(\frac{V_{OUT}}{N}\right)\beta_2\left(\frac{1}{C_{X2}} - \omega_2^2 L_{X2}\right); \tag{C.37}$$

$$I_{21b} = -V_{IN}\beta_1\left(\frac{1}{C_r N^2} - \omega_1^2\frac{L_r}{N^2}\right); \tag{C.38}$$

$$I_{21d} = -V_{IN}\beta_2\left(\frac{1}{C_r N^2} - \omega_2^2\frac{L_r}{N^2}\right); \tag{C.39}$$

$$I_{22b} = V_{IN}\beta_1\left[\left(\frac{1}{C_r N^2} + \frac{1}{C_{X1}}\right) - \omega_1^2\left(\frac{L_r}{N^2} + L_{X1}\right)\right]; \tag{C.40}$$

$$I_{22d} = V_{IN}\beta_2\left[\left(\frac{1}{C_r N^2} + \frac{1}{C_{X1}}\right) - \omega_2^2\left(\frac{L_r}{N^2} + L_{X1}\right)\right]; \tag{C.41}$$

$$I_{23b} = -\left(\frac{V_{OUT}}{N}\right)\beta_1\left(\frac{1}{C_{X1}} - \omega_1^2 L_{X1}\right); \tag{C.42}$$

$$I_{23d} = -\left(\frac{V_{OUT}}{N}\right)\beta_2\left(\frac{1}{C_{X1}} - \omega_2^2 L_{X1}\right); \tag{C.43}$$

$$\beta_1 = \frac{1}{\omega_1(\omega_2^2 - \omega_1^2)\left(L_{X1}L_{X2} + L_{X1}\frac{L_r}{N^2} + L_{X2}\frac{L_r}{N^2}\right)}; \tag{C.44}$$

$$\beta_2 = \frac{1}{\omega_2(\omega_1^2 - \omega_2^2)\left(L_{X1}L_{X2} + L_{X1}\frac{L_r}{N^2} + L_{X2}\frac{L_r}{N^2}\right)}. \tag{C.45}$$

Appendix D

Loss Model

This appendix provides the loss model that is used to estimate the efficiency and loss breakdown of the ICN converter. This loss model includes transistor losses, diode losses, inductor losses, transformer losses, capacitor losses, and the PCB trace losses. The equations used to estimate the losses are summarized below.

Inverter Losses

The turn-on losses of the transistors in the inverters are negligible as they achieve ZVS at all operating points. Therefore, only conduction losses, turn-off losses and gate charge losses are considered for these transistors. The conduction losses in each transistor are calculated using:

$$\mathrm{P_{trans,cond}} = \mathrm{I_{rms}^2 R_{ds(on)}}, \tag{D.1}$$

where, I_{rms} is the RMS current through the transistor, $R_{ds(on)}$ is the on-state resistance of the transistor. The turn-off losses of each transistor are calculated assuming the current through its channel decreases linearly to zero upon transistor turns off. The remaining current (which increases linearly) flows into its output capacitance, leading to a quadratic rise in the transistor's drain-source voltage. The overlap between the channel current and the drain-source voltage results in losses, and is given by:

$$\mathrm{P_{trans,off}} = \frac{\mathrm{I_{off}^2 t_{off}^2 f_{sw}}}{48\mathrm{C_{oss}}}. \tag{D.2}$$

Here I_{off} is the current through the transistor at the turn-off instant, t_{off} is the fall time of the current, f_{sw} is the switching frequency of the converter, and C_{oss} is the output capacitance of the transistor. The gate charge losses of each transistor are calculated using:

$$\mathrm{P_{trans,gate}} = \mathrm{V_{gs} Q_g f_{sw}}, \tag{D.3}$$

where V_{gs} is the gate-to-source voltage of the transistor, and Q_g is the total gate charge of the transistor.

Rectifier Losses

The rectifier diode in on-state can be modeled as a voltage source in series with an on-state resistor. Therefore, diode losses are calculated using:

$$P_{diode} = I_{avg}V_t + I_{rms}^2 R_t, \tag{D.4}$$

where I_{avg} is the average current through the diode, V_t is the diode's voltage drop, I_{rms} is the RMS current through the diode, and R_t is its on-state resistance.

Magnetic Losses

Losses in the inductors and the transformer include winding losses and core losses. Winding losses are calculated using:

$$P_{winding} = \sum_{i=1}^{11} I_{rms,i}^2 R_{dc} F_{r,i}, \tag{D.5}$$

where $I_{rms,i}$ is the RMS value of the *i*th harmonic of the current through the winding, R_{dc} is the dc resistance resistance of the winding, and $F_{r,i}$ is a factor that relates the ac resistance to the dc resistance, and is determined using equation (2) of reference [22]. The first eleven harmonics of the winding current are used to calculate the winding losses. The core losses are calculated using the improved generalized Steinmetz equation (iGSE) [23]:

$$P_{core} = V_c \frac{1}{T} \int_0^T k_i \left|\frac{dB}{dt}\right|^\alpha (\Delta B)^{\beta-\alpha} dt, \tag{D.6}$$

$$k_i = \frac{k}{(2\pi)^{\alpha-1} \int_0^{2\pi} |\cos\theta|^\alpha 2^{\beta-\alpha} d\theta}. \tag{D.7}$$

Here V_c is the core volume, B is the flux density, ΔB is the peak-to-peak flux density, T is the cycle period of the flux density (the same as switching period), and k, α and β are material parameters used in the basic Steinmetz equation $P_v = k f^\alpha B_{pk}^\beta$, where P_v is the core loss per unit volume, and B_{pk} is the peak value of a sinusoidal excitation, and f is the frequency of the sinusoidal excitation.

Capacitor Losses

The losses in the capacitors are calculated using:

$$P_{cap} = I_{rms}^2 R_{esr}, \tag{D.8}$$

where I_{rms} is the RMS current through the capacitor, and R_{esr} is the equivalent series resistance of the capacitor.

PCB Trace Losses

The PCB trace losses are calculated using:

$$P_{PCB} = I_{rms}^2 R_{dc} \frac{h}{\delta}, \tag{D.9}$$

where I_{rms} is the RMS current through the PCB trace, R_{dc} is the dc resistance of the PCB trace, h is the thickness of the trace, and δ is the skin depth.

Appendix E

Sensitivity Analysis

To investigate the robustness of the ICN converter to variations in component values, and the possibility of compensating for these variations through slight changes in the available control handles, the sensitivity of the ICN converter's key performance metrics to variations in component values, switching frequency, and the phase shift between the inverters is studied. The performance metrics of interest are the converter's soft switching ability, maximum output power, and conversion efficiency. The change in these performance metrics as the value of inductor L_{X1} varies across a $\pm 10\%$ range is shown in Fig. E.1. As can be seen from Fig. E.1 (a), the sensitivity of the inverter turnoff current to variations in in value of L_{X1} depends on the converter's operating point. The inverter turnoff current for both inverters is most sensitive when the ICN converter is at its maximum boost operating point (25 V input voltage and 400 V output voltage). At all operating points the inverter turnoff current tends towards a positive value when the value of L_{X1} decreases, and with a large decrease in L_{X1} the inverter switches will lose ZVS. At the worst case operating point (25 V input voltage and 400 V output voltage) the loss in ZVS occurs when L_{X1} is reduced by around 2.5% from its nominal value. When the value of L_{X1} increases, the inverter turnoff current becomes more negative, which leads to the eventual loss of near ZCS. Interestingly the maximum output power and the efficiency of the ICN converter do not change too much across a $\pm 10\%$ variation in the value of L_{X1}. The change in performance of the ICN converter with variations in the values of the other components (C_{X1}, L_{X2}, C_{X2}, L_r, C_r) is also investigated in the same way. Figure E.2 shows the change in the top inverter turnoff current across $\pm 10\%$ variations in the values of these components. The top inverter turnoff current tends to become less negative when C_{X1}, L_{X2}, or C_{X2} decrease or when L_r or C_r increase, and the top inverter turnoff current becomes more negative when the component values change in the opposite direction. The change in the bottom inverter turnoff current is very similar to that in the top inverter. Also, as with variations in L_{X1}, the maximum output power and efficiency of the ICN converter do not change much with slight changes in these component values.

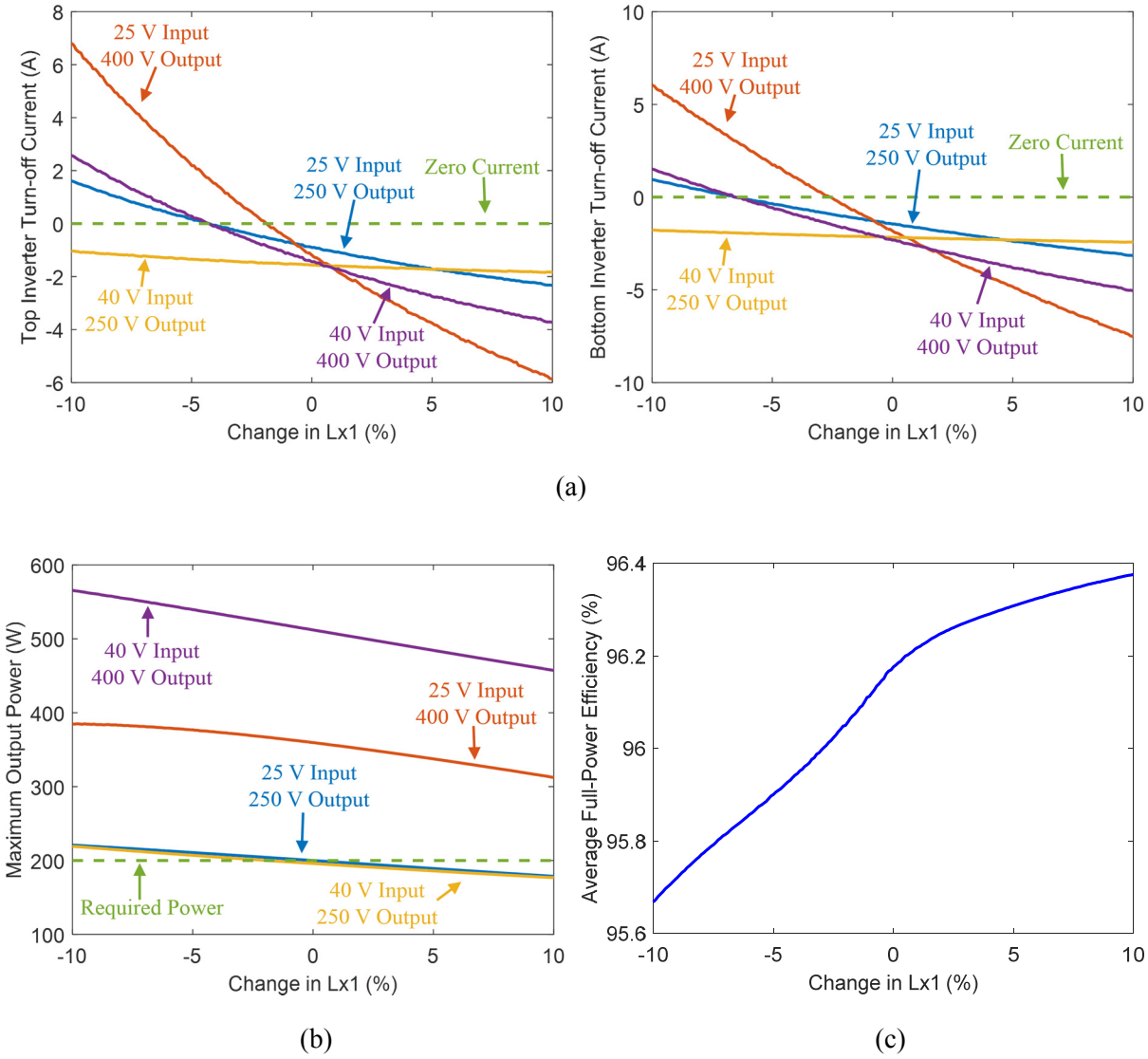

Figure E.1: Variations in (a) inverter turn-off current, (b) maximum output power, and (c) average full-power efficiency of the medium-Q (Q=1) ICN converter as a function of variations in L_{X1}.

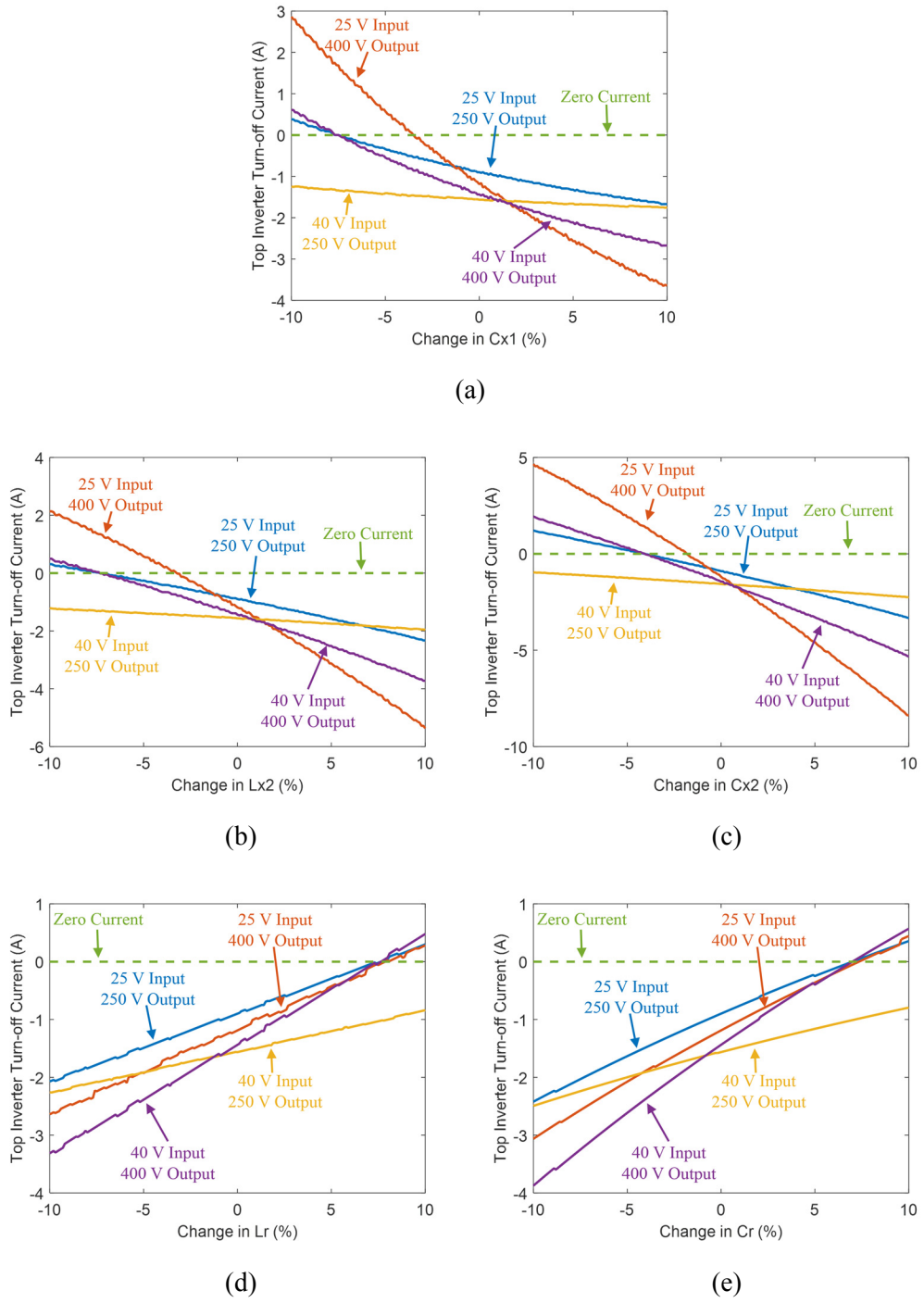

Figure E.2: Change in top inverter turnoff current of the medium-Q ICN converter across ±10% variations in the value of a) C_{X1}, (b) L_{X2}, (c) C_{X2}, (d) L_r, and (e) C_r.

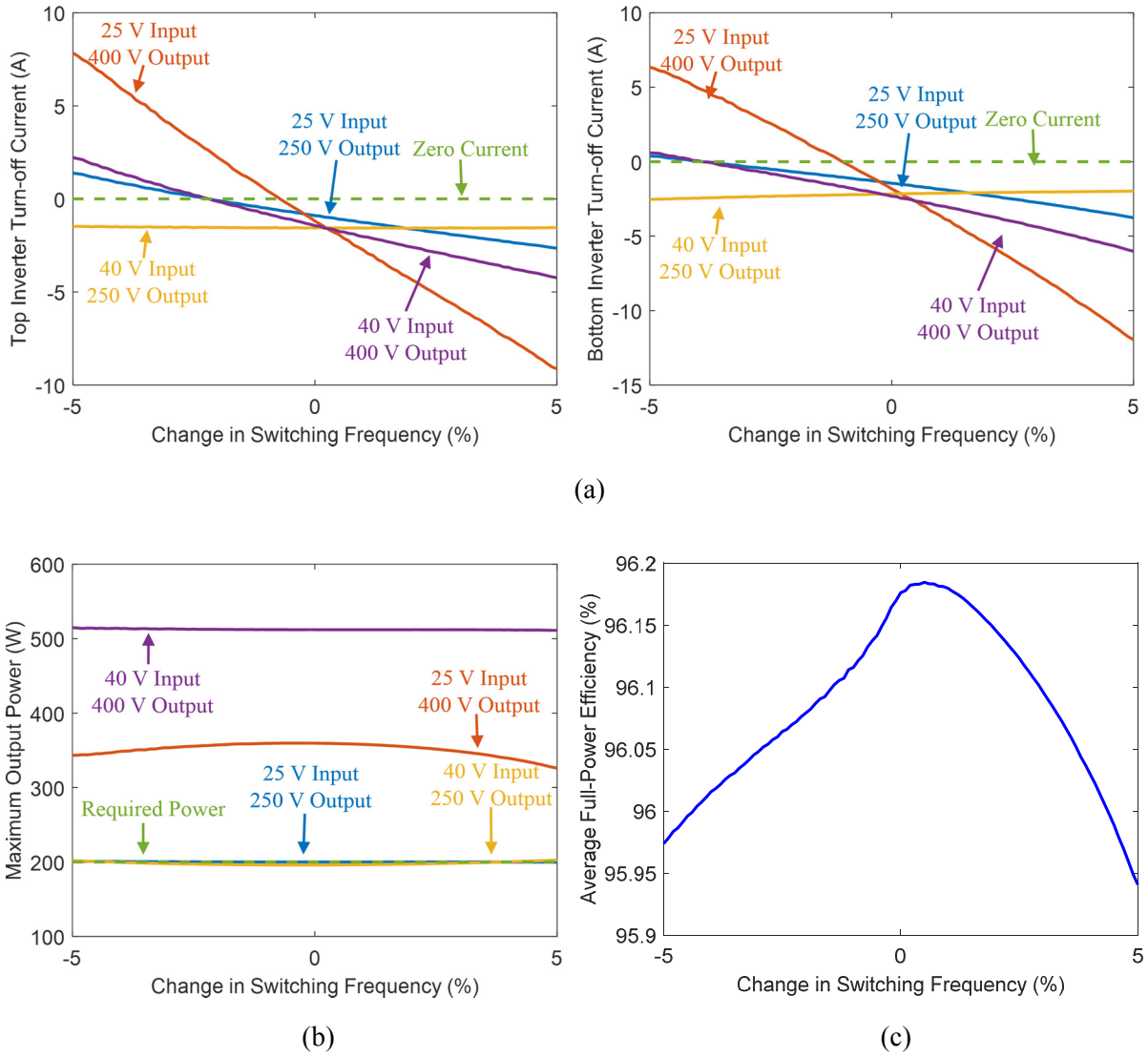

Figure E.3: Variations in (a) inverter turn-off current, (b) maximum output power, and (c) average full-power efficiency of the medium-Q (Q=1) ICN converter as a function of variations in switching frequency.

As shown above, variations in component values do change the soft switching ability of the ICN converter; therefore it is valuable to see if the available control handles (switching frequency and phase shift between inverters) can be adjusted slightly to compensate for the change in turn-off current. Figure E.3 shows the change in performance of the ICN converter across $\pm 5\%$ variations in switching frequency. As can be seen from Fig. E.3 (a), the inverter turnoff current is quite sensitive to the switching frequency. The inverter turnoff current will become less negative (and eventually positive) when the switching frequency decreases, and it will become more negative when switching frequency increases. Moreover, the change in maximum output power and efficiency is quite small with such variations in the switching frequency, as shown in Fig. E.3 (b) and (c). Hence, switching frequency is a good candidate to compensate for changes in inverter turn-off currents and recover the soft switching ability of the ICN converter in case it is lost due to variations in component values. Another potential candidate is the phase shift between the inverters. Figure E.4 shows the change in performance of the ICN converter across $\pm 20\%$ variations in phase shift between the inverters. As can be seen from Fig. E.4 (a), the top and bottom inverter turnoff currents change in the opposite directions with variations in phase shift. Again, the change in maximum output power and efficiency is quite small with variations in phase shift, as can be seen in Fig. E.4 (b) and (c). Hence, phase shift can be used to compensate for any differential-mode changes in the top and bottom inverter turnoff currents.

To demonstrate the above-mentioned compensation techniques for variations in inverter turn-off current due to variations in component values, two examples are considered. Figure E.5 shows the inverter output voltage and current for the medium-Q ICN converter with L_{X1} decreased by 10% from its nominal value, while Fig. E.6 shows the same waveforms with L_{X1} increased by 10% from its nominal value. In Fig. E.5 (a), the switching frequency of the converter is 505 kHz, which results in positive turnoff current for both inverters, and both inverters lose ZVS. To recover ZVS capability, the switching frequency is increased by 5% (to 530 kHz) in Fig. E.5 (b). The resultant inverter turn-off currents become slightly negative and both inverters achieve ZVS and near ZCS. In Fig. E.6 (a) (with L_{X1} increased), the converter switches at 505 kHz, and the inverter turn-off currents are very negative so near ZCS is not achieved. In Fig. E.6 (b), the

switching frequency is decreased by 3% to 490 kHz to make the inverter turn-off current only slightly negative to achieve ZVS and near ZCS. Hence, slightly adjusting the switching frequency is an effective way to compensate for variations in the component values of the ICN converter. If L_{X1} had decreased and L_{X2} had increased, requiring a differential adjustment in the inverter currents, a slight adjustment in phase could additionally be employed to compensate for these changes.

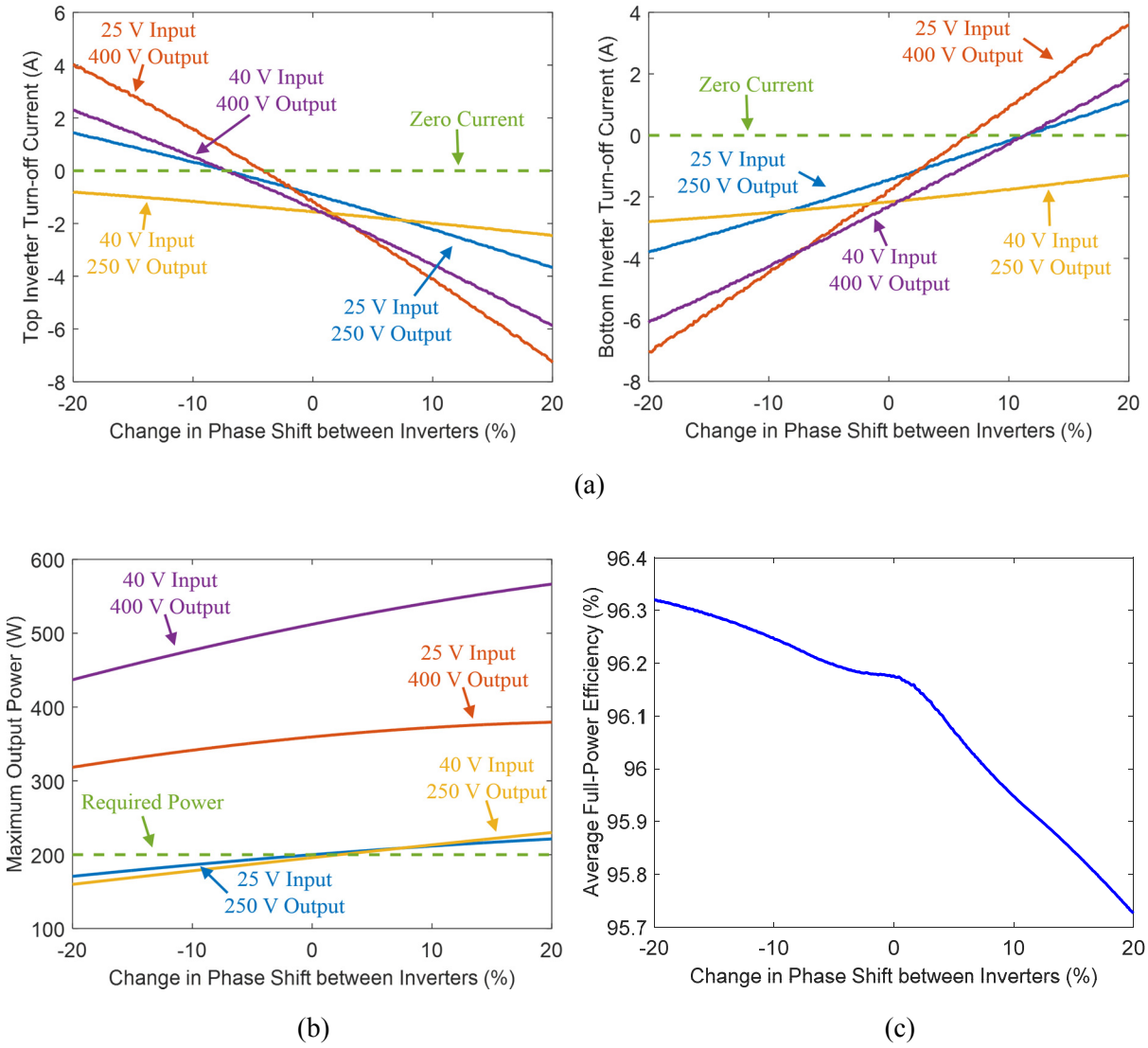

Figure E.4: Variations in (a) inverter turn-off current, (b) maximum output power, and (c) average full-power efficiency of the medium-Q (Q=1) ICN converter as a function of variations in phase shift.

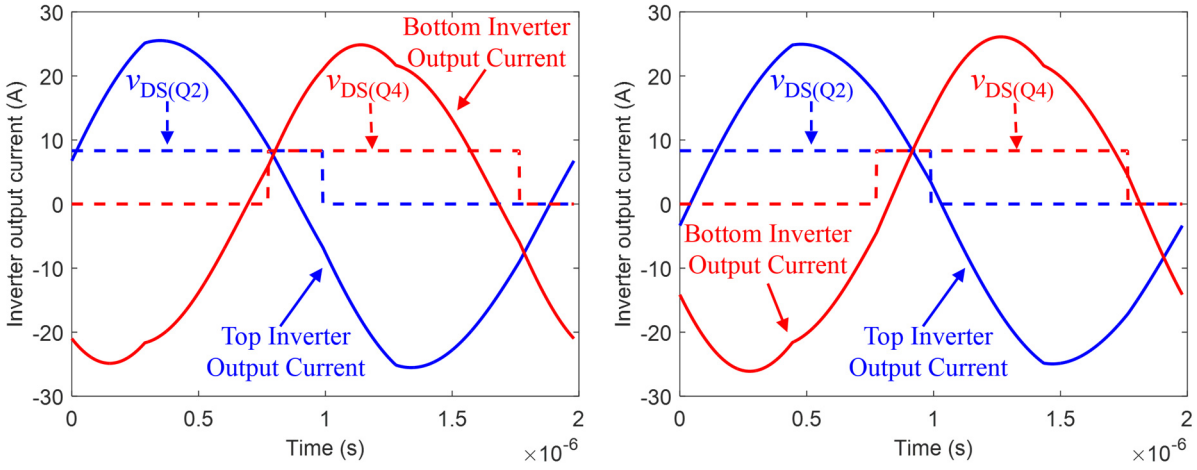

Figure E.5: Inverter output voltage and current for the medium-Q (Q=1) ICN converter with L_{X1} decreased by 10% from its original value. The switching frequencies used in (a) and (b) are 505 kHz and 530 kHz, respectively. In both cases, the converter is operated with 25 V input voltage and 400 V output voltage.

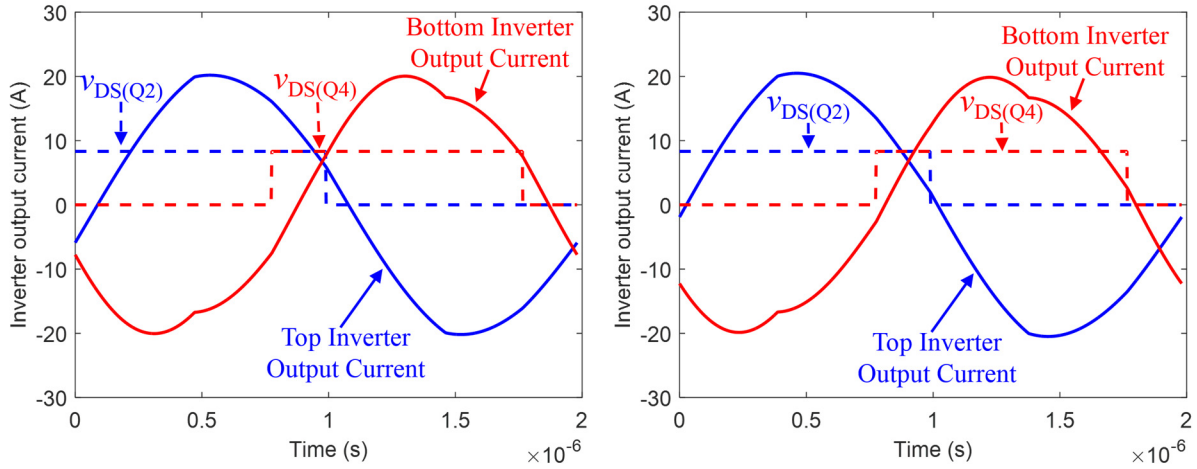

Figure E.6: Inverter output voltage and current for the medium-Q (Q=1) ICN converter with L_{X1} increased by 10% from its original value. The switching frequencies used in (a) and (b) are 505 kHz and 490 kHz, respectively. In both cases, the converter is operated with 25 V input voltage and 400 V output voltage.

The above discussion shows that with known component values, for a given combination of input and output voltages, there is an optimum choice of switching frequency and phase shift that results in a turnoff current which maximizes the converter efficiency. With known component values, one way to achieve this optimal turnoff current automatically would be to use a lookup table that stores the optimum values of switching frequency and phase shift as a function of input and output voltages. However, with component tolerances in a practical converter, the above method needs to be augmented with a self-learning algorithm that determines the optimum switching frequency and phase shift as a function of input and output voltages during converter operation to maximize efficiency. This can be achieved through an online efficiency optimization technique similar to the one presented in [24], [25].